A comprehensive analysis of dynamic indentation and impact behavior in viscoelastic solids

POLITECNICO DI BARI

DEPARTMENT OF MECHANICS, MATHEMATICS AND MANAGEMENT
Mechanical and Management Engineering Ph.D. Program
SSD: ING-IND/13 - Applied Mechanics

Dissertation in

A Comprehensive Analysis of Dynamic Indentation and Impact Behavior in Viscoelastic Solids

Supervisor
Prof. Carmine PUTIGNANO
Prof. Giuseppe CARBONE

Candidate
Etibar MIKAYILOV

Coordinator of the Ph.D. Program: Prof. Giuseppe CASALINO
Course XXXVIII, 01/11/2022 - 30/04/2026

Summary

The main research topic of this thesis is the in-depth study of the time-dependent mechanical behaviour of viscoelastic materials, particularly their responses under contact loading conditions. Viscoelastic solids, such as polymers, elastomers and biological tissues, exhibit complex mechanical responses characterised by a combination of elastic energy storage and viscous dissipation. These properties give rise to phenomena such as stress relaxation, creep, and hysteresis, which are fundamental to a wide range of engineering and biomedical applications. However, the study of these properties requires complex, traditional experimental analyses such as DMA, which is both time-consuming and leads to destructive damage through material exposure to high temperatures. The main objective of this thesis is to address the challenges involved in accurately and rapidly characterising and modelling the properties of such viscoelastic materials, particularly under dynamic loading conditions such as indentation and impact, using methods that differ from traditional approaches.

The research develops a unified and comprehensive framework that combines experimental techniques, numerical simulations, and theoretical modelling to analyse viscoelastic contact mechanics. The research covers two important complementary aspects: the first is the study of the behaviour of viscoelastic materials under harmonic and quasi-static compression, and the other is the analysis of their dynamic response under normal impact. The application of this dual approach allows for a unified understanding of both steady and transient behaviours. The methodology combines the use of various advanced experimental setups, including the Biomomentum-Mach1 and Dynamic Mechanical Analysis used in experimental practices, as well as custom-built in-laboratory indentation and impact systems, with numerical modelling based on the Boundary Element Method. This integration allows for the accurate representation and study of both global mechanical responses, such as force and displacement, and local contact phenomena, including the evolution of the contact area, which has not been considered in previous studies.

At the theoretical level, the thesis is justified within a linear viscoelasticity framework. Thus, the material's stress response depends on the entire history of the deformation applied to it. This behaviour is mathematically explained by convolution integrals derived from the Boltzmann principle of superposition. The material's

fundamental properties—the relaxation modulus and creep compliance—are also characterised by the complex modulus in the frequency domain. The decomposition of the complex modulus into storage and loss components provides insight into the balance between elastic energy accumulation and viscous energy dissipation. The study also encompasses thermodynamic principles, ensuring that constitutive models satisfy conditions such as causality and non-negative energy dissipation, thereby preserving physical consistency.

The initial main part of the thesis was based on the study of the indentation behaviour of a viscoelastic material using a specially designed sinusoidal indenter. Both stress relaxation and harmonic indentation experimental tests are carried out on nitrile butadiene rubber, which allows for the measurement of the force response and energy dissipation in the material. These experimental results are then systematically compared with numerical simulations and analytical approximations, conducted under the same conditions, based on the Boundary Element Method. The results obtained demonstrate a strong agreement between the three approaches—analytical, numerical, and experimental—and confirm the validity of the proposed framework. The study shows that the indentation behaviour of viscoelastic materials varies with the loading frequency and amplitude, and provides a quantitative estimation of the energy dissipated through a new analytical formulation. This indentation method enables the efficient and non-destructive characterisation of viscoelastic materials. The second part of the thesis is based on the study of dynamic impact events, analysing the normal collision of viscoelastic spheres made from materials such as PTFE, PEEK, Nylon and Acrylic with a rigid sapphire substrate. A experimental setup has been developed to determine the motion of the spheres and the evolution of the contact area, incorporating laser displacement measurements and high-speed imaging. These analyses allow for a detailed investigation of transient behaviours, including deformation, rebound, and energy dissipation. A mathematical model based on linear viscoelastic contact mechanics, which accounts for the time-dependent material response, has been formulated to simulate the impact process. The comparison between the experimental results and the numerical predictions shows excellent agreement under various impact conditions, including variations in drop height and temperature. All these results confirm the validity and predictive capability of the proposed modelling approach.

The thesis presents a unified, predictive framework for viscoelastic contact analysis that combines numerical and analytical methods. Through this methodology, the viscoelastic behavior of materials can be characterized by simple, fast, and non-destructive contact tests. These methodologies have a wide range of applications in both engineering and various fields of science.

Abstract

Viscoelastic materials exhibit complex, time-dependent mechanical behaviour, which is one of their fundamental properties and is widely used in engineering and biomedical applications. The accurate characterisation and predictive modelling of their complex behaviour, particularly under various loading conditions such as indentation and impact, remains a key challenge. In this dissertation, an experimental, numerical and theoretical combined framework is developed to investigate the contact mechanics of viscoelastic solids. Two important complementary problems are addressed: dynamic indentation and normal impact.

First, the viscoelastic response of nitrile butadiene rubber (NBR) under sinusoidal deformation is investigated. Such indentation plays a key role as an alternative standard technique for the reliable, rapid, and non-destructive characterisation of materials in practical applications, particularly in sensitive fields such as biotechnology, as well as in viscoelastic dampers. In this study, experimental measurements obtained with specially designed sinusoidal indenters are compared with numerical simulations based on the Boundary Element Method (BEM) and a simplified theoretical formulation. The experimental, numerical, and theoretical predictions closely match one another, with only minor differences in the peak force and the relaxation phases. These findings validate the proposed multi-disciplinary methodology and highlight its effectiveness in the characterisation of viscoelastic materials and the estimation of dissipated energy.

In the next stage, the dynamic behaviour of spheres such as PTFE, acrylic, PEEK and Nylon is investigated on a hard sapphire surface under normal impact. A custom-designed experimental setup combines controlled drop tests, a laser distance sensor, and high-speed imaging to record both the sphere's motion and the evolution of the contact area at room temperature and at elevated temperatures. A numerical model based on linear viscoelastic contact mechanics, which incorporates the normal dynamics of the system, has been developed. Comparisons between the simulations and experiments show that under various impact conditions, the reduction of the gap during the initial impact events closely follows the measured contact-radius profiles. Despite its simplified formulation, the model successfully captures the main features of contact dynamics.

In conclusion, the results of this thesis suggest that the integration of experimental techniques with advanced numerical modelling provides a fast, robust and reliable framework for the analysis of viscoelastic contact problems. The proposed methodologies contribute to a deeper understanding of the quasi-static and dynamic responses of viscoelastic materials. At the same time, they provide practical tools for their reliable characterisation and design in engineering applications.

Contents

List of Figures VIII

Introduction 1

1 Foundations of Linear Viscoelasticity 6
- 1.1 Constitutive Relations Under Steady-State Conditions 11
- 1.2 Thermoviscoelastic Behavior of Materials 14
- 1.3 Constitutive Rheological Models for Materials 20

2 Dynamic Response of Viscoelastic Solids 27
- 2.1 Materials and Experimental Methods 28
- 2.2 Theoretical and Numerical Framework 31
- 2.3 Results and discussion 38
  - 2.3.1 Dynamic Mechanical Analysis of NBR 38
  - 2.3.2 Stress Relaxation and Harmonic Indentation Experiments . 41
  - 2.3.3 Energy Dissipation and Analytical Approximation 46

3 Impact Response of Viscoelastic Solids 52
- 3.1 Materials and Experimental Methods 54
- 3.2 Theoretical and Numerical Framework 59
- 3.3 Results and discussion 63
  - 3.3.1 Dynamic Mechanical Analysis of the Spheres 63
  - 3.3.2 Experimental Validation via Laser and High-Speed Imaging 64
  - 3.3.3 Effect of Drop Height on Impact Response 68
  - 3.3.4 Static Loading Tests 77

Conclusions 80

A Preliminary Theoretical Model for Acrylic Ball Drop Experiments 85
  - A1 Theoretical Framework for Collision Dynamics and Impact Trajectory Analysis 85
  - A2 Comparison with experimental results 87

B Plate Vibration During Impact Tests 90
B1 Experimental Setup and Measurement 90
B2 Measured Vibration Response 92
B3 Influence on Experimental–Numerical Discrepancies 92

C Experimental Comparison of Displacement and Contact Radius 94
C1 Overview of Experimental Results 94

D Camera and Image Calibration Procedures Used in the DIC Validation Tests 96
D1 DIC Calibration — PTFE Ball Drop Test 96
D2 Contact-Area Calibration: Camera Beneath the Sapphire Disc 98

Bibliography 100

Publications 111

Acknowledgments 112

List of Figures

1.1 Sinusoidal stress–strain responses under harmonic loading: (a) Ideal elastic — stress and strain are in phase ($\delta = 0°$); (b) Viscoelastic — stress is delayed ($0° < \delta < 90°$), indicating both elastic storage and viscous dissipation; (c) Ideal viscous — stress is proportional to the rate of strain ($\delta = 90°$). 8

1.2 Frequency dependence of the complex modulus for a material with a single relaxation time τ. The storage modulus $\mathcal{G}'(\omega) = \operatorname{Re}\mathcal{G}^*(\omega)$ (black) quantifies stored elastic energy, while the loss modulus $\mathcal{G}''(\omega) = \operatorname{Im}\mathcal{G}^*(\omega)$ (blue) quantifies viscous dissipation. $\mathcal{G}'(\omega)$ rises from the relaxed modulus $\mathcal{G}_0$ at low frequencies to the unrelaxed modulus $\mathcal{G}_\infty$ at high frequencies, while $\mathcal{G}''(\omega)$ peaks at $\omega\tau \approx 1$, where the loading time scale matches the material's relaxation time. 13

1.3 The viscoelastic behavior of a polymer is characterized by the storage modulus $\mathcal{G}'(\omega) = \operatorname{Re}(\mathcal{G}^*(\omega))$ and the loss tangent $\tan\delta(\omega) = \mathcal{G}''(\omega)/\mathcal{G}'(\omega)$, both presented as functions of logarithmic frequency or temperature. The curves illustrate the glassy, transition, and rubbery regions, along with the relaxation processes α, β, and γ, including the glass transition (θ_g). Vertical dashed lines indicate θ_α, θ_β, and θ_γ, while the extension at low frequency shows the viscous flow regime. 18

1.4 Schematic representation of $\mathcal{G}'(\omega)$ (black solid line) and $\tan\delta$ (blue dashed line) as functions of frequency for different polymer classes: (a) amorphous thermoplastics (linear or branched), (b) semi-crystalline thermoplastics (linear or branched), (c) elastomers (sparsely cross-linked), and (d) thermosets (densely cross-linked). 18

1.5 The glass transition is shown from volumetric and molecular perspectives. On the left, the specific volume–temperature curve changes slope at θ_g, separating the low-mobility glassy state from the high-mobility rubbery state; the dashed line extrapolates the glassy region, while the open line marks the free-volume increase above θ_g. On the right, the molecular picture shows densely packed chains below θ_g and enhanced mobility above it, driven by increased free volume. 19

1.6 Schematic representation of the Maxwell viscoelastic model. 20

1.7 Relaxation modulus and creep compliance of the Maxwell model, together with the frequency-domain representation of its complex modulus. (a) Relaxation modulus, $\mathcal{G}(t) = \mathcal{E}\ \exp(-t/\tau)$, as a function of time. (b) Creep compliance, $\mathcal{J}(t) = 1/\mathcal{E} + t/\mu$, as a function of time. (c) Real part of the complex modulus, $\mathrm{Re}(\mathcal{G}^*(\omega)) = \mathcal{G}'(\omega)$ (black line, left axis), and imaginary part, $\mathrm{Im}(\mathcal{G}^*(\omega)) = \mathcal{G}''(\omega)$ (blue line, right axis), plotted as functions of angular frequency ω. The dashed vertical line denotes the characteristic frequency $\omega = 1/\tau$. . 23

1.8 Schematic representation of the standard linear solid model. 24

1.9 Standard linear solid (Zener) model. (a) Relaxation function $\mathcal{G}(t)$ as a function of time, showing a decay from the instantaneous modulus to a finite equilibrium value. (b) Creep function $\mathcal{J}(t)$ as a function of time, illustrating a bounded increase in compliance. (c) Real part of the complex modulus, $\mathrm{Re}(\mathcal{G}^*(\omega))$ (black line, left axis), and imaginary part, $\mathrm{Im}(\mathcal{G}^*(\omega))$ (blue line, right axis), plotted as functions of angular frequency ω on a logarithmic scale. The curves highlight the transition between low- and high-frequency elastic regimes and the intermediate viscoelastic response. 25

1.10 Schematic representation of the generalized Maxwell model. 25

2.1 Schematic overview of the Anton Paar MCR 702e MultiDrive dynamic mechanical analyzer (DMA), highlighting its dual-drive system for rotational shear and linear DMA testing modes (tension, compression, bending). 29

2.2 Experimental setup for static and dynamic testing of NBR samples. (a) Biomomentum-MACH1 machine setup, (b) schematic illustration of the indentation-sample interface, and (c) illustration of the indentation design placed on the NBR sample under real conditions. 30

2.3 Illustration of the viscoelastic modulus master curves obtained from DMA analysis for Nitrile Rubber (NBR). The storage modulus is shown as the blue line and the loss modulus is shown as the red line, and is denoted as Re $\mathcal{E}(\omega)$ and Im $\mathcal{E}(\omega)$, respectively. (a) The viscoelastic modulus shift factors are plotted as a function of temperature a_T (b); the compliances C_i are characterized as a function of the relaxation times τ_i for NBR. (c). The reference temperature of the analyses is taken to be $T_0 = 20°\mathrm{C}$. 39

2.4 Stress relaxation curves obtained for different values of the dimensionless penetration $\tilde{\Delta} = \Delta/R$, where the indenter radius is $R = 2$ mm. The three panels correspond to $\tilde{\Delta} = 0.05$ (left), $\tilde{\Delta} = 0.1$ (center), and $\tilde{\Delta} = 0.15$ (right). On the left vertical axis, the experimentally measured normal force (red dots) is compared with the numerical prediction obtained from the model (solid blue line). On the right vertical axis, the imposed indentation displacement is reported (solid black line). 42

2.5 The upper left panel displays the dimensionless penetration $\tilde{\Delta} = \Delta/R$ (black line) as a function of dimensionless time $\tilde{t}$ at an indenting frequency $\tilde{f} = 0.78 \times 10^{-10}$. In the lower panel, (a) compares the dimensionless normal force $\tilde{F}_n = F/(E_0 \lambda d)$, where d is the out-of-plane thickness, between experimental data (red dots) and numerical results (blue line). Panel (b) shows $\tilde{F}_n$ versus $\tilde{\Delta}$ for various indenting frequencies $\tilde{f} = f\tau_0$. 44

2.6 (a) Contour plot of the dimensionless dissipated work $\tilde{W}$, calculated using Eq. (2.31), for vertical harmonic oscillation of the punch as a function of dimensionless frequency $\tilde{f}$ and amplitude $\tilde{\alpha}$ at constant mean indentation $\tilde{\Delta}_0 = 0.05$. The red curve shows the analytical detachment boundary from Eq. (2.34), which separates the detachment region (white) from continuous contact. (b) Dimensionless dissipated work versus frequency for the critical amplitude $\tilde{\alpha}^* = 0.005$, illustrating the influence of the loss modulus Im $\mathcal{E}(\omega)$ as described by Eq. (2.31). 47

2.7 The pressure distribution at different time steps is characterized by the black line and the corresponding displacement distribution, the red line. The dotted red line shows the change in the position of the rigid indenter. In the simulation, the average displacement value is $\tilde{\Delta}_0 = 0.25$, the oscillation frequency is $\tilde{\alpha} = 3.12 \times 10^{-10}$ and the amplitude is $\tilde{\alpha} = 0.15$. 48

2.8 The graph compares the dissipated work $\tilde{W}$ during the vertical oscillation of the punch at different frequencies. Dashed lines with red dots indicate experimental measurements at ten frequencies, while the solid green line shows theoretical results. The dashed line with blue dots represents Boundary Element Method (BEM) analyses based on Eq. 2.31. 50

3.1 (a) General view of the experimental setup for the ball drop test, equipped with electromagnetic release, micrometer height adjustment, 3D printed holder, laser sensor, and high-speed camera; (b) close-up view of the holder-ball-sapphire contact area; (c) loading configuration of weights attached to the holder, intended for the static test; and (d) 3/4-inch Nylon, PTFE, PEEK, and Acrylic spheres manufactured by PCS Instruments and used in the tests. 55

3.2 Experimental setup and temperature measurement for studying the contact analysis of acrylic sphere at high temperatures (a) Schematic representation of the experimental configuration, where an acrylic sphere mounted on a vertical holder impacts the substrate, while localized heating is applied using a heat gun. The contact event is recorded from below using a Phantom Mini UX100 high-speed camera. (b) Thermal image of the contact area obtained using an infrared thermometer, showing the controlled temperature of approximately 39 °C. 57

3.3 (a) The evolution of the reduced gap g_r as a function of time t_c for a given initial drop height h_0, where $t_c = 0$ corresponds to the first contact. (b) Qualitative illustration of the impact process. 59

3.4 Viscoelastic modulus master curves obtained from DMA analysis for a PEEK sphere: the left panel shows the experimental data for the storage and loss moduli (blue circles Re $\mathcal{G}$, red circles Im $\mathcal{G}$ and the numerical fits (solid blue and black lines), respectively; the right panel presents the temperature-dependent slip factors a_T, with the reference temperature $T_0 = 129.93$°C. 64

3.5 Viscoelastic modulus master curves obtained from DMA analysis for a Nylon sphere: the left panel shows the experimental data for the storage and loss moduli (blue circles Re $\mathcal{G}$, red circles Im $\mathcal{G}$ and the numerical fits (solid blue and black lines), respectively; the right panel presents the temperature-dependent slip factors a_T, with the reference temperature $T_0 = 20.16$°C. 64

3.6 Viscoelastic modulus master curves obtained from DMA analysis for a Acrylic sphere: the left panel shows the experimental data for the storage and loss moduli (blue circles Re $\mathcal{G}$, red circles Im $\mathcal{G}$ and the numerical fits (solid blue and black lines), respectively; the right panel presents the temperature-dependent slip factors a_T, with the reference temperature $T_0 = 20.042$°C. 65

3.7 Viscoelastic modulus master curves obtained from DMA analysis for a PTFE sphere: the left panel shows the experimental data for the storage and loss moduli (blue circles Re $\mathcal{G}$, red circles Im $\mathcal{G}$ and the numerical fits (solid blue and black lines), respectively; the right panel presents the temperature-dependent slip factors a_T, with the reference temperature $T_0 = 20.031°C$. 65

3.8 Deformation evolution of the PTFE ball impact on a sapphire disc. (a) DICe analysis of the PTFE ball holder showing the reference line (blue) selected on the subset of automatically detected points (yellow dots). (b) Time-lapse deformation of the reference line at selected times (0, 0.074, 0.085, 0.106, 0.126,3, 0.138, 0.149,6, 0.155,6, 0.161,8 s, and final time - 0.300 s). The line drops from a 7 mm height and progressively deforms upon impact, with subsequent rebounds visible. All coordinates are in mm (calibration: 1 pixel = 77.7 µm). 66

3.9 Time evolution of the ball drop response for a drop height of $h = 7$ mm, obtained from the high-speed Phantom Mini UX100 camera (blue markers) obtained from the DIC and from laser measurements (red markers). Panel (a) presents the experimental displacement histories of both tests, while panel (b) shows the corresponding velocities calculated from these data. 67

3.10 The impact response of an Acrylic sphere dropped from heights $h_0 =$ 1.5 mm, 5 mm, 7 mm, and 10 mm. shows the variation of the vertical displacement h as a function of time t. The experimental data with uncertainty is represented by the blue region, while the red line shows the numerical prediction of the gap evolution. 68

3.11 The impact response of an Nylon sphere dropped from heights $h_0 =$ 1.5 mm, 5 mm, 7 mm, and 10 mm. shows the variation of the vertical displacement h as a function of time t. The experimental data with uncertainty is represented by the blue region, while the red line shows the numerical prediction of the gap evolution. 69

3.12 The impact response of an PEEK sphere dropped from heights $h_0 =$ 1.5 mm, 5 mm, 7 mm, and 10 mm. shows the variation of the vertical displacement h as a function of time t. The experimental data with uncertainty is represented by the blue region, while the red line shows the numerical prediction of the gap evolution. 70

3.13 Temporal evolution of the impact response of an acrylic sphere released from an initial height $h_0 = 1.5\,\text{mm}$ onto a sapphire substrate. The blue markers correspond to experimentally measured sphere displacement acquired using a Keyence laser sensor, while the green markers represent the contact radius evolution obtained from high-speed camera imaging. The response is segmented into three distinct regimes: (a) a bouncing phase characterized by successive impacts, (b) a vibration phase exhibiting damped oscillations, and (c) a static phase where a steady contact condition is attained. The highlighted intervals I-II-III identify representative impact events selected for detailed contact analysis, while the shaded region indicates the Hertzian contact limit (see Figure 3.14). 72

3.14 The numerically predicted contact areas (red lines) are compared with those obtained experimentally from high-speed cameras. The comparison is based on the first three maximum impacts and the static Hertzian limit at the end, with an initial drop height of $h_0 = 1.5\,\text{mm}$, as shown in Figure 3.13. During calibration, 1 *pixel* was measured as $=2.17mm$. 73

3.15 The contact radius a versus time is plotted for different drop heights ($h_0 = 1.5\,\text{mm}$ (a), $h_0 = 5\,\text{mm}$ (b), $h_0 = 7\,\text{mm}$ (c), and $h_0 = 10\,\text{mm}$ (d)). The numerical results (red lines) are compared with the experimental data (blue squares), both data sets being transformed so that the maximum contact radius occurs at $t_p = 0$. 74

3.16 Experimental comparison of the evolution of the contact radius for an acrylic sphere dropped from 10 mm at two different thermal conditions: at room temperature (blue squares) and heated to 39°C (red squares). Panels (a)–(c) show the first three maximum impacts at each height, while (d) presents the quasi-static Hertz limit. Each plot shows the contact radius a and the shifted contact time t_p, together with corresponding high-speed images of the contact area. 76

3.17 (a) Comparative plot of experimental and theoretical contact area evolution under stepwise loading for a PTFE ball on a sapphire surface: gray dots show raw data from the laser, blue solid curve is the smoothed response of the raw data, and red dashed line represents the Hertz prediction; horizontal dashed lines show the average contact radius at each load (0.5–5.5 kg), and vertical dashed lines show the applied load changes. (b) Evolution of theoretical contact area under stepwise loading. 78

A.1 Comparison between theoretical predictions and laser-based experimental measurements for acrylic ball drop impacts at four release heights: 1.5 mm (blue), 5 mm (red), 7 mm (green), and 10 mm (purple). In panel (a), colored dotted curves represent the theoretical results, while black curves correspond to the experimental laser measurements. Panel (b) presents magnified views of the first impact region for each drop height, highlighting the agreement between the theoretical model and experimental observations during the initial collision dynamics. 89

B.1 (a) Impact configuration showing the holder on a sapphire disk placed on a metal plate, the attached sphere, and the laser beam before and after impact (top), and the corresponding schematic of the drop device showing the vibrational state before and after impact (bottom). (b) Qualitative representation of the plate response after impact, showing the equilibrium position and oscillation due to wave propagation. 91

B.2 Measured plate vibration responses for drop heights of (a) 1.5 mm, (b) 5 mm, (c) 7 mm, and (d) 10 mm. The plate displacement near the sapphire disc is shown for impacts from Nylon (red), Acrylic (blue), PEEK (green), and PTFE (black) spheres. 93

C.1 General illustrations of the experimental evolution of vertical displacement and contact radius for an acrylic sphere impacting a sapphire substrate at different drop heights ($h_0 = 1.5\,\mathrm{mm}, 5\,\mathrm{mm}, 7\,\mathrm{mm}, 10\,\mathrm{mm}$). The blue curves show the laser-measured displacement, while the green marks show the contact radius obtained based on image processing from high-speed images, respectively, highlighting the relationship between global motion and contact evolution. 95

D.1 DICe reference frame: subset grid (yellow) and reference line (blue) used to track displacement. 97

D.2 Calibration ruler on the sapphire disc, imaged with the camera positioned beneath the disc. The 461-pixel distance corresponds to a 1 mm reference interval. 99

Introduction

The study of the mechanical and tribological properties of hard and soft viscoelastic materials has become a particular focus and has been the subject of extensive research in recent years. Thus, such viscoelastic materials include rubber-based composites [1, 2], thermoplastics [3, 4], and biological tissues [5, 6, 7, 8], hydrogels, and micro- and nano-scale polymer structures [9, 10, 11], which are widely used in both natural and engineered systems. Their time-dependent mechanical response arises from a combination of elastic energy storage and viscous dissipation mechanisms, which is characterised by stress relaxation, creep, rate-dependent stiffness, and hysteresis. This property of the materials further expands their scope of application. These properties govern how the materials deform and dissipate energy under loading, making viscoelasticity essential in applications such as biomedical devices [12], tribological systems, vibration-damping components [13, 14], and durable polymers [15, 16, 17], and 3D printing [18, 19], among others, enabling their use in a wide range of applications. The accurate characterisation of viscoelastic properties plays a crucial role in fields such as prosthetics [20], tissue engineering [21], and diagnostics [22]. This is mainly due to the close relationship between mechanical response and physiological function in biomedical applications.

The interaction between deformable viscoelastic bodies and rigid surfaces is considered one of the fundamental problems of contact mechanics. In such systems, viscoelasticity leads to time-dependent deformation, hysteresis, and energy dissipation, which are factors that strongly influence performance indicators such as friction, wear, vibration damping, and impact response. For this reason, the study of such effects in contact mechanics is of great importance in both classical and new engineering applications [23, 24, 25, 26]. For example, in tyre–road interaction [27, 28, 29], compliant interfaces [30, 31, 32], and in damping or protective systems [33, 34], these effects play a special role. Despite extensive research, the accurate modelling of viscoelastic contact remains a challenging and highly sought-after area of study due to the interplay between material rheology, contact geometry, and the loading history.

The most commonly used conventional method for determining the viscoelastic properties of materials is Dynamic Mechanical Analysis (DMA) [35], which provides the material's fundamental viscoelastic properties under controlled conditions.

However, this method often requires carefully prepared samples. For example, cutting small specimens from the materials for analysis, conducting analyses at high temperatures, etc. At the same time, it may not be suitable for in-situ applications or for determining material properties in complex geometries [36, 37]. This makes the use of highly sensitive materials for such behaviours impossible. For this reason, indentation-based approaches [38, 39, 40] offer a non-destructive alternative for localised investigation of material behaviour in components, although their interpretation is often based on simplified elastic assumptions. Similarly, classical contact theories, such as the Hertzian solutions [41], are limited to elastic and quasi-static conditions. All this stimulates the development of advanced numerical methods, such as viscoelastic extensions [42, 43] and, in particular, Boundary Element approaches [39, 40, 44, 37]. These methods establish an efficient link between material behaviour and measurable contact quantities.

Most existing studies only provide indirect insights into local interface mechanisms. For example, they are based on globally observed phenomena such as force, displacement and recovery [45, 46, 47, 48, 49]. In contrast, the evolution of the contact area, which is directly related to deformation and energy dissipation, remains largely unexplored, particularly in dynamic conditions, especially the simultaneous acquisition of various experimental data. For example, under highly transient conditions, it is necessary to simultaneously measure both the global kinematics of the colliding body and the local evolution of the contact interface. At the same time, the demand for such fast, non-destructive, and practically applicable methods that can characterise the viscoelastic behaviour under real service conditions is increasing across all fields. This is also confirmed by recent developments in contact-based testing systems [33, 50].

In this context, this dissertation investigates two complementary problems in viscoelastic contact mechanics. The first is the characterisation of viscoelastic materials through harmonic and quasi-static indentation, and the second is the analysis of their dynamic response under normal impact.

The thesis is structured to gradually develop both the theoretical framework and the application-oriented approaches. This enables the analysis of viscoelastic contact phenomena. Thus, Chapter 1 focuses on the fundamental theoretical knowledge in the research field, presenting the fundamentals of linear viscoelasticity, as well as the formulations and constitutive principles governing the time-dependent material response. Chapter 2 pays special attention to viscoelastic indentation under harmonic (cyclic) and stress relaxation loading conditions, and builds upon this foundation to present the mathematical theory that forms the basis of the numerical technique. In particular, a Boundary Element (BEM) framework is developed that establishes a direct link between material rheology and contact mechanics by incorporating viscoelasticity through time-dependent convolution integrals based on the creep function. The use of periodic Green's functions, an essential component of the numerical approach, significantly increases computational efficiency whilst preserving the key physics of periodic contact problems—particularly during perforation with periodically distributed matrices. The established model incorporates the development of contact pressure, displacement fields, and the contact area under a time-dependent loading. This allows for the analysis of transient relaxation phenomena, whilst also enabling the study of steady-state cyclic behaviour. The multi-frequency effects resulting from changes in the contact conditions can also be analysed with this method. The work dissipated during harmonic indentation is evaluated, in addition to the numerical representation, through a unique analytical expression that links the hysteretic losses directly to the complex viscoelastic modulus. The proposed framework is supported by a dedicated experimental campaign designed to replicate the conditions considered in the numerical simulations. The experiments are carried out on nitrile butadiene rubber (NBR) using a custom-designed sinusoidal indenter. These experiments offer a strong agreement between analytical, numerical, and experimental results, validating the proposed methodology.

In Chapter 3, the study is extended to dynamic impact conditions. The normal impact of a viscoelastic sphere on a rigid substrate is first analysed using a numerical method. Subsequently, a dedicated experimental investigation is conducted using high-speed imaging and a laser position sensor, taking into account the conditions established in the numerical method. Dynamic impact tests are performed on various materials, including PTFE, PEEK, nylon, and acrylic. Initially, validation between the laser sensor result and the high-speed imaging camera result is studied using PTFE material, while also investigating the impact of PTFE spheres in a static state. The experimental work continues by comparing laser and numerical results for PEEK, Nylon and Acrylic spheres dropped from various heights. Special attention is paid to the transparent acrylic spheres to directly observe the development of the contact area. Additionally, experiments are conducted at elevated temperatures to investigate the temperature-dependent effects on the acrylic spheres and to study the growth of the contact area. The strong agreement between the experiments and simulations confirms the validity of the proposed framework.

It should be stressed that several of the building blocks employed in this dissertation are not new in themselves: linear viscoelastic constitutive theory, DMA-based material characterisation, and Boundary Element formulations for viscoelastic contact have all been established in prior literature [38, 39, 40, 35]. The original contribution of this work lies not in proposing new constitutive theory, but in the integration of these established tools into a single, experimentally validated framework, and specifically in two aspects that have received limited attention to date: (i) the combined analytical–numerical–experimental treatment of oscillatory indentation, including a dedicated analytical formulation for the dissipated energy; and (ii) the direct optical measurement of the transient contact radius during impact, alongside the global kinematic response, which most existing studies do not capture simultaneously. The contribution of the thesis should therefore be read as a validated integration and extension of existing methodologies to previously underexplored loading conditions, rather than as a new theoretical framework.

The novelty of this dissertation lies in the development of a unified and predictive framework for viscoelastic contact analysis, which combines numerical modelling with analytical formulae in a single approach. The results demonstrate that viscoelastic behaviour can be effectively characterised and predicted through simple, non-destructive contact-based tests. This allows for the avoidance of complex experimental procedures or invasive sample preparation, such as material cutting. Taking into account the variation of the contact area allows for a more accurate validation of the models and a better understanding of the mechanisms of energy dissipation. This approach is particularly relevant for fields such as tyre analysis, biomedical applications, and the design of damper systems.

Chapter 1

Foundations of Linear Viscoelasticity

As noted in the introduction, viscoelastic materials are widely used in both scientific research and various industrial fields due to their time-dependent and energy-dissipative characteristics [6, 7, 51, 52, 53, 54].In engineering, such materials are used in mechanical and tribological systems, such as belts, gears, and polymer-based or journal bearings, as their rheological response affects friction, load distribution, and energy loss [55, 31, 56]. Furthermore, their light weight compared to metals, wear resistance, corrosion protection, ease of manufacture and low cost make them widely applicable in the automotive, aerospace, electronics and robotics industries, as well as in polymer coatings that enhance thermal stability [57, 58, 59, 60, 61, 62, 63]. In biomechanics, such viscoelastic materials play a key role in biological tissues such as skin, cartilage, tendons, and cellular structures, supporting important physiological functions due to their ability to relieve stress and withstand repeated loading [64, 65, 66, 67, 68]. At the same time, the controlled energy dissipation and damping capability of such materials is used in a wide range of applications, including vibration control systems [69, 70], seismic isolation devices [71, 72], soft robotic grippers [73, 74], sealing systems [75], and various damping elements [76], among a wide range of applications.

Considering their extensive range of applications and future prospects, the study of viscoelastic materials is of paramount importance. In particular, the investigation of the contact mechanics of such materials is of even greater significance. For example, by monitoring changes in the penetration depth or the applied force over time, indentation tests, which are an alternative to material characterisation methods such as DMA, are widely used to evaluate the viscoelastic properties of materials. Fundamental material properties such as relaxation times and viscoelastic moduli can be determined through these studies by Hunter [43], Person [77], Christensen [78, 35], and Grosch [79], which provide important insights into creep and relaxation processes. It is essential to incorporate numerical and analytical models to interpret these studies and to correlate the observed mechanical response with the material's fundamental constitutive characteristics.

Given the wide range of applications of these materials and the inherent complexity of viscoelastic behaviour, it is crucial to develop a robust theoretical framework that can explain their mechanical response. Viscous fluid models describe purely dissipative behaviour, whereas classical elasticity theory assumes an instantaneous and inverse relationship between stress and strain. However, since viscoelastic materials combine the properties of both systems, the response depends on both the history of the applied loads and the current state of deformation. The constitutive description of viscoelastic materials must include the time-dependent interactions between stress and strain [80, 81]. These relationships are typically described by integral formulations involving relaxation or creep functions.

A useful description of the time-dependent mechanical response of viscoelastic materials can be obtained by considering the condition of harmonic loading, where the deformation varies sinusoidally with time [82, 78, 83, 84]. The strain history can be defined as $\varepsilon(t) = \varepsilon_A \sin(\omega t)$, where ε_A denotes the strain amplitude and ω represents the angular frequency of oscillation. The stress response in the viscoelastic material is also defined in a sinusoidal form, but is shifted in phase relative to the applied strain. This is expressed as $\sigma(t) = \sigma_A \sin(\omega t - \delta)$, where σ_A is the stress amplitude and δ denotes the phase lag between stress and strain. The magnitude of this phase angle characterises the relative contributions of elastic energy storage and viscous energy dissipation within the material [78, 82].

In the case of purely elastic behaviour, the stress and strain remain perfectly in-phase, resulting in $\delta = 0°$. This reflects the instantaneous and inverse relationship described by Hooke's law [83, 85]. In this case, the mechanical energy supplied during loading is completely stored elastically and is recovered during unloading. In purely viscous behaviour, on the other hand, the stress response is characterised by being proportional to the strain rate, $\sigma(t) = \eta\dot{\varepsilon}(t)$, where η is the viscosity of the material. Under sinusoidal loading conditions, the relationship between stress and strain creates a phase difference of $\delta = 90°$. This is associated with the mechanical response being entirely dissipative, and the applied energy is irreversibly converted into heat [83, 82, 78]. Most materials found in nature, particularly polymers and biological tissues, exhibit viscoelastic behaviour characterised by phase lag, $0° < \delta < 90°$.

In this intermediate regime, the material combines both elastic deformation mechanisms that store energy and viscous properties that dissipate energy due to molecular rearrangements and internal friction. These three states are schematically depicted in Figure 1.1, where we can clearly see the role of the stress-strain curves in characterizing the mechanical behavior under oscillating loading with a phase angle of δ.

In applied mechanics, the development of theoretical models for viscoelastic materials is considered one of its main areas, where linear viscoelasticity provides a mathematically convenient framework for describing polymeric materials under

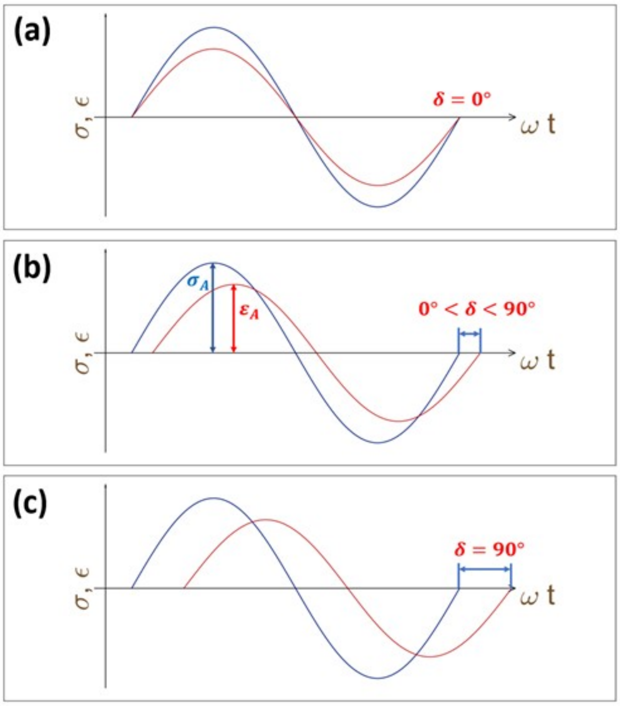

Figure 1.1: Sinusoidal stress–strain responses under harmonic loading: (a) Ideal elastic — stress and strain are in phase ($\delta = 0°$); (b) Viscoelastic — stress is delayed ($0° < \delta < 90°$), indicating both elastic storage and viscous dissipation; (c) Ideal viscous — stress is proportional to the rate of strain ($\delta = 90°$).

moderate deformations. It includes important concepts such as constitutive relations for time-dependent deformation, as well as creep and relaxation functions, and rheological models, which are the basis for many analytical and computational methods, such as finite elements and boundary elements.

To study the constitutive relations governing viscoelastic materials, let us consider a deformable body in its initial, undeformed state. Let us assume that this body is attached to a fixed reference frame that is at rest.

Let $\mathbf{X}_0$ be the coordinates of a material point in the undeformed state, and $\mathbf{r}(t')$ be the coordinates of that point in the deformed state at time t'. Taking these into account, we can express the displacement vector as $\mathbf{u}(t') = \mathbf{r}(t') - \mathbf{X}_0$ where t' is the time variable such that $-\infty < t' < t$, with t denoting the current time.

Within the framework of infinitesimal deformation theory, the displacement gradients are assumed to be sufficiently small compared with unity [78], such that $\varepsilon = \sup_{t'} |\partial u_i(t')/\partial X_{0j}| \ll 1$. Under these conditions, the infinitesimal strain tensor is defined as $\varepsilon_{ij} = \frac{1}{2}\left(\partial u_i/\partial X_{0j} + \partial u_j/\partial X_{0i}\right)$ which describes the local deformation of the continuum body by quantifying the relative displacement of neighbouring material points.

The stress field that occurs within a material is determined by the traction vector acting on its infinitesimal surface element dS, and if $\mathbf{n}$ here denotes the unit normal vector of this surface, then the tension vector $\mathbf{F}$ acting on the surface element is expressed namely $F_i = \sigma_{ij} n_j dS$, where σ_{ij} is the Cauchy stress tensor [86]. The relationship between the orientation of a surface element and the traction acting on it is related to the stress tensor. Thus, the application of linear momentum balance to an infinitesimal tetrahedral element is related as $\sigma_i = \sigma_{ij} n_j$. Furthermore, imposing the balance of angular momentum implies that the stress tensor must be symmetric, namely $\sigma_{ij} = \sigma_{ji}$.

Once the kinematic and stress measures are determined, the viscoelastic constitutive law can be introduced. As we noted earlier, in linear viscoelasticity, the current stress state incorporates the entire past history of strain, which is expressed as [78]:

$$\sigma_{ij}(t) = \underset{s=0}{\overset{\infty}{\mathcal{F}_{ij}}} \left(\varepsilon_{kl}(t-\tau), \varepsilon_{kl}(t)\right) \tag{1.1}$$

where $\mathcal{F}_{ij}$ is considered to be a linear tensor-valued operator that transforms each strain history $\varepsilon_{ij}(t)$ into a related stress history $\sigma_{ij}(t)$, where the time $-\infty < t < \infty$.

When a linear and continuous stress history is considered and the Riesz representation theorem is applied, the expression Equation (1.1) is presented in the form of a Stieltjes integral:

$$\sigma_{ij}(t) = \int_0^{\infty} \varepsilon_{kl}(t-\tau)\, d\mathcal{G}_{ijkl}(\tau), \tag{1.2}$$

Moreover, due to the symmetry properties of the stress and strain tensors, the relaxation tensor satisfies $\mathcal{G}_{ijkl}(t) = \mathcal{G}_{jikl}(t) = \mathcal{G}_{ijlk}(t)$. Equation (1.2) further indicates that the constitutive relation is invariant under a shift in the time scale, i.e., it exhibits time-translation invariance. In addition, assuming that $\varepsilon_{kl}(t) = 0$ for $t < 0$, and that $\mathcal{G}_{ijkl}$ together with its first derivative are continuous on the interval $0 \leq t < \infty$ [78, 35, 87], Equation (1.2) can be expressed as:

$$\sigma_{ij}(t) = \mathcal{G}_{ijkl}(0)\, \varepsilon_{kl}(t) + \int_0^t \varepsilon_{kl}(t-\tau) \frac{d\mathcal{G}_{ijkl}(\tau)}{d\tau}\, d\tau. \tag{1.3}$$

Introducing the change of variable $\zeta = t - \tau$, the constitutive relation becomes

$$\sigma_{ij}(t) = \int_0^t \mathcal{G}_{ijkl}(t-\zeta) \frac{d\varepsilon_{kl}(\zeta)}{d\zeta}\, d\zeta. \tag{1.4}$$

The above formula is a mathematical expression of the *Boltzmann superposition principle*. According to this principle, the stress at the current time is obtained by superimposing the contributions of all past strain increments, each weighted by the relaxation function. Thus, the function $\mathcal{G}_{ijkl}(t)$ is an important material parameter that characterizes how the stress decreases with time after the application of a uniform step strain. For isotropic materials, this relaxation behavior is expressed by scalar functions such as the shear relaxation modulus $\mathcal{G}(t)$.

A complementary constitutive relationship can be formulated by expressing the strain in terms of the time history of the stress [88, 35]. In this case, the strain response is expressed as:

$$\varepsilon_{ij}(t) = \int_0^t \mathcal{J}_{ijkl}(t-\zeta)\frac{d\sigma_{kl}(\zeta)}{d\zeta}\,d\zeta, \tag{1.5}$$

where $\mathcal{J}_{ijkl}(t)$ is the *creep compliance function*. This function describes the strain response of the material to a unit step in stress.

The relaxation modulus and the creep compliance are not independent functions and are determined by the Laplace transform of the constitutive equations [89, 90]. Denoting the Laplace transforms of $\mathcal{G}(t)$ and $\mathcal{J}(t)$ as $\overline{\mathcal{G}}(\varrho)$ and $\overline{\mathcal{J}}(\varrho)$ respectively, the following relation holds as $\overline{\mathcal{G}}(\varrho)\,\overline{\mathcal{J}}(\varrho) = \varrho^{-2}$.

The following integral is obtained by applying the inverse Laplace transform and using the convolution theorem [76].

$$\int_0^t \mathcal{J}(t-\tau)\,\mathcal{G}(\tau)\,d\tau = t. \tag{1.6}$$

Alternatively, the same relation can be written as

$$\mathcal{J}(0)\mathcal{G}(t) + \int_0^t \frac{d\mathcal{J}(\tau)}{d\tau}\,\mathcal{G}(t-\tau)\,d\tau = 1. \tag{1.7}$$

In many practical situations, the creep function is expressed in terms of a relaxation time spectrum. In this formulation, the creep function can be written as [78]s ,$\mathcal{J}(t) = \mathcal{H}(t)/E_0 - \mathcal{H}(t)\int_0^\infty C(\tau)e^{-t/\tau}\,d\tau$, where E_0 and E_∞ denote the rubbery and glassy elastic moduli respectively, $C(\tau)$ is the creep spectrum, τ represents the relaxation time, and $H(t)$ is the Heaviside step function ensuring the causality condition.

For numerical applications, the creep spectrum is often discretized so that the creep function becomes [78], $\mathcal{J}(t) = \mathcal{H}(t)/E_0 - \mathcal{H}(t)\sum_{k=1}^{n} C_k e^{-t/\tau_k}$, where C_k are the creep coefficients and τ_k the corresponding relaxation times.

Such representations are widely employed in numerical simulations of viscoelastic contact problems, where the time–dependent mechanical behaviour of the material must be incorporated into the governing equations of contact mechanics.

Another important property of viscoelastic materials is the presence of memory effects. In other words, the current mechanical response of the material depends on its entire loading history. This phenomenon occurs due to internal physical processes of the material, such as molecular rearrangements, viscous flow mechanisms, and internal stress relaxation. Mathematically, this behavior can be characterized by convolution integrals present in the viscoelastic constitutive equations. Thus, the stress at a given moment is determined by the weighted sum of the previous deformation increments, and the relaxation modulus plays the role of a weighting function in this weighting.

At the same time, it should be noted that in most real materials, the effect of events that occurred in the distant past weakens with time, a phenomenon called *fading memory*. This phenomenon has been extensively studied by Vito Volterra [91] and Bernard D. Coleman [92, 93]. According to this principle, deformation changes that occurred in the recent past have a stronger effect on the current stress state, while the effect of the distant past weakens with time. The fading memory condition imposes important restrictions on the possible forms of the relaxation modulus and creep function. In particular, the derivative of the relaxation modulus should decrease with time [78].

$$\left|\frac{d\mathcal{G}}{dt}(t_1)\right| \leq \left|\frac{d\mathcal{G}}{dt}(t_2)\right|, \qquad t_1 > t_2 > 0. \tag{1.8}$$

An analogous condition holds for the creep function,

$$\left|\frac{d\mathcal{J}}{dt}(t_1)\right| \leq \left|\frac{d\mathcal{J}}{dt}(t_2)\right|. \tag{1.9}$$

These inequalities ensure that the weighting of past events decreases continuously with time, reflecting the physical relaxation processes occurring in the material.

One important condition to consider is the *causality principle* [78, 35]. According to this principle, the response of the material can not depend on future loading events. In mathematical terms, this means that the creep and relaxation functions must vanish for negative time values [89, 78], $\mathcal{J}(t) = 0, \qquad \mathcal{G}(t) = 0 \quad \text{for } t < 0.$

1.1 Constitutive Relations Under Steady-State Conditions

In this section, we consider a viscoelastic body subjected to steady-state harmonic oscillations, a condition of central importance in many experimental and practical situations. We examine the specific case in which the strain history is given by $\varepsilon(t) = \varepsilon_0 \exp(i\omega t)$, where ε_0 denotes the strain amplitude and ω the angular frequency of the imposed deformation. As shown in Refs. [82, 83], under these conditions the stress and strain oscillate at the same frequency but with a phase lag between them.

In linear viscoelasticity, the stress response is governed by a relaxation modulus $\mathcal{G}(t)$, which can be decomposed as $\mathcal{G}(t) = \tilde{\mathcal{G}} + \hat{\mathcal{G}}(t)$, where $\tilde{\mathcal{G}}$ is the equilibrium modulus and $\hat{\mathcal{G}}(t)$ is the transient part that vanishes as $t \to \infty$ [82]. Using the hereditary integral formulation [82, 78], the stress under harmonic strain is given by

$$\sigma(t) = \tilde{\mathcal{G}}\,\varepsilon_0 e^{i\omega t} + i\omega\varepsilon_0 \int_{-\infty}^{t} \hat{\mathcal{G}}(t-\tau)\, e^{i\omega\tau}\, d\tau, \tag{1.10}$$

reflecting the combination of an instantaneous elastic contribution from $\tilde{\mathcal{G}}$ and a history-dependent viscoelastic contribution from relaxation [76].

By simplifying the convolution integral by introducing the variable $\zeta = t - \tau$, the stress can be expressed in a simpler form:

$$\sigma(t) = \left[\tilde{\mathcal{G}} + \omega \int_0^{\infty} \hat{\mathcal{G}}(\zeta)\sin(\omega\zeta)\, d\zeta + i\omega \int_0^{\infty} \hat{\mathcal{G}}(\zeta)\cos(\omega\zeta)\, d\zeta\right] \varepsilon_0 e^{i\omega t}. \tag{1.11}$$

Since stress and strain oscillate at the same frequency in the steady-state regime, then the frequency-dependent coefficient, the *complex modulus* [82, 83]., is introduced, which is expressed as $\sigma(t) = \mathcal{G}^*(\omega)\,\varepsilon_0 e^{i\omega t}$. The complex modulus $\mathcal{G}^*(\omega)$ encapsulates the entire dynamic mechanical response of the viscoelastic material and is given by [82, 78]

$$\mathcal{G}^*(\omega) = \tilde{\mathcal{G}} + \omega \int_0^{\infty} \hat{\mathcal{G}}(\zeta)\left[\sin(\omega\zeta) + i\cos(\omega\zeta)\right] d\zeta. \tag{1.12}$$

This quantity is generally complex and can be decomposed into real and imaginary components [82] - $\mathcal{G}^*(\omega) = \mathcal{G}'(\omega) + i\,\mathcal{G}''(\omega)$. The real part $\mathcal{G}'(\omega)$, known as the *storage modulus*, represents the elastic energy stored in the material during each oscillation period [82, 84]. This parameter characterizes the ability of the material to store energy and restore it after the load is removed. Mathematically, it is defined as:

$$\mathcal{G}'(\omega) = \tilde{\mathcal{G}} + \omega \int_0^{\infty} \hat{\mathcal{G}}(\zeta)\sin(\omega\zeta)\, d\zeta. \tag{1.13}$$

The imaginary part $\mathcal{G}''(\omega)$ is known as the *loss modulus* and characterizes the viscous energy losses occurring within the material [82, 83]. This is due to the irreversible energy dissipation due to internal friction and molecular rearrangements during deformation. The loss modulus is defined as:

$$\mathcal{G}''(\omega) = \int_0^{\infty} \omega\, \hat{\mathcal{G}}(\zeta)\cos(\omega\zeta)\, d\zeta. \tag{1.14}$$

These two parameters fully characterize the dynamic behavior of viscoelastic materials under harmonic loading [82, 81]. The storage modulus reflects elasticity, while the loss modulus accounts for viscous energy dissipation.

The behavior of these modules is highly dependent on excitation frequency [82, 83]. Analysis of the above expressions allows investigation of both very low and very high frequency cases. At zero frequency, or under quasi-static loading, the storage modulus decreases to the $\mathcal{G}'(0) = \tilde{\mathcal{G}} = \mathcal{G}(t)\big|_{t\to\infty}$, while the loss modulus vanishes $\mathcal{G}''(0) = 0$.

At low frequencies, the material reaches equilibrium and behaves as an elastic solid governed by the long-term relaxation modulus, whereas at high frequencies, deformation occurs too rapidly for relaxation to take place, and the response approaches the instantaneous elastic limit, with $\mathcal{G}'(\infty) = \tilde{\mathcal{G}}+\hat{\mathcal{G}}(0) = \mathcal{G}(t)\big|_{t\to 0}$, $\mathcal{G}''(\infty) = 0$.

These limits reveal the dual nature of viscoelastic materials: at low frequencies the behavior may be fluid-like or solid-like depending on the relaxation spectrum, whereas at high frequencies the response is always elastic, since insufficient time remains for molecular rearrangement. Figure 1.2 qualitatively illustrates the storage and loss moduli for a typical viscoelastic material with a single relaxation time.

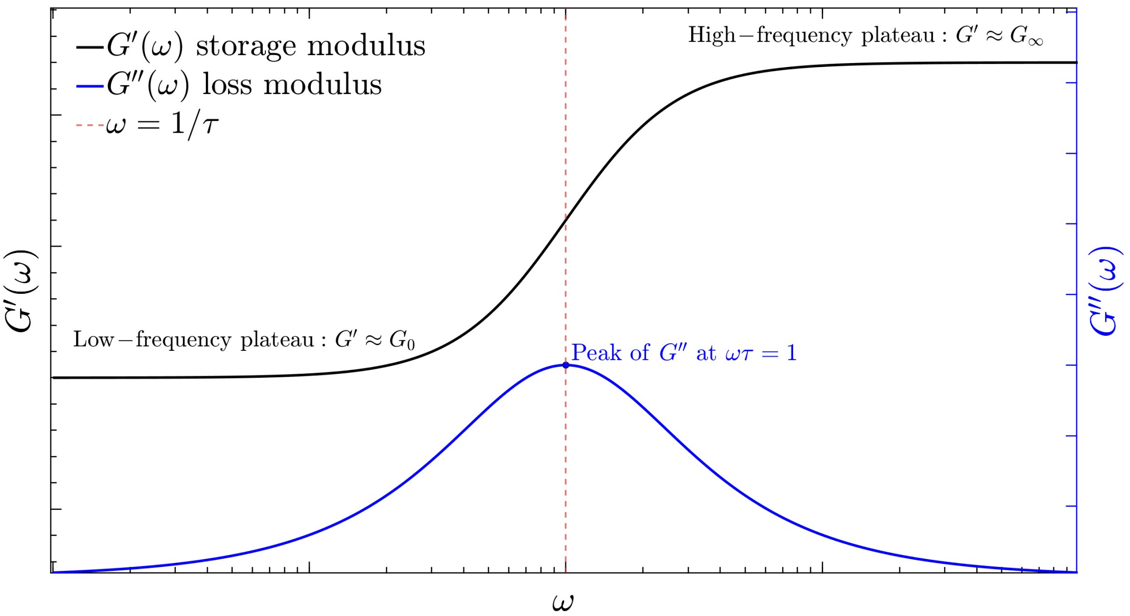

Figure 1.2: Frequency dependence of the complex modulus for a material with a single relaxation time τ. The storage modulus $\mathcal{G}'(\omega) = \mathrm{Re}\,\mathcal{G}^*(\omega)$ (black) quantifies stored elastic energy, while the loss modulus $\mathcal{G}''(\omega) = \mathrm{Im}\,\mathcal{G}^*(\omega)$ (blue) quantifies viscous dissipation. $\mathcal{G}'(\omega)$ rises from the relaxed modulus $\mathcal{G}_0$ at low frequencies to the unrelaxed modulus $\mathcal{G}_\infty$ at high frequencies, while $\mathcal{G}''(\omega)$ peaks at $\omega\tau \approx 1$, where the loading time scale matches the material's relaxation time.

The relationship between the storage and loss moduli provides important insights about the energy dissipation mechanisms. During cyclic loading, the stress does not reach its maximum at the same time as the strain, but a phase difference is created between them. This phase lag indicates the energy dissipated in the material during each cycle and is directly related to the ratio of the loss modulus to the storage modulus.

The stress–strain relation can therefore be written in an alternative and physically meaningful form

$$\sigma(t) = |\mathcal{G}^*(\omega)|\ \varepsilon_0 e^{i\omega t+\delta(\omega)}. \tag{1.15}$$

In this representation, $|\mathcal{G}^*(\omega)|$ denotes the magnitude of the complex modulus and the quantity, $\delta(\omega) = \arctan(\mathcal{G}''(\omega)\,[\mathcal{G}'(\omega)]^{-1})$, represents the phase lag between stress and strain.This phase difference indicates that some of the mechanical energy supplied during loading is dissipated as heat within the material. The energy loss per cycle is proportional to the loss modulus, resulting in the hysteresis behavior characteristic of cyclic loading.

A frequency-dependent description of viscoelasticity is central to the dynamic mechanical behavior of soft materials, particularly in oscillatory contacts, cyclic indentation, and vibration damping. In the indentation problems considered in this thesis, the complex modulus governs the relationship between oscillatory indentation depth and contact force, thereby determining the stiffness and energy dissipation of the system [42, 94]. This framework underlies most numerical models of viscoelastic contact mechanics and the interpretation of harmonic indentation and impact experiments.

1.2 Thermoviscoelastic Behavior of Materials

The previous discussion shows that viscoelastic materials are intrinsically dissipative: part of the mechanical energy supplied during deformation is stored, while the rest is lost as heat. A consistent description of viscoelasticity must therefore comply with the principles of thermodynamics, which is the basis of *thermoviscoelasticity*, where constitutive laws follow from both the balance equations of continuum mechanics and the second law of thermodynamics. Although the present analysis is restricted to isothermal conditions, this is a special case of the broader thermoviscoelastic theory, which we introduce first.

The theory rests on the following assumptions: infinitesimal deformations, so that deformation and displacement gradients are small; a continuum description with density ρ and a temperature field smooth in space and time; and causality, whereby the current response depends only on past deformation and temperature history, not on future states. These standard assumptions of linear thermoviscoelasticity underlie the constitutive framework used later in the viscoelastic contact and indentation models.

The starting point is the local balance of energy for an infinitesimal body [95, 96, 97], which may be written as

$$\sigma_{ij}\dot{\varepsilon}_{ij} - q_{i,i} + \rho r - \rho\left(\dot{\psi} + \theta\dot{s} + \dot{\theta}s\right) = 0. \tag{1.16}$$

Here, ρ is the mass density, r the heat supply per unit mass, ψ the Helmholtz free energy per unit mass, s the entropy per unit mass, θ the absolute temperature, and q_i the components of the heat flux vector, with $\sigma_{ij}\dot{\varepsilon}_{ij}$ the mechanical power density and $q_{i,i}$ the divergence of the heat flux. This equation expresses that the energy supplied to the body is balanced by its storage, entropy generation, and heat transfer—a balance that is essential in viscoelastic materials, where internal relaxation continually converts mechanical work into dissipated energy.

The second thermodynamic ingredient is the local entropy production inequality, commonly written in the form of the Clausius–Duhem inequality [88, 96, 86],

$$\rho\dot{\theta}\, s - \rho r + q_{i,i} - q_i\left(\frac{\theta_{,i}}{\theta}\right) \geq 0. \tag{1.17}$$

This inequality implies that entropy production cannot be negative, which constrains the admissible forms of the relaxation functions, free energy, and temperature–strain relations, ruling out constitutive equations that would imply spontaneous energy generation or other thermodynamically inadmissible behavior.

Crucially, because the material has memory, its free energy depends not only on the instantaneous deformation and temperature but on their entire histories. Assuming $\varepsilon_{ij}(t)$ and $\theta(t)$ are continuous on $(-\infty, \infty)$ with $\varepsilon_{ij}(t) \to 0$ and $\theta(t) \to \theta_0$ as $t \to -\infty$, the Stone–Weierstrass theorem allows the free energy to be approximated as a polynomial of linear functionals of these histories, which the Riesz representation theorem expresses as Stieltjes integrals with bounded-variation kernels. The full derivation is omitted for brevity, but it leads directly to the thermodynamic inequality [78].

$$\Lambda - q_i\left(\frac{\Theta_{,i}}{\theta_0}\right) \geq 0, \tag{1.18}$$

where $\Theta(t) = \theta(t) - \theta_0$, is the temperature deviation from the base temperature θ_0, and Λ denotes the rate of energy dissipation.

The dissipation rate is then written as

$$\begin{aligned}\Lambda = &-\frac{1}{2}\int_{-\infty}^{t}\int_{-\infty}^{t}\frac{\partial}{\partial t}\mathcal{G}_{ijkl}(t-\tau, t-\eta)\,\frac{\partial\varepsilon_{ij}(\tau)}{\partial\tau}\frac{\partial\varepsilon_{kl}(\eta)}{\partial\eta}\,d\tau d\eta \\ &+\int_{-\infty}^{t}\int_{-\infty}^{t}\frac{\partial}{\partial t}\mathcal{K}_{ij}(t-\tau, t-\eta)\,\frac{\partial\varepsilon_{ij}(\tau)}{\partial\tau}\frac{\partial\Theta(\eta)}{\partial\eta}\,d\tau d\eta \\ &+\frac{1}{2}\int_{-\infty}^{t}\int_{-\infty}^{t}\frac{\partial}{\partial t}\mathcal{M}(t-\tau, t-\eta)\,\frac{\partial\Theta(\tau)}{\partial\tau}\frac{\partial\Theta(\eta)}{\partial\eta}\,d\tau d\eta.\end{aligned} \tag{1.19}$$

In this expression, $\mathcal{G}_{ijkl}(t, t')$ denotes the mechanical relaxation kernel, $\mathcal{K}_{ij}(t, t')$ denotes the thermo-mechanical interaction kernel, and $\mathcal{M}(t, t')$ denotes the thermal contribution. These kernels satisfy the causality principle: they are zero for any negative time argument and remain continuous for positive times. Physically, the first term Λ represents the mechanical dissipation associated with viscoelastic relaxation, the second term represents the interaction between the deformation and temperature histories, and the third term represents the thermal dissipation. This division shows that thermoviscoelasticity is not simply the sum of viscoelasticity and thermal conductivity but rather a fully interconnected thermo-mechanical system.

Because the contact and impact analyses in this dissertation are conducted under isothermal conditions, the general formulation is simplified by assuming a spatially uniform temperature field $\Theta_{,i} = 0$. Under this condition, Equation (1.17) reduces to $\Lambda \geq 0$, which is usually referred to as the dissipation inequality. In this case, the dissipation rate simplifies to

$$\Lambda = -\frac{1}{2}\int_{-\infty}^{t}\int_{-\infty}^{t} \frac{\partial}{\partial t}\mathcal{G}_{ijkl}(t-\tau, t-\eta)\,\frac{\partial \varepsilon_{ij}(\tau)}{\partial \tau}\frac{\partial \varepsilon_{kl}(\eta)}{\partial \eta}\,d\tau d\eta. \tag{1.20}$$

This expression highlights the primary thermodynamic constraint: energy dissipation during viscoelastic relaxation must remain non-negative. That is, the material either stores or loses energy, but cannot generate mechanical energy through internal relaxation.

A related condition in continuum mechanics is the non-negative work principle. Morton E. Gurtin and Ismael Herrera applied this principle to linear isothermal viscoelasticity [98]:

$$\int_{0}^{t} \sigma_{ij}(\tau)\,\frac{\partial \varepsilon_{ij}(\tau)}{\partial \tau}\,d\tau \geq 0. \tag{1.21}$$

This demonstrates that the work needed to deform a material from its initial state cannot be negative. By combining equations (1.16) and (1.17) under isothermal conditions, we obtain the following result:

$$-\rho\dot{\psi} + \sigma_{ij}\dot{\varepsilon}_{ij} \geq 0. \tag{1.22}$$

Integrating in time then gives

$$-\rho\psi + \int_{0}^{t} \sigma_{ij}(\tau)\,\dot{\varepsilon}_{ij}(\tau)\,d\tau \geq 0. \tag{1.23}$$

Recognizing that the left-hand side is directly connected with the rate of dissipation, the non-negative work requirement may equivalently be expressed as

$$\int_{0}^{t} \Lambda(\tau)\,d\tau \;\geq\; 0. \tag{1.24}$$

The Helmholtz free energy per unit mass, interpreted here as the stored energy, is written as

$$\psi = \frac{1}{2}\int_{-\infty}^{t}\int_{-\infty}^{t} \mathcal{G}_{ijkl}(t-\tau, t-\eta)\,\dot{\varepsilon}_{ij}(\tau)\,\dot{\varepsilon}_{kl}(\eta)\,d\tau d\eta. \tag{1.25}$$

These relations indicate that requiring positive stored free energy is a stricter constraint than the non-negative work condition $\rho\psi \geq 0$ ensures non-negative work, the reverse does not always hold.Thus, non-negative free energy is viewed as a more stringent and physically reasonable constitutive condition. For a discontinuous deformation history such as $\varepsilon_{ij}(t) = \bar{\varepsilon}_{ij}\,\mathcal{H}(t)$, where $\mathcal{H}(t)$ is the Heaviside step function, the condition $\rho\psi \geq 0$ imposes $\mathcal{G}_{ijkl}(t, t') \geq 0$. Equation (1.20) requires the relaxation function's derivative to be negative, and the "fading memory" assumption requires its second derivative with respect to time to be non-negative, meaning the function must be concave upwards. Although standard, these conditions are essential to ensure that the constitutive kernels are thermodynamically consistent and physically justified.

Once general thermodynamic constraints are established, focus shifts to the temperature dependence of viscoelastic properties, which is a key characteristic of polymeric and soft materials. The viscoelastic functions in the constitutive law are highly temperature-dependent. The thermoviscoelastic approach described above considers material functions at a fixed base temperature θ_0, but does not address small deviations from this temperature without further assumptions. In order to include the effect of general temperature changes in a more systematic way, it is appropriate to introduce concepts related to the frequency response of viscoelastic materials.

Figure 1.4 compares the dynamic behavior of four polymer classes—amorphous and semicrystalline thermoplastics, elastomers, and thermosets—via the storage modulus $\mathcal{G}'(\omega)$ (solid) and loss factor $\tan\delta(\omega) = \mathcal{G}''(\omega)/\mathcal{G}'(\omega)$ (dashed).

In amorphous thermoplastics, $\mathcal{G}'(\omega)$ drops sharply at the glass transition, where $\tan\delta$ peaks, after which the material turns rubbery or flows. Semicrystalline thermoplastics show a similar but weaker drop, since crystalline regions sustain stiffness until melting causes a second, sharper decline. Elastomers, with a low glass transition temperature, show a broad rubbery plateau before $\mathcal{G}'(\omega)$ gradually falls, the $\tan\delta$ peak marking the glassy-to-rubbery crossover. Thermosets retain a high, nearly constant $\mathcal{G}'(\omega)$, do not melt, and show only a weak $\tan\delta$ peak, reflecting limited chain mobility.

In terms of $\mathcal{G}^*(\omega)$, three regimes appear: a stiff glassy regime at high frequency, a mobile rubbery regime at low frequency, and a transition region—tied to the frequency-dependent θ_g—where the modulus changes fastest and $\tan\delta$ shows its main (α) peak from segmental relaxation, sometimes with smaller β- and γ-peaks from more localized motion. The γ-peak reflects bending/twisting of short segments; the β-peak, at higher temperature, reflects larger-segment or side-group motion. Overlap of the α- and β-peaks signals thermorheological complexity, where

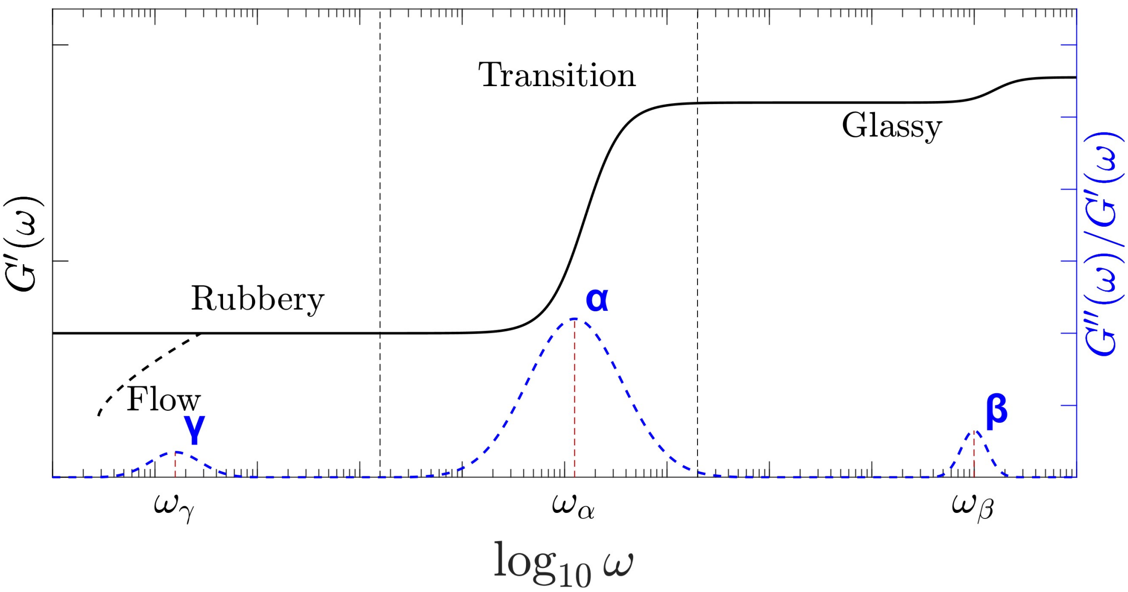

Figure 1.3: The viscoelastic behavior of a polymer is characterized by the storage modulus $\mathcal{G}'(\omega) = \mathrm{Re}(\mathcal{G}^*(\omega))$ and the loss tangent $\tan\delta(\omega) = \mathcal{G}''(\omega)/\mathcal{G}'(\omega)$, both presented as functions of logarithmic frequency or temperature. The curves illustrate the glassy, transition, and rubbery regions, along with the relaxation processes α, β, and γ, including the glass transition (θ_g). Vertical dashed lines indicate θ_α, θ_β, and θ_γ, while the extension at low frequency shows the viscous flow regime.

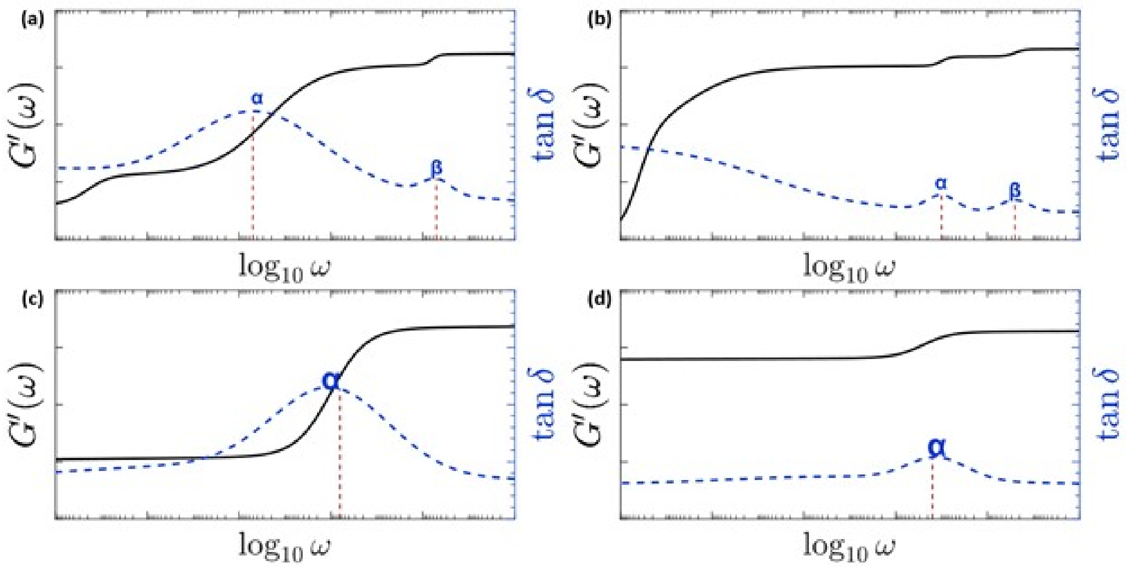

Figure 1.4: Schematic representation of $\mathcal{G}'(\omega)$ (black solid line) and $\tan\delta$ (blue dashed line) as functions of frequency for different polymer classes: (a) amorphous thermoplastics (linear or branched), (b) semi-crystalline thermoplastics (linear or branched), (c) elastomers (sparsely cross-linked), and (d) thermosets (densely cross-linked).

multiple relaxation mechanisms preclude a single shift function [99]. At high temperature, expansion increases mobility and lowers the modulus; entanglement then dominates, with the equilibrium modulus set by crosslink density and molecular mass, while uncrosslinked chains slide freely and the material behaves as a liquid [76].

Defining θ_g from free volume alone is difficult, since Kovács [100] showed it to be time-dependent. The loss tangent offers an alternative: although it may show several peaks, the main one typically coincides with the frequency at which the storage modulus changes most rapidly [76]. The locus of these maxima, $\theta_g = f(\omega)$, indicates whether the material is glassy or rubbery at a given frequency. Composition also tunes θ_g: plasticizers lower it by increasing chain mobility, while particulate fillers raise it by restricting interfacial free volume [101].

The transition can equally be tracked through volume: in a strain-free sample, the specific volume–temperature curve shows a slope change near θ_g. By the free-volume concept [102], the material is stiff below θ_g, where free volume is limited [103], and softer above it, where greater free volume enhances chain mobility [104]—a link that ties macroscopic mechanical behavior directly to molecular structure.

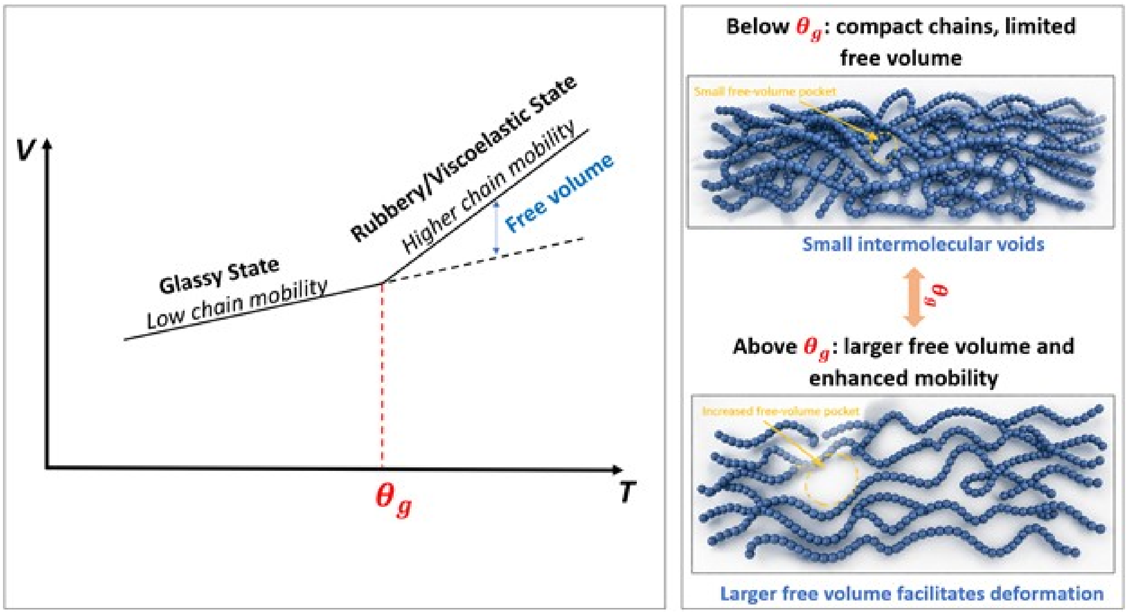

Figure 1.5: The glass transition is shown from volumetric and molecular perspectives. On the left, the specific volume–temperature curve changes slope at θ_g, separating the low-mobility glassy state from the high-mobility rubbery state; the dashed line extrapolates the glassy region, while the open line marks the free-volume increase above θ_g. On the right, the molecular picture shows densely packed chains below θ_g and enhanced mobility above it, driven by increased free volume.

Thermorheologically simple materials, as described by [105, 106, 107], form an important class. For these materials, temperature affects only the position of the relaxation function along the time axis, not its shape. If $\mathcal{G}(t)$ is the relaxation function at the base temperature θ_0 and $\mathcal{G}(t, \theta)$ is the relaxation function at another temperature, then the thermorheological simplicity is expressed as:

$$\mathcal{G}(t, \theta) = \mathcal{L}(\log_{10} t + \phi_\theta(\theta)) \,, \tag{1.26}$$

where $\phi_\theta(\theta)$ denotes the shift function, which satisfies the conditions $\phi_\theta(\theta_0) = 0$, $d\phi_\theta(\theta)/d\theta > 0$. These properties indicate that the relaxation curve shifts along the logarithmic time axis as the temperature changes, and is the basis of the time–temperature superposition principle.

If one introduces $\phi_\theta(\theta) = \log_{10} a_\theta(\theta)$, then $a_\theta(\theta_0) = 1$, and Equation (1.26) can be rewritten as $\mathcal{G}(t, \theta) = \mathcal{L}(\log_{10}(t\, a_\theta(\theta)))$. It follows that $\mathcal{G}(t, \theta) = \mathcal{G}(\varpi)$, where $\varpi = t, a_\theta(\theta)$.

This shows that the relaxation function at temperature θ follows from that at θ_0 by replacing t with the reduced time ϖ, or more generally $\mathcal{G}(t, \theta) = b_\theta(\theta)\, \mathcal{G}(\varpi)$, with $b_\theta(\theta) = \rho\, \theta/(\rho_0\, \theta_0)$ accounting for the minor vertical shift from density and temperature changes—small enough to be neglected in most contact-mechanics applications, where the horizontal shift $a_\theta(\theta)$ dominates.

The same principle applies in the frequency domain: the complex modulus (and likewise the creep function) at temperature θ follows from that at θ_0 by substituting ω with $\omega/a_\theta(\theta)$. This underlies the master curves obtained from dynamic mechanical analysis (DMA) and used in numerical contact models; the indentation and oscillatory contact analyses in this dissertation rely on such temperature-shifted viscoelastic functions to characterize dynamic response and energy dissipation.

1.3 Constitutive Rheological Models for Materials

Linear viscoelastic constitutive behavior is commonly represented through rheological models combining idealized elastic and viscous elements, which phenomenologically capture the interplay of instantaneous elastic deformation and time-dependent molecular rearrangement underlying polymer response. The following section examines the Maxwell, standard linear solid, and generalized Maxwell models, along with their time- and frequency-domain responses and physical implications.

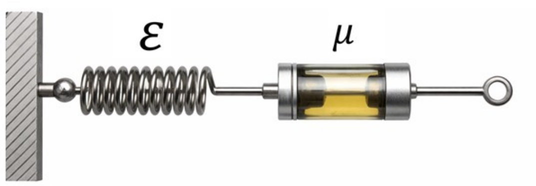

Figure 1.6: Schematic representation of the Maxwell viscoelastic model.

The Maxwell model consists of an elastic spring and a viscous damper (dashpot) connected in series, as shown in Figure 1.6. In this arrangement, the stress in both elements is the same, and the total strain is defined as the sum of the strains developed in the spring and in the dashpot. Accordingly, the constitutive relations are written as:

$$\sigma(t) = \mathcal{E}\,\varepsilon_s(t) \qquad \Rightarrow \qquad \dot{\varepsilon}_s(t) = \frac{\dot{\sigma}(t)}{\mathcal{E}}, \tag{1.27}$$

and

$$\sigma(t) = \mu\,(\dot{\varepsilon}_d(t) - \dot{\varepsilon}_s(t)) = \mu\,\dot{\varepsilon}_d(t) - \frac{\mu}{\mathcal{E}}\,\dot{\sigma}(t). \tag{1.28}$$

Combining the above expressions leads to the governing differential equation

$$\sigma(t) + \frac{\mu}{\mathcal{E}}\,\dot{\sigma}(t) = \mu\,\dot{\varepsilon}_d(t). \tag{1.29}$$

Equivalently, introducing the characteristic relaxation time $\tau = \mu/\mathcal{E}$, the constitutive law can be rewritten in the more compact form

$$\dot{\sigma}(t) + \frac{1}{\tau}\,\sigma(t) = \mathcal{E}\,\dot{\varepsilon}(t). \tag{1.30}$$

This relationship indicates that stress is a function of both the current strain and its rate of change, which constitutes a fundamental characteristic of viscoelastic behavior [76, 78, 82, 108].

Stepwise deformation can be applied to determine the relaxation function. In this context, the stress response corresponds to the relaxation modulus $\mathcal{G}(t)$. Substituting this relationship into the previous equation produces the following result:

$$\frac{d\mathcal{G}(t)}{dt} + \frac{1}{\tau}\mathcal{G}(t) = \mathcal{E}\,\delta(t). \tag{1.31}$$

To determine the initial condition, both sides of the equation are integrated in the interval $t \in [0^-,0^+]$:

$$\int_{0^-}^{0^+} \frac{d\mathcal{G}(t)}{dt}\,dt + \frac{1}{\tau}\int_{0^-}^{0^+} \mathcal{G}(t)\,dt = \mathcal{E}\int_{0^-}^{0^+} \delta(t)\,dt. \tag{1.32}$$

Since the integration interval is infinitesimal, the second term on the left-hand side may be neglected, and one obtains, $\mathcal{G}(0^+) - \mathcal{G}(0^-) = \mathcal{E}$. Recalling causality, $\mathcal{G}(0^-) = 0$, and therefore $\mathcal{G}(0^+) = \mathcal{E}$. This result also has a clear physical interpretation. Upon application of the deformation step, the shock absorber (dashpot) does not deform instantaneously and thus acts as a rigid element [78, 106, 76]. Consequently, the system initially behaves as a purely elastic solid with stiffness $\mathcal{E}$. For

$t > 0$, the Dirac delta vanishes and the governing equation reduces to the homogeneous form [108], $\tau\,\dot{\mathcal{G}}(t) + \mathcal{G}(t) = 0$, considering the initial condition, $\mathcal{G}(0^+) = \mathcal{E}$, the relaxation function is found as

$$\mathcal{G}(t) = \mathcal{E}\,\mathcal{H}(t)\,\mathrm{e}^{-t/\tau}. \tag{1.33}$$

The exponential decay of $\mathcal{G}(t)$ shows that the Maxwell model progressively relaxes the applied stress until the relaxation modulus vanishes at long times. This is an important feature of the model: because $\mathcal{G}(t) \to 0$ as $t \to \infty$, the Maxwell element ultimately behaves as a viscoelastic fluid rather than as a solid. the elastic spring governs the initial response, whereas at sufficiently long times the dashpot dominates and permits continuous deformation.

The response of the Maxwell model to a step stress effect can be determined by considering that the total strain in two elements connected in series is expressed as $\varepsilon(t) = \varepsilon_s(t) + \varepsilon_d(t)$. For a unit step stress, the corresponding creep function becomes

$$\mathcal{J}(t) = \frac{1}{\mathcal{E}}\,\mathcal{H}(t) + \frac{t}{\mu}\,\mathcal{H}(t). \tag{1.34}$$

This result predicts a linear increase of strain with time. Although such behavior captures the possibility of long-term viscous flow, it is not able to represent the initial nonlinear shape typically observed in experimental primary creep curves. For this reason, the Maxwell model is useful as a basic theoretical model, but it is generally insufficient for a realistic description of the creep response of many polymers.

The harmonic response of the Maxwell model is examined in the frequency domain using a complex modulus. For elements connected in series, the equivalent complex modulus adheres to the following condition:

$$[\mathcal{G}^*(\omega)]^{-1} = \sum_i \left[\mathcal{G}_i^*(\omega)\right]^{-1}. \tag{1.35}$$

For the Maxwell model, this gives

$$\mathcal{G}^*(\omega) = \mathcal{E}\,\frac{i\,\omega\,\mu}{\mathcal{E} + i\,\omega\,\mu} = \mathcal{E}\,\frac{i\,\omega\,\tau}{1 + i\,\omega\,\tau} = \frac{\mathcal{E}\,\omega^2\tau^2}{1+\omega^2\tau^2} + i\,\frac{\mathcal{E}\,\omega\,\tau}{1+\omega^2\tau^2}. \tag{1.36}$$

The real part of the complex modulus corresponds to the elastic (storage) component, while the imaginary part reflects energy dissipation. At very low frequencies, the storage modulus approaches zero, and the material exhibits liquid-like behavior.At very high frequencies, the material transitions to a glassy state and behaves as an elastic solid. Between these two extremes, the imaginary part reaches its maximum, indicating the frequency range where viscoelastic energy losses are most pronounced.

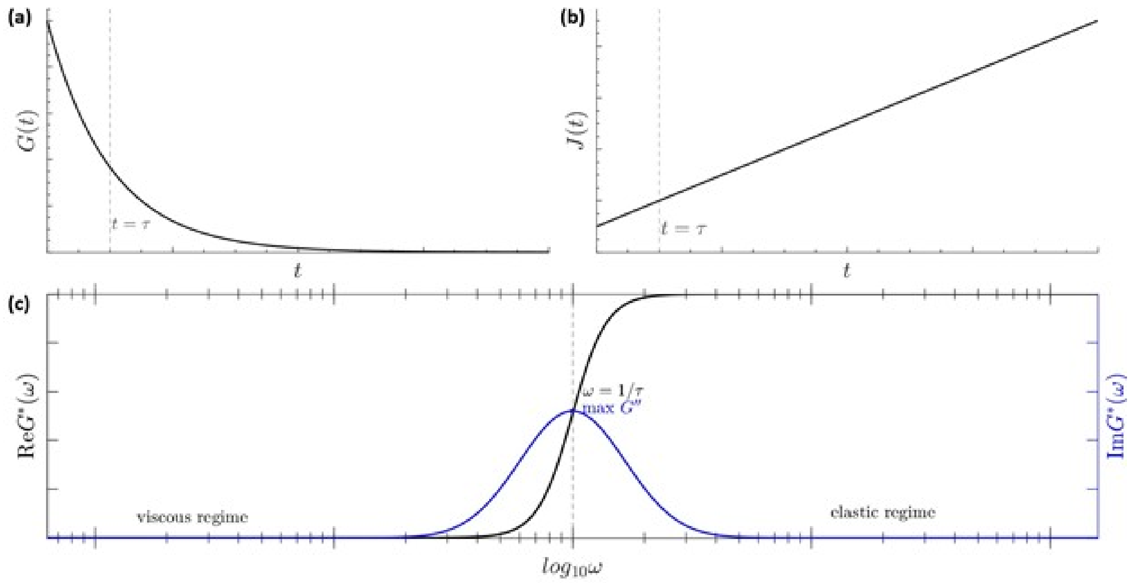

Figure 1.7: Relaxation modulus and creep compliance of the Maxwell model, together with the frequency-domain representation of its complex modulus. (a) Relaxation modulus, $\mathcal{G}(t) = \mathcal{E}\ \exp(-t/\tau)$, as a function of time. (b) Creep compliance, $\mathcal{J}(t) = 1/\mathcal{E} + t/\mu$, as a function of time. (c) Real part of the complex modulus, $\mathrm{Re}(\mathcal{G}^*(\omega)) = \mathcal{G}'(\omega)$ (black line, left axis), and imaginary part, $\mathrm{Im}(\mathcal{G}^*(\omega)) = \mathcal{G}''(\omega)$ (blue line, right axis), plotted as functions of angular frequency ω. The dashed vertical line denotes the characteristic frequency $\omega = 1/\tau$.

To more accurately model the behavior of many viscoelastic solids, an additional elastic spring is incorporated in parallel with the Maxwell element. This configuration forms the Standard Linear Solid model, which is depicted schematically in Figure 1.8. Because of the parallel arrangement, the total stress equals the sum of the stresses in both branches, while the strain remains identical in each branch.

The corresponding relaxation modulus can be written as

$$\mathcal{G}(t) = \mathcal{H}(t)\left(\mathcal{E}_0 + \mathcal{E}_1\ \exp(-t/\tau)\right). \tag{1.37}$$

This expression immediately shows that the relaxation function decreases with time, but, unlike the Maxwell model, it does not vanish at long times. In fact, $\lim_{t\to\infty}\mathcal{G}(t) = \mathcal{E}_0, \qquad \lim_{t\to 0}\mathcal{G}(t) = \mathcal{E}_0 + \mathcal{E}_1 = \mathcal{E}_\infty.$

Over extended periods, the response is governed exclusively by the spring with stiffness $\mathcal{E}_0$, resulting in the system exhibiting the characteristics of a solid with finite equilibrium stiffness. At the onset of loading, the shock absorber functions as a rigid element, causing the system to respond as a stiffer elastic solid characterized by modulus $\mathcal{E}_\infty$.

The creep function of the standard linear solid is obtained by considering a step stress input. In this case, the governing differential equation can be written as

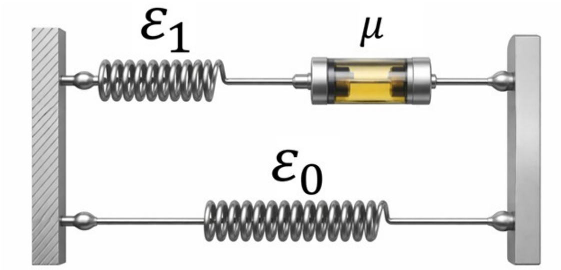

Figure 1.8: Schematic representation of the standard linear solid model.

$$\frac{d\mathcal{J}(t)}{dt} + \frac{1}{\beta\,\tau}\,\mathcal{J}(t) = \frac{1}{\mathcal{E}_\infty}\left(\delta(t) + \tau^{-1}\mathcal{H}(t)\right), \tag{1.38}$$

where $\beta = \mathcal{E}_\infty/\mathcal{E}_0$. To solve this equation, it is convenient to first identify the particular solution associated with the long-time equilibrium state. Since, for $t \to \infty$, the derivative of the creep function vanishes, one obtains $\mathcal{J}_\infty/(\beta\,\tau) = 1/(\mathcal{E}_\infty\,\tau)$,

from which $\mathcal{J}_p = \mathcal{J}_\infty = \beta/\mathcal{E}_\infty = 1/\mathcal{E}_0$. The initial condition is obtained by integrating the governing equation over the interval $t \in [0^-, 0^+]$ [108]:

$$\int_{0^-}^{0^+} \frac{d\mathcal{J}(t)}{dt}\,dt + \frac{1}{\beta\,\tau}\int_{0^-}^{0^+} \mathcal{J}(t)\,dt = \frac{1}{\tau\,\mathcal{E}_\infty}\int_{0^-}^{0^+} \mathcal{H}(t)\,dt + \frac{1}{\mathcal{E}_\infty}\int_{0^-}^{0^+} \delta(t)\,dt. \tag{1.39}$$

Again, because the interval is infinitesimal, the integral involving $\mathcal{J}(t)$ can be neglected, and, invoking causality, one finds $\mathcal{J}(0^+) = 1/\mathcal{E}_\infty$. The homogeneous equation associated with the problem is $\beta\,\tau\,\dot{\mathcal{J}}(t) + \mathcal{J}(t) = 0$, whose solution, together with the previously derived particular solution and the initial condition, leads to [108]

$$\mathcal{J}(t) = \frac{\mathcal{H}(t)}{\mathcal{E}_0} + \mathcal{H}(t)\left(\frac{1}{\mathcal{E}_\infty} - \frac{1}{\mathcal{E}_0}\right) \mathrm{e}^{-t/(\beta\tau)}. \tag{1.40}$$

This expression shows that the creep response is limited and gets closer to the steady-state compliance $1/\mathcal{E}_0$ over time. So, unlike the Maxwell model, the standard linear solid model shows both the delayed deformation and the limited long-term stiffness.

Under harmonic loading, the complex modulus of the standard linear solid model is determined by the summation rule of parallel elements [108], $\mathcal{G}^*(\omega) = \sum_i \mathcal{G}_i^*(\omega)$.

The limiting values are particularly instructive. At very low frequencies, $\lim_{\omega\to 0}\mathcal{G}^*(\omega) = \mathcal{E}_0$, whereas at very high frequencies, $\lim_{\omega\to\infty}\mathcal{G}^*(\omega) = \mathcal{E}_0 + \mathcal{E}_1$,

Thus, the model exhibits elastic solid behavior at both low and high frequencies, resulting in minimal dissipation. At intermediate frequencies, the imaginary component increases and energy losses reach a maximum. In this frequency range, viscoelastic effects are most pronounced.

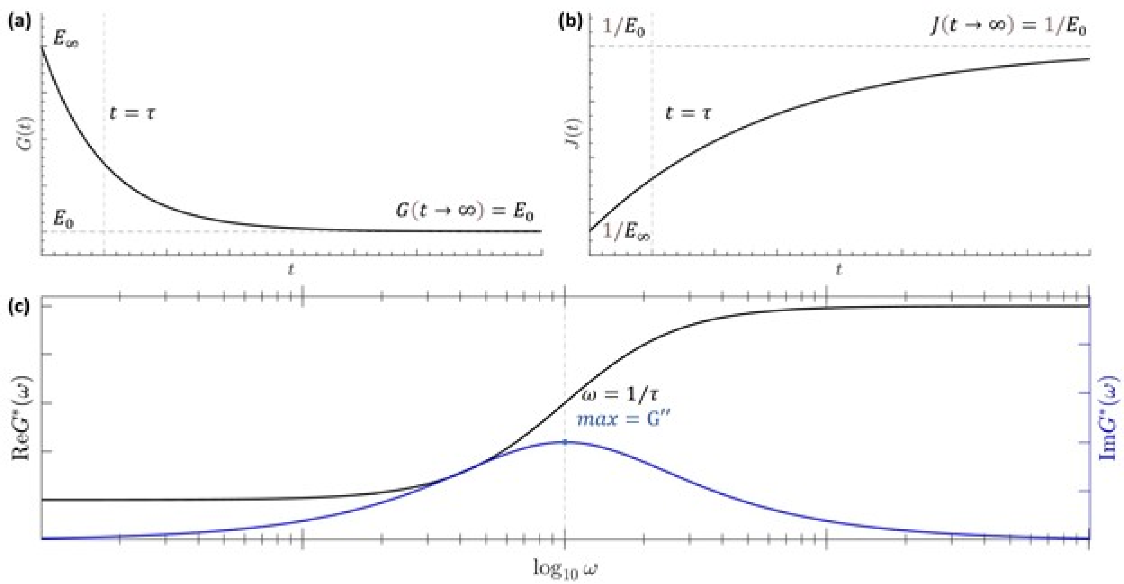

Figure 1.9: Standard linear solid (Zener) model. (a) Relaxation function $\mathcal{G}(t)$ as a function of time, showing a decay from the instantaneous modulus to a finite equilibrium value. (b) Creep function $\mathcal{J}(t)$ as a function of time, illustrating a bounded increase in compliance. (c) Real part of the complex modulus, $\mathrm{Re}(\mathcal{G}^*(\omega))$ (black line, left axis), and imaginary part, $\mathrm{Im}(\mathcal{G}^*(\omega))$ (blue line, right axis), plotted as functions of angular frequency ω on a logarithmic scale. The curves highlight the transition between low- and high-frequency elastic regimes and the intermediate viscoelastic response.

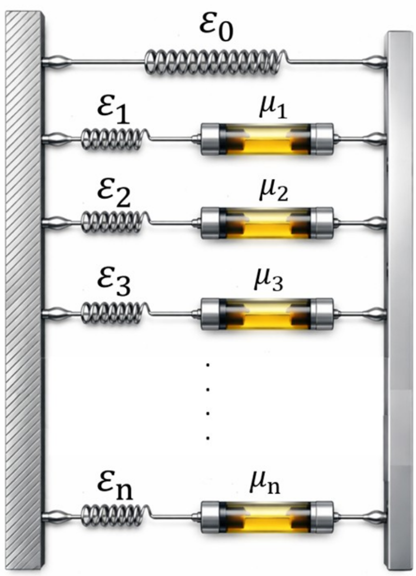

Figure 1.10: Schematic representation of the generalized Maxwell model.

Maxwell and standard linear solid models are useful but account for only a single relaxation time. In contrast, real polymers exhibit a broad relaxation spectrum, so single-time models often represent transitions too abruptly. To overcome this problem, the generalized Maxwell (Wiechert) model is used, Figure 1.10. This model consists of a parallel combination of several Maxwell branches, each characterized by a different relaxation time. As a result, the behavior of real materials is described more accurately.

The relaxation function then becomes

$$\mathcal{G}(t) = \mathcal{E}_0\, \mathcal{H}(t) + \sum_{j=1}^{n} \mathcal{E}_j\, \mathrm{e}^{-t/\tau_j}\, \mathcal{H}(t). \tag{1.41}$$

while the corresponding complex modulus is [108]

$$\mathcal{G}^*(\omega) = \mathcal{E}_0 + \sum_{j=1}^{n} \frac{i\,\omega\,\tau_j\,\mathcal{E}_j}{1 + i\,\omega\,\tau_j}. \tag{1.42}$$

This formulation extends single-relaxation time models to account for multiple relaxation mechanisms simultaneously. It effectively fits experimental relaxation and dynamic modulus data across broad time and frequency ranges. As a result, the generalized Maxwell model is widely used to describe linear viscoelastic materials.

Chapter 2

Dynamic Response of Viscoelastic Solids

The primary objective of this chapter is to establish and validate a high-precision, multi-method framework for analyzing viscoelastic solids under oscillatory microindentation conditions. Although advanced numerical models, such as the Boundary Element Method (BEM), can predict the complex time-dependent behavior of viscoelastic contacts, these models frequently lack adequate experimental validation for specific modeling conditions [39, 37].This chapter addresses this deficiency by combining high-precision experiments, advanced numerical simulations, and a novel analytical formulation approach into a single validation framework. The goal is to show that such an integrated approach is not only possible but also necessary for the quantitatively reliable prediction of key behaviors such as energy dissipation due to hysteresis and the onset of contact separation. This approach provides a powerful and practical tool for a wide range of applications, from the design of viscoelastic dampers to the precise mechanical characterization of biomaterials.

Therefore, in the next section, special attention is paid to the integration of experimental tests with numerical and theoretical approaches, substantiating the models with empirical data. The experimental program accurately reproduces the boundary conditions used in numerical simulations. The primary focus is the micro-indentation regime under harmonic loading, which is well suited for thin biological coatings and sensitive materials. A well-characterized nitrile-butadiene rubber (NBR) was chosen, which exhibits linear viscoelastic behavior, and the tests were carried out with a specially designed periodic indenter within a high-precision mechanical system. The obtained results, in particular the hysteresis force–displacement cycles serve as a key criterion for evaluating the predictive accuracy of the Boundary Element Method (BEM) model, which directly simulates the effect of a rigid, periodic indenter on a viscoelastic half-space. A simplified analytical formulation is also presented to estimate dissipated work and clarify the main influencing parameters. The chapter describes the experimental and numerical methods, compares the results of the three approaches, and evaluates the effectiveness of this integrated framework in explaining and predicting viscoelastic contact behavior.

2.1 Materials and Experimental Methods

Nitrile-butadiene rubber (NBR) was selected for this study because of its chemical resistance and stable mechanical properties [109, 110]. NBR is well studied and exhibits predominantly linear viscoelastic behavior at moderate strain levels, which reduces nonlinearity and facilitates more accurate evaluation of theoretical models. Its widespread application in industry, such as in gaskets, sealing, and vibration damping, further supports its suitability for this research [111].

To characterize its time-dependent mechanical properties, we conducted an extensive Dynamic Mechanical Analysis (DMA). DMA separates the elastic (energy-storing) and viscous (energy-dissipating) components by applying sinusoidal deformation and measuring the phase-differential stress response. The dimensions of the NBR sample used were 4 cm in length, 5 mm in width, and 5 mm in thickness. The tests were performed with a tensile fixture (Solid Rectangular Fixture, SRF), see Figure 2.1 a and this setup is suitable for film and elastomer samples. The experimental program included a constant-frequency temperature sweep and a constant-temperature multi-frequency sweep. Temperature sweeps enabled precise identification of the glass transition by a sharp decrease in storage modulus ($\mathcal{E}'$) and a peak in the loss factor ($\tan\delta$).

Multi-frequency isotherms from a selected temperature range were analyzed using the time–temperature superposition (TTS) principle to construct master curves for the storage modulus $\mathrm{Re}(\mathcal{E}(\omega))$ and loss modulus $\mathrm{Im}(\mathcal{E}(\omega))$. This method allows the generation of a single and continuous curve by horizontally shifting the data collected at different temperatures, thus extending the frequency range by several decades. The resulting master curve fully characterizes the material's viscoelastic properties and serves as the primary empirical basis for subsequent numerical simulations.

All indentation tests were conducted using the Biomomentum MACH-1 v. 4.5 (Biomomentum Inc., Canada), (see Figure 2.2 a), universal mechanical testing system, recognized for its high accuracy and flexibility in evaluating soft materials [111, 112]. This lightweight, multi-axis system is designed to measure the mechanical properties of a wide range of materials, such as polymers, gels, and biological tissues. The system accommodates samples ranging from tens of microns to several centimeters, making it highly suitable for both laboratory and biomechanical applications [113, 114, 115, 116].

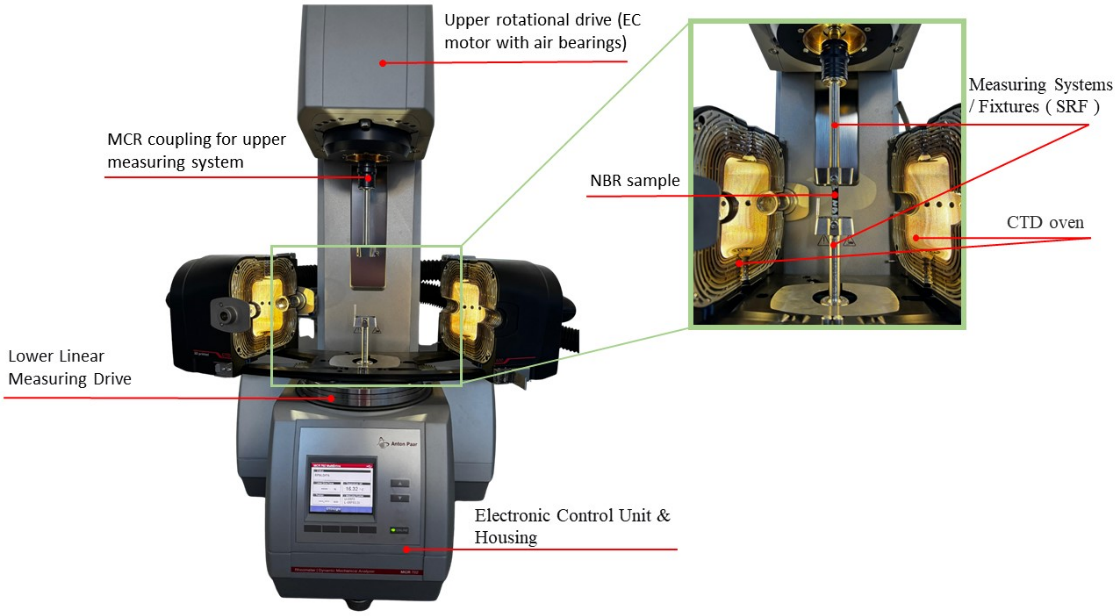

Figure 2.1: Schematic overview of the Anton Paar MCR 702e MultiDrive dynamic mechanical analyzer (DMA), highlighting its dual-drive system for rotational shear and linear DMA testing modes (tension, compression, bending).

The main advantage of this system is its highly accurate and repeatable displacement-controlled motion, enabling precise measurement of stiffness, viscoelasticity, plasticity, and relaxation. In this study, ithe system was equipped with a high-sensitivity multi-axis load cell that measures forces and moments along the x, γ, and z, axes simultaneously. This load cell has a maximum load capacity of $\pm 250\,\mathrm{N}$ along the z axis and $\pm 125\,\mathrm{N}$ N along the x and γ axes, and provides a force resolution as high as $12.5\,\mathrm{mN}$. This sensitivity was crucial for the reliable measurement of very small forces generated in micrometer-scale indentation tests. As a result, the high accuracy of the device ensures that experimental data can be used as a reliable basis for the validation of numerical models.

A key objective of this study was to design a rigid indenter for direct comparison with periodic boundary conditions in the numerical model. The indenter features a periodic structure with three cylindrical tips, simplifying the complex three-dimensional contact problem to a one-dimensional formulation.

The indenter has a rectangular base measuring $20\,\mathrm{mm}$ in width and $6\,\mathrm{mm}$ in depthç see Figure 2.2 (b). Each cylindrical tip has a radius of $R = 2\,\mathrm{mm}$ mm and is spaced $\lambda = 8\,\mathrm{mm}$ mm apart. The indenter includes a 1/4–28 male thread for mounting on a load cell.

The indenter is constructed from stainless steel 303, which offers high strength and corrosion resistance. It was manufactured using CNC machining to ensure high geometric accuracy. The contact surface was polished to minimize roughness and

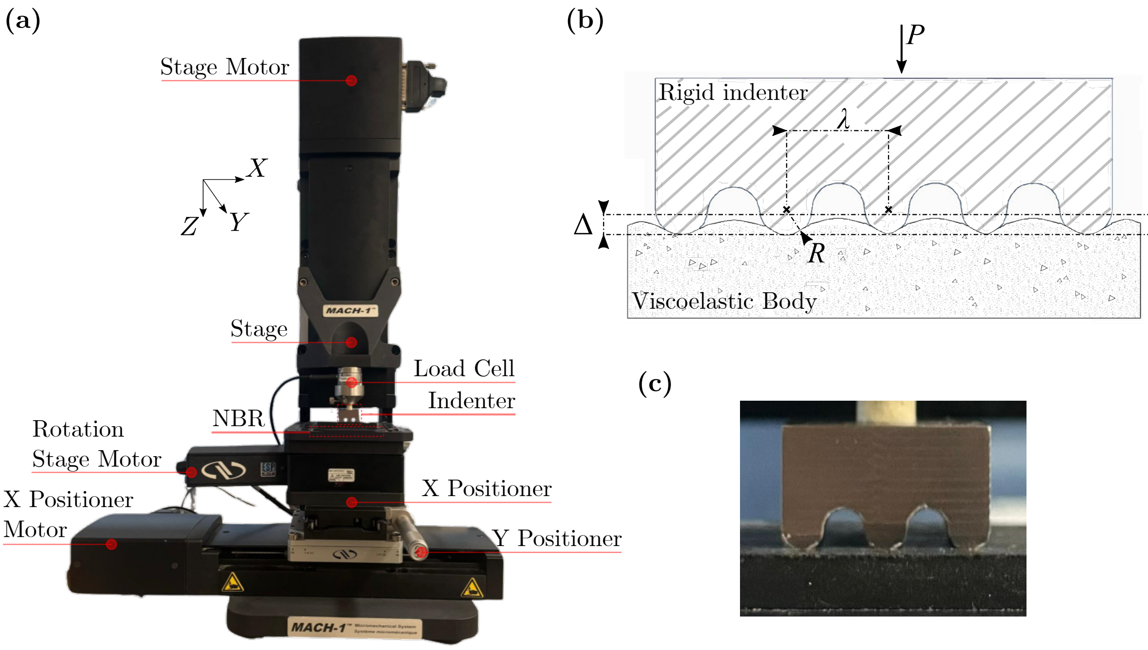

Figure 2.2: Experimental setup for static and dynamic testing of NBR samples. (a) Biomomentum-MACH1 machine setup, (b) schematic illustration of the indentation-sample interface, and (c) illustration of the indentation design placed on the NBR sample under real conditions.

closely match the ideal smooth surface conditions assumed in theoretical models.

The experimental test protocol consisted of two main stages to study the time-dependent response of the material: stress relaxation and harmonic indentation. The tests were performed by applying a precisely defined displacement history $\Delta(t)$ to the indenter.

The protocol began with a *stress relaxation phase*. The indenter was inserted into the NBR sample to an average indentation depth $\tilde{\Delta}_0 = \Delta_0/R = 0.05$ (where R is the punch radius) and held for 600 seconds. This allowed the material to relax and reach equilibrium, ensuring stable initial conditions for the dynamic tests.

Subsequently, the protocol proceeded to the *harmonic test*. During this phase, the indenter moved with a sinusoidal oscillation superimposed on the average indentation, following the law described below:

$$\Delta(t) = \Delta_0 + \Delta_1(t) = \Delta_0 + \alpha \sin(\omega t)\, \mathcal{H}(t - t_0), \tag{2.1}$$

where α is the oscillation amplitude, $\omega = 2\pi f$ is the angular frequency, the function $\mathcal{H}(t)$ denotes the Heaviside step function, which activates the oscillatory response only after the initial relaxation phase. The amplitude was set to $\tilde{\alpha} = \alpha/R = 0.005$ for the primary tests, and the frequency was varied across a range of values.

The harmonic tests employed a multi-axis load cell to precisely measure the small forces produced during micrometer-scale oscillations. This two-step protocol characterizes both long-term relaxation behavior and dynamic cyclic response.

2.2 Theoretical and Numerical Framework

This section establishes the mathematical foundation for Chapter 2 and introduces a framework for modeling time-dependent contact mechanics in viscoelastic solids. The exposition commences with the constitutive laws of viscoelasticity, followed by the development and application of the Boundary Element Method (BEM), which enables simulation of arbitrary loading histories and is further extended to incorporate thin viscoelastic layers.

Viscoelastic materials, such as nitrile-butadiene rubber (NBR), exhibit a time-dependent response in contrast to pure elastic solids. The deformation of these materials depends on the complete loading history and is characterized by hereditary behavior [35, 82, 117]. The fundamental constitutive relation for an isotropic, linear viscoelastic solid is expressed as follows:

$$\varepsilon(t) = \int_{-\infty}^{t} \frac{d\sigma(\tau)}{d\tau}\, \mathcal{J}(t-\tau)\, d\tau. \tag{2.2}$$

where $\varepsilon(t)$ is the strain, $\sigma(t)$ the stress, and $\mathcal{J}(t)$ the *creep compliance function*. Physically, $\mathcal{J}(t)$ represents the strain response to a unit step of stress [35]. It satisfies causality ($\mathcal{J}(t<0)=0$), enforced mathematically through the Heaviside step function $\mathcal{H}(t)$.

The creep function can be expressed as

$$\mathcal{J}(t) = \frac{\mathcal{H}(t)}{\mathcal{E}_0} - \mathcal{H}(t) \int_{0}^{\infty} \mathcal{C}(\xi)\, \mathrm{e}^{-t/\xi}\, d\xi. \tag{2.3}$$

here $\mathcal{E}_0$ is the *rubber modulus* characterizing very low frequencies, and $C(\tau)$ is the creep spectrum corresponding to the relaxation time. Although real materials possess a continuous relaxation spectrum, practical calculations require discretization of this spectrum using the *Prony series*:

$$\mathcal{C}(\tau) = \sum_{i=1}^{n} \mathcal{C}_i\, \delta(\tau - \tau_i), \tag{2.4}$$

leading to a numerically convenient form of the creep function:

$$\mathcal{J}(t) = \frac{\mathcal{H}(t)}{\mathcal{E}_0} - \mathcal{H}(t) \sum_{i=1}^{n} \mathcal{C}_i\, \mathrm{e}^{-t/\tau_i}. \tag{2.5}$$

In this context, C_i represent the creep coefficients, which are the weights of each relaxation mode, while τ_i denote the discrete relaxation times corresponding to specific molecular processes.

For oscillatory loading, analysis in the frequency domain is often preferred. In this context, the primary characteristic quantity is the *complex modulus*:

$$\mathcal{E}^*(\omega) = \frac{\sigma(\omega)}{\varepsilon(\omega)} = \left(i\,\omega\,\mathcal{J}(\omega)\right)^{-1}. \tag{2.6}$$

This is conventionally written as $\mathcal{E}^*(\omega) = \mathcal{E}'(\omega) + i\,\mathcal{E}''(\omega)$, here $\mathcal{E}'(\omega)$ — the *storage modulus* — represents the in-phase elastic response and quantifies the energy stored and released during each cycle. In contrast, the *loss modulus*, $\mathcal{E}''(\omega)$, characterizes the out-of-phase viscous response and the energy dissipated as heat.

In practice, the Prony parameters $\{C_i, \tau_i\}$, are typically determined by fitting to results from Dynamic Mechanical Analysis (DMA). To achieve a broad frequency range, the *Time–Temperature Superposition (TTS)* principle is applied. In this approach, curves measured at different temperatures are horizontally shifted to construct a single master curve [37, 39, 39, 38].

We now consider the contact problem under investigation (see Figure 2.2 (b)), in which a rigid indenter interacts with a viscoelastic layer of infinite thickness. According to Equation ((2.2)), the normal displacement of the surface, $u(\mathbf{r}, t)$, is given by the following integral relation in terms of the time derivative of the applied stress, $\dot{\sigma}(\mathbf{r}, t)$ [37, 118, 39, 37, 38]:

$$u(\mathbf{r}, t) = \int_{-\infty}^{t} d\tau \int d^2r'\, \frac{\partial \sigma(\mathbf{r}', \tau)}{\partial \tau}\, \mathcal{G}_{\mathrm{tot}}(\mathbf{r} - \mathbf{r}',\, t - \tau). \tag{2.7}$$

For linear viscoelastic materials, the kernel separates into temporal and spatial components [39, 37], yielding:

$$u(\mathbf{r}, t) = \int_{-\infty}^{t} d\tau \int d^2r'\, \mathcal{J}(t - \tau)\, \mathcal{G}(\mathbf{r} - \mathbf{r}')\, \frac{\partial \sigma(\mathbf{r}', \tau)}{\partial \tau}. \tag{2.8}$$

Here, $\mathcal{J}(t)$ denotes the creep function, and $\mathcal{G}(\mathbf{r})$ represents the elastic Green's function, which characterizes the displacement of the half-space subjected to a uniform point load.

As shown in Figure 2.2 (b), the system exhibits spatial periodicity with wavelength λ. Consequently, a periodic Green's function $\mathcal{G}_\lambda(\mathbf{r})$ is introduced to characterize the displacement arising from the periodic pressure distribution.

Specifically, the pressure distribution $\chi_\lambda(x)$ is analyzed. This distribution is generated by periodically repeating a uniform load $\chi_a(x)$ applied over a region of length a with period λ:

$$\chi_\lambda(\mathbf{r}) = \sum_{k=-\infty}^{\infty} \chi_a(\mathbf{r} - k\lambda), \tag{2.9}$$

where $\chi_a(\mathbf{r})$ remains constant within the charged field and is zero outside this region. Upon transformation to the Fourier domain, the periodic Green's function is expressed as $\mathcal{G}_\lambda(q) = \mathcal{G}(q)\,\chi_\lambda(q)$, where $\chi_\lambda(q)$ is the Fourier transform of the periodic pressure distribution:

$$\chi_\lambda(q) = \int_{-\infty}^{\infty} \chi_\lambda(\mathbf{r})\,\mathrm{e}^{-iqr}\,dr. \tag{2.10}$$

This evaluates to:

$$\chi_\lambda(q) = \sum_{k=-\infty}^{+\infty} \frac{2\sin\left(\frac{1}{2}kq_0 a\right)}{kq_0}\,\delta(q - kq_0), \tag{2.11}$$

where $q_0 = \frac{2\pi}{\lambda}$ is the fundamental wavevector. Taking the inverse Fourier transform, the periodic Green's function in real space becomes:

$$\mathcal{G}_\lambda(\mathbf{r}) = \frac{q_0}{2\pi} \sum_{k=-\infty}^{\infty} \mathcal{G}(kq_0) \frac{2\sin\left(\frac{kq_0 a}{2}\right)}{kq_0} \mathrm{e}^{ikq_0 r}. \tag{2.12}$$

This expression demonstrates that $\mathcal{G}_\lambda(\mathbf{r})$ can be represented as a Fourier series, enabling efficient computation using the Inverse Fast Fourier Transform (IFFT).

The integral Equation (2.12) is discretized in both space and time, and subsequently solved numerically [37, 119] The spatial domain is partitioned into N elements with period λ, assuming constant stress within each element. Collocation points are located at the element centers x_j. The time domain is divided into steps of size Δt, and the hereditary integral is approximated by summing past stress increments.

Accordingly, the displacement at the i-th element at time $t_n = n\Delta t$ is expressed as:

$$u(x_i, n\Delta t) = \sum_{j=1}^{N} \mathcal{G}_\lambda(x_i - x_j) \sum_{k=0}^{n} \mathcal{J}\big((n-k)\Delta t\big)\,\Delta\sigma_j^k, \tag{2.13}$$

, $\Delta\sigma_j^k = \sigma(x_j, k\Delta t) - \sigma(x_j, (k-1)\Delta t)$. To separate the contribution of the current time step from the history-dependent terms, we introduce:

$$u(x_i, n\Delta t) - \Xi(x_i, n\Delta t) - \Upsilon(x_i, n\Delta t) = \mathcal{J}(0) \sum_{j=1}^{N} \mathcal{G}_\lambda(x_i - x_j)\,\sigma(x_j, n\Delta t). \tag{2.14}$$

where

$$\Xi(x_i, n\Delta t) = \sum_{j=1}^{N} \mathcal{G}_\lambda(x_i - x_j) \sum_{k=0}^{n-1} \mathcal{J}\big((n-k)\Delta t\big)\, \Delta\sigma_j^k, \tag{2.15a}$$

$$\Upsilon(x_i, n\Delta t) = -\mathcal{J}(0) \sum_{j=1}^{N} \mathcal{G}_\lambda(x_i - x_j)\, \sigma(x_j, (n-1)\Delta t), \tag{2.15b}$$

Term Ξ accounts for the accumulated viscoelastic memory effect, while term Υ represents the direct effect from the previous time step. Consequently, Equation (2.14) can be reformulated as a system of linear equations.

Specifically, the displacement at point i is defined as $u_c(x_i, n\Delta t) = u(x_i, n\Delta t) - \Xi(x_i, n\Delta t) - \Upsilon(x_i, n\Delta t)$ and is expressed in terms of the loading at strip j as follows:

$$\{u_{c_i}\} = [\mathcal{K}_{ij}]\{\sigma_j\}, \tag{2.16}$$

where $\mathcal{K}_{ij}$ represents the intercorrelation matrix.

The contact problem is addressed using the numerical approach described by [119]. Because the contact area is not predetermined, an iterative algorithm is employed. At each iteration, elements exhibiting negative pressure are excluded, while interpenetrating elements are incorporated into the contact area.

This formulation does not impose specific kinematic constraints. However, the displacement, denoted as $u_c(x_i, n\Delta t)$, depends on the stress history because the effects of previous time steps are incorporated through the terms $\Xi(x_i, n\Delta t)$ and $\Upsilon(x_i, n\Delta t)$. This dependence increases the complexity of the calculation.

This computational burden is partially alleviated by employing a periodic Green's function, $\mathcal{G}_\lambda$. Consequently, the spatial domain can be restricted to a single period of the rigid indenter [37].

In cyclic contact problems with viscoelastic materials, the mechanical response depends on both elastic deformation and time-dependent viscous processes. Under periodic loading, some energy is stored and recovered elastically, while the remainder is dissipated due to molecular rearrangement, chain mobility, and relaxation.

Macroscopically, this energy loss appears as hysteresis in the force-displacement curve. The area of the hysteresis loop represents the work dissipated during one cycle and characterizes the damping capacity of the system. Therefore, a quantitative assessment of this energy is important for understanding the dynamic behavior of viscoelastic contacts and predicting various engineering applications.

In this section, an analytical expression for the energy dissipated during oscillatory indentation of a viscoelastic half-space is developed based on the Equation (2.1). The analysis is based on the previously presented indentation configuration [37], where a rigid periodic indenter interacts with a flat viscoelastic substrate, see in Figure 2.2. The indentation depth is imposed through a harmonic displacement law consisting of a static indentation component and a superimposed oscillatory perturbation.

From a mechanical point of view, the indentation process consists of two stages. In the first stage, a static indentation Δ_0 is applied and held for a sufficient time to allow the material to relax and approach to equilibrium. During this period, internal stresses redistribute, leading to the formation of a contact area characterized by the contact length a_0 and the equilibrium force $\mathcal{F}_0$. The second stage applies a harmonic displacement $\Delta_1(t)$ to the indenter, generating a time-dependent contact force. The viscoelastic properties of the material induce a phase difference between force and displacement, resulting in hysteresis and energy dissipation in the load–indentation curve.

The analytical description of the contact force, the formulation proposed by Giuseppe Carbone and Maria Mangialardi [120]. This method models the contact between a soft elastic layer and a hard sinusoidal surface, combining the Westergaard solution with a correction derived from the Koiter model.

The present analysis is limited to the symmetric contact case according to Mikayilov [38], and slip and adhesion are not taken into account. Under these assumptions, the contact force between the rigid indenter and the viscoelastic substrate is expressed as follows:

$$\mathcal{F} = \frac{\pi \mathcal{E}^*}{2\,\ln\left(\dfrac{1}{\sin\left(\frac{\pi a}{\lambda}\right)}\right)} \left[\Delta - h\,\left(\sin\left(\frac{\pi a}{\lambda}\right)\right)^2\right] \tag{2.17}$$

where $\mathcal{E}$ and ν denote the Young's modulus and Poisson's ratio of the soft viscoelastic solid. The quantity

$$\mathcal{E}^* = \mathcal{E}\,(1-\nu^2)^{-1} \tag{2.18}$$

represents the effective elastic modulus of the contact system. Here, a denotes the instantaneous contact length, and λ refers to the spatial wavelength associated with the periodic indenter geometry.

The present configuration features an indenter composed of cylindrical tips arranged at regular intervals. When the contact length is much smaller than the spatial wavelength, i.e.

$$a \ll \lambda, \tag{2.19}$$

The cylindrical geometry is represented by an equivalent sinusoidal profile that maintains the same radius of curvature at the contact center. Consequently, the amplitude of this profile is given by:

$$h = \frac{\lambda^2}{4\pi^2 R} \tag{2.20}$$

where R represents the radius of the cylindrical punches.

Because the indentation depth includes both static and oscillatory components, the contact force is expressed as the sum of two distinct parts:

$$\mathcal{F}(t) = \mathcal{F}_0 + \mathcal{F}_1(\Delta_1) \tag{2.21}$$

The first contribution $\mathcal{F}_0$ is the static force from the equilibrium indentation Δ_0 [120]. This force is calculated from Equation (2.17) by replacing the indentation depth with Δ_0. Here, the elastic modulus equals the long-term modulus E_0, describing the material's equilibrium response after relaxation. Thus, the static contact force is written as:

$$\mathcal{F}_0 = \frac{\pi \mathcal{E}_0^*}{2\,\ln\left(\dfrac{1}{\sin\left(\frac{\pi a_0}{\lambda}\right)}\right)} \left[\Delta_0 - h\,\left(\sin\left(\frac{\pi a_0}{\lambda}\right)\right)^2\right] \tag{2.22}$$

where

$$\mathcal{E}_0^* = \mathcal{E}_0\,(1-\nu^2)^{-1} \tag{2.23}$$

and a_0 denotes the static contact length associated with the equilibrium indentation.

The second contribution $\mathcal{F}_1(t)$ arises from the oscillatory indentation component $\Delta_1(t)$. To analyze the dynamic response, it is more convenient to transfer these quantities to the frequency domain by Fourier transformation. The Fourier transform of the oscillatory force is written as:

$$\hat{\mathcal{F}}_1(\omega) = \frac{\pi \mathcal{E}^*(\omega)}{2\,\ln\left(\dfrac{1}{\sin\left(\frac{\pi a_0}{\lambda}\right)}\right)}\,\hat{\Delta}_1(\omega) \tag{2.24}$$

which can be rewritten in a compact form as

$$\hat{\mathcal{F}}_1(\omega) = \hat{\kappa}(\omega)\,\hat{\Delta}_1(\omega) \tag{2.25}$$

Here, $\hat{\kappa}(\omega)$ represents the complex dynamic contact stiffness, while $\mathcal{E}(\omega)$ represents the complex viscoelastic modulus of the material.

The dissipated work over a single oscillation period is calculated from the average power exchanged between the oscillatory force and the indentation velocity. The instantaneous power during indentation is given by:

$$\mathcal{F}_1(t)\,\dot{\Delta}_1(t) \tag{2.26}$$

and the average power over one oscillation cycle is therefore

$$\overline{\Pi} = \frac{\omega}{2\pi} \int_{t}^{t+\frac{2\pi}{\omega}} \mathcal{F}_1(t)\, \frac{d\Delta_1(t)}{dt}\, dt \tag{2.27}$$

Parseval's theorem allows the average power can be expressed in terms of the cross-power spectral density between the oscillatory force and the indentation velocity, as shown below [121, 122]:

$$\bar{\Pi} = \int_{-\infty}^{+\infty} \mathrm{Re}[S_{\mathcal{F}_1\dot{\Delta}_1}(\nu)] d\nu \tag{2.28}$$

The cross-power spectral density appearing in the previous expression can be reformulated using Eq. (2.25) as

$$S_{\mathcal{F}_1\dot{\Delta}_1}(\nu) = \lim_{T\to\infty} \frac{1}{T}\, E\Big[\hat{\kappa}(\nu)\, \hat{\Delta}_1(\nu)\, \Big(i\nu\, \hat{\Delta}_1(\nu)\Big)^*\Big] = -i\nu\, \hat{\kappa}(\nu)\, S_{\Delta_1}(\nu). \tag{2.29}$$

where $S_{\Delta_1}(\nu)$ denotes the power spectral density of the indentation signal and $\mathrm{E}\,[\cdot]$ denotes the expected value operator.

For the sinusoidal indentation law considered here, the spectral density of the indentation displacement takes the form

$$S_{\Delta_1}(\nu) = \frac{\alpha^2}{4}\, (\delta(\nu - \omega) + \delta(\nu + \omega)) \tag{2.30}$$

where $\delta(\cdot)$ represents the Dirac delta function.

Substituting Equation (2.30) into the power equation and performing the integration leads to the final expression for the dissipated work during one oscillation cycle:

$$W = \frac{2\pi}{\omega} \int_{-\infty}^{\infty} \mathrm{Re}\big[S_{\mathcal{F}_1\dot{\Delta}_1}(\nu)\big]\; d\nu = \pi\; \mathrm{Im}[\hat{\kappa}(\omega)]\, \alpha^2, \tag{2.31}$$

This expression demonstrates the energy dissipation resulting from hysteresis in viscoelastic indentation. Specifically, the dissipated work is proportional to the imaginary component of the complex contact stiffness, which is directly associated with the material's loss modulus.

Equation (2.31) indicates that the dissipated work is proportional to the square of the oscillation amplitude.

$$W \propto \alpha^2, \tag{2.32}$$

indicating that an increase in indentation amplitude results in a greater volume of material participating in the cyclic deformation process.

The pull-off phenomenon during vertical harmonic oscillations, as shown in [37], arises from the complex interaction of the indenter motion and the viscoelastic response. This phenomenon occurs when the characteristic velocity of the oscillatory motion is large compared to the relaxation capacity of the material and the material is unable to redistribute the stresses during the loading period. As a result, during the unloading phase, the response lags behind the displacement, the contact pressure decreases and partial separation occurs at the interface.

This mechanism is governed by the balance between frequency and relaxation time: at high frequencies the material behaves in an elastic-like manner and cannot fully relax, whereas at low frequencies it has sufficient time to respond viscously and maintain contact [37]. The concept of an *incipient tapping front* is used to describe this transition; this limit defines the boundary between continuous contact and the onset of periodic separation.

Within this framework, tapping is assumed to initiate when the amplitude of the oscillatory component of the normal force becomes equal to the mean force associated with the static indentation, thus defining a critical condition for detachment given by

$$\left|\hat{\mathcal{F}}_1(\omega)\right| - \mathcal{F}_0 = 0. \tag{2.33}$$

By exploiting Equation (2.22) and (2.25), this condition can be reformulated in terms of the critical amplitude of the oscillatory indentation component $\alpha(\omega)$ required to trigger detachment, yielding

$$\alpha(\omega) = \mathcal{E}_0 \left(\Delta_0 - h \sin^2\!\left(\pi a_0/\lambda\right)\right) |\mathcal{E}(\omega)|^{-1}. \tag{2.34}$$

which explicitly shows that the "incipient tapping front" is inversely proportional to the value of the complex modulus $|\mathcal{E}(\omega)|$ (ignoring inertia and rigid body motion). That is, as the frequency increases and the material becomes stiffer,larger oscillation amplitudes are required to induce detachment, while at lower frequencies a softer response facilitates pull-off.

Specifically, at high frequencies and for small values of a_0/λ, the critical amplitude is $\alpha(\infty) \approx \Delta_0/\beta$, whereas at low frequencies it is $\alpha(0) \approx \Delta_0$. These results indicate that the onset of pull-off is mainly determined by the frequency–material relaxation interaction, and are consistent with the observations reported in [37].

2.3 Results and discussion

2.3.1 Dynamic Mechanical Analysis of NBR

Experimental tests start with DMA analysis of an NBR sample measuring 4 cm by 5 mm by 5 mm. This step yields the viscoelastic parameters needed for numerical simulations and analytical models in the subsequent sections. Since the mechanical response of viscoelastic materials strongly depends on the time scale of deformation, accurate determination of frequency-dependent properties is essential for a correct description of the behavior under dynamic loading such as cyclic indentation.

To achieve this, an extensive dynamic mechanical analysis (DMA) test was conducted, including both temperature and frequency sweeps, in accordance with established methodologies [35, 31, 82, 123]. These tests enable determination of the complex viscoelastic modulus of the material across a broad frequency range. Specifically, DMA measurements yield two principal parameters that characterize viscoelastic behavior: the storage modulus Re $\mathcal{E}(\omega)$ and the loss modulus Im $\mathcal{E}(\omega)$.

The storage modulus provides information about the elastic component of the viscoelastic response and characterizes the energy stored in the material during deformation and subsequently released. The loss modulus represents the viscous component and measures the energy dissipated as a result of molecular rearrangement and chain mobility. Together, these two parameters determine the complex modulus and fully describe the mechanical behavior of the material under oscillatory loading. The results of the DMA analysis are presented in Figure 2.3.

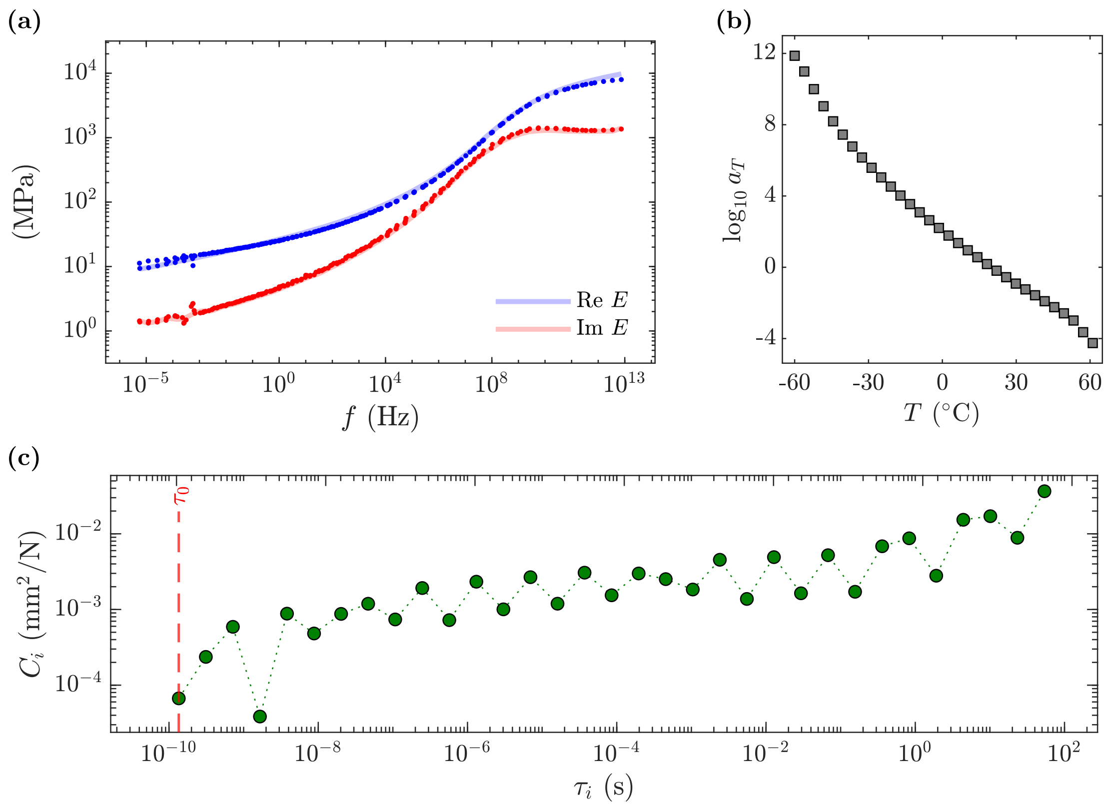

Figure 2.3: Illustration of the viscoelastic modulus master curves obtained from DMA analysis for Nitrile Rubber (NBR). The storage modulus is shown as the blue line and the loss modulus is shown as the red line, and is denoted as Re $\mathcal{E}(\omega)$ and Im $\mathcal{E}(\omega)$, respectively. (a) The viscoelastic modulus shift factors are plotted as a function of temperature a_T (b); the compliances C_i are characterized as a function of the relaxation times τ_i for NBR. (c). The reference temperature of the analyses is taken to be $T_0 = 20$°C.

Panel (a) of Figure 2.3 presents the master curves of the viscoelastic modulus for the NBR material. The blue curve indicates the storage modulus Re $\mathcal{E}(\omega)$, while the red curve indicates the loss modulus Im $\mathcal{E}(\omega)$. These curves characterize the material's response across a broad frequency range, illustrating the respective contributions of elastic and viscous effects as a function of loading rate. At low frequencies, the behavior is mainly determined by viscous relaxation, while at high frequencies the elastic component dominates because the chains do not have time to rearrange.

Panel (b) of Figure 2.3 shows the temperature dependence of the temperature shift coefficients a_T obtained by the Time–Temperature Superposition (TTS) principle. In this analysis, the reference temperature of $T_0 = 20°$ was chosen. These shift coefficients enable the extrapolation of experimentally measured viscoelastic properties to a broader frequency range, thereby encompassing behaviors beyond the direct measurement capabilities of laboratory experiments. According to the TTS principle [123, 124, 125], the viscoelastic modulus at any temperature and frequency can be expressed as follows:

$$\mathcal{E}(\omega, T) = \mathcal{E}\big(a_T\,\omega,\, T_0\big) \tag{2.35}$$

This relationship allows the experimental data obtained at different temperatures to be combined into a single and continuous master curve by shifting the data along the frequency axis. As demonstrated in the literature [35, 77, 126, 127], this method significantly broadens the accessible frequency range and provides a more comprehensive characterization of the material's viscoelastic behavior. In this study, the validity of the TTS principle for the NBR sample is confirmed by the agreement of the storage and loss moduli [35]. In particular, the relationship between these moduli is consistent with the Kramers–Kronig relations [128]. These mathematical conditions indicate that the measured viscoelastic response is physically correct and consistent with the linear viscoelastic model. This agreement confirms that the material behaves in the linear viscoelastic regime under the deformation conditions considered and supports the validity of the assumptions employed in the numerical modeling.

Panel (c) of Figure 2.3 presents the relaxation spectrum of the material by plotting the fitting coefficients C_i against the corresponding relaxation times τ_i on a logarithmic scale. These parameters are determined by fitting the dynamic mechanical analysis (DMA) data in the frequency domain using the creep function described in Section 2.2. This approach enables the continuous viscoelastic response of the material to be approximated by a spectrum of discrete relaxation processes, where each process is characterized by a distinct relaxation time [129].

The obtained compliance spectrum covers a very wide range of relaxation times. It extends from approximately 10^{-10} seconds to 10^{2} seconds. This wide distribution reflects the complex internal structure of the material and the multiple molecular mechanisms active over different time scales. As a result, the mechanical response depends strongly on the rate of deformation: at high rates the elastic response dominates, while at low rates, viscous relaxation mechanisms dominate.

This wide relaxation spectrum indicates that viscoelasticity determines the behavior of the NBR material over a very wide time interval. A correct understanding of this time dependence is of great importance for predicting the dynamic indentation behavior and explaining the energy dissipation mechanisms observed under cyclic loading.

2.3.2 Stress Relaxation and Harmonic Indentation Experiments

The stress relaxation response of viscoelastic materials has been investigated through a series of controlled indentation experiments. [130, 131, 132, 133]. These tests are regarded as a primary method for studying viscoelastic behavior because they allow us to observe how the internal stresses over time while the applied deformation remains constant. In a typical relaxation experiment, the material is deformed to a predetermined displacement, which is then held constant. [130, 132, 134]. At this time, the reaction force of the material gradually decreases as internal stresses within the polymer network are relieved through viscoelastic relaxation. Figure 2.4 presents the results of the stress relaxation experiments alongside the corresponding numerical simulation outcomes.

As shown in Figure 2.4, three different tests were performed with indentation amplitudes of 0.1 mm, 0.2 mm and 0.3 mm. In all cases, the indentation step was applied at a constant speed of 1 mm/s. Upon reaching the target depth, the indenter remained constant for 600 seconds, during which the stress relaxation behavior of the material was monitored. For each loading condition, both experimental data and numerical simulations were collected to evaluate the model's accuracy in describing the time-dependent response of the viscoelastic substrate.

At an indentation amplitude of 0.1 mm, the normal force rises quickly and peaks at approximately 23.1 N immediately after reaching the target depth. This rapid increase indicates the material's initial elastic response, as the polymer chains have not yet begun to rearrange.

Following the initial peak, a distinct stress relaxation phase is observed. Due to internal relaxation processes such as molecular rearrangement and stress redistribution, cause the measured force decreases gradually. Over time, the force stabilizes and, after approximately 200 seconds, approaches a plateau of about 12.2 N. At the same time, the indentation displacement reaches 0.1 mm and remains almost constant for the rest of the time. This indicates that the decrease in force is not due to additional deformation but to relaxation processes within the material.

Numerical simulations based on the proposed modelling framework successfully reproduce the experimental behaviour. In particular, both the initial force peak and the subsequent relaxation trend are accurately described. Small discrepancies

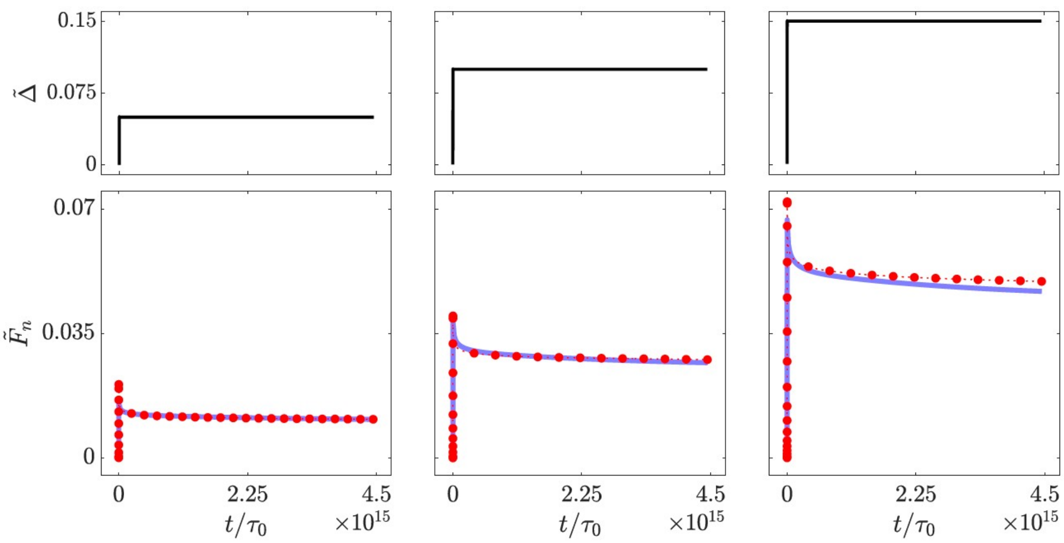

Figure 2.4: Stress relaxation curves obtained for different values of the dimensionless penetration $\tilde{\Delta} = \Delta/R$, where the indenter radius is $R = 2$ mm. The three panels correspond to $\tilde{\Delta} = 0.05$ (left), $\tilde{\Delta} = 0.1$ (center), and $\tilde{\Delta} = 0.15$ (right). On the left vertical axis, the experimentally measured normal force (red dots) is compared with the numerical prediction obtained from the model (solid blue line). On the right vertical axis, the imposed indentation displacement is reported (solid black line).

are observed in the initial relaxation phase; these differences can be explained by simplifying assumptions in the constitutive model or by experimental uncertainties.

A similar relaxation behavior occurs in the second test with an indentation amplitude of 0.2 mm. During loading, the force rises quickly and reaches a maximum of approximately 44.7 N due to the larger deformation. The system then enters a relaxation phase, where the force gradually decreases and stabilizes around 31 N after about 200 seconds. The indentation displacement remains stable at 0.2 mm. Numerical simulations show good agreement with experimental measurements. The calculated force response follows the relaxation trend correctly, indicating that the model adequately describes the viscoelastic behavior. Although small differences are observed in the initial stage of relaxation, especially near the initial peak, the long-term plateau behavior is recovered with high accuracy.

The third experiment was performed with a larger 0.3 mm indentation amplitude and allowed to evaluate the behavior of the material at higher deformation levels. In this case, the force reaches a maximum of about 80.6 N, which is consistent with a larger indentation. After loading, the force gradually decreases during the relaxation phase and approaches a plateau value around 55.5 N after about 200 s. The indentation displacement, however, remains constant after reaching 0.3 mm.

Numerical simulations accurately reproduced this behavior. The calculated curves closely matched the experimental results, particularly during the long-term relaxation phase. Minor differences in the initial peak and early relaxation phase were observed, but these discrepancies were small relative to the overall force level.

The stress relaxation tests demonstrate consistent viscoelastic behavior across all three indentation amplitudes. The time-dependent force variation can be categorized into three phases: initial elastic loading characterized by a rapid increase, a relaxation phase marked by a gradual decrease, and a stable plateau phase as the system approaches equilibrium. Although the indentation amplitude increases, the shape of the relaxation curves remains unchanged; this indicates that the material remains in the same viscoelastic regime over the range considered. The good agreement between the experimental results and the numerical simulations confirms that the modeling framework accurately describes the viscoelastic behavior and justifies its application to more complex loading cases, especially harmonic indentation problems.

The next stage of the experimental program involves harmonic tests, conducted following the initial relaxation tests. Harmonic tests enable the investigation of material response under cyclic loading conditions, including the determination of frequency dependence [82, 123, 76], phase lag between force and displacement [135, 131], and energy dissipation mechanisms [136, 79]. Whereas relaxation tests reveal a decrease in stress under constant deformation, harmonic tests provide a more comprehensive description of the material's dynamic behavior and are more representative of practical applications. Normal indentation tests under harmonic loading were subsequently performed on the NBR material, which had previously been characterized by dynamic mechanical analysis (DMA). These tests constitute the main experimental part of the study, and the aim is to investigate the dynamic contact response under cyclic loading and to directly compare the results with the predictions of a numerical model based on the Boundary Element Method (BEM).

The results of these harmonic indentation experiments are summarized in Figure 2.5.

The indentation tests were designed using a two-stage loading protocol to ensure that the material achieved a steady state prior to the application of oscillatory loading. During the first stage, a rigid indenter is pressed into the NBR surface to a predetermined average indentation depth. This depth is represented in dimensionless form as follows:

$$\tilde{\Delta}_0 = \frac{\Delta_0}{R}, \tag{2.36}$$

Here, R denotes the radius of the cylindrical indenter used in the experiment. For these tests, the average indentation was set to $\tilde{\Delta}_0 = 0.05$. Upon reaching this value, the indenter position was maintained for 600 seconds.

The waiting phase in viscoelastic testing is essential because it permits internal stresses to relax under constant deformation. At this time, the polymer chains

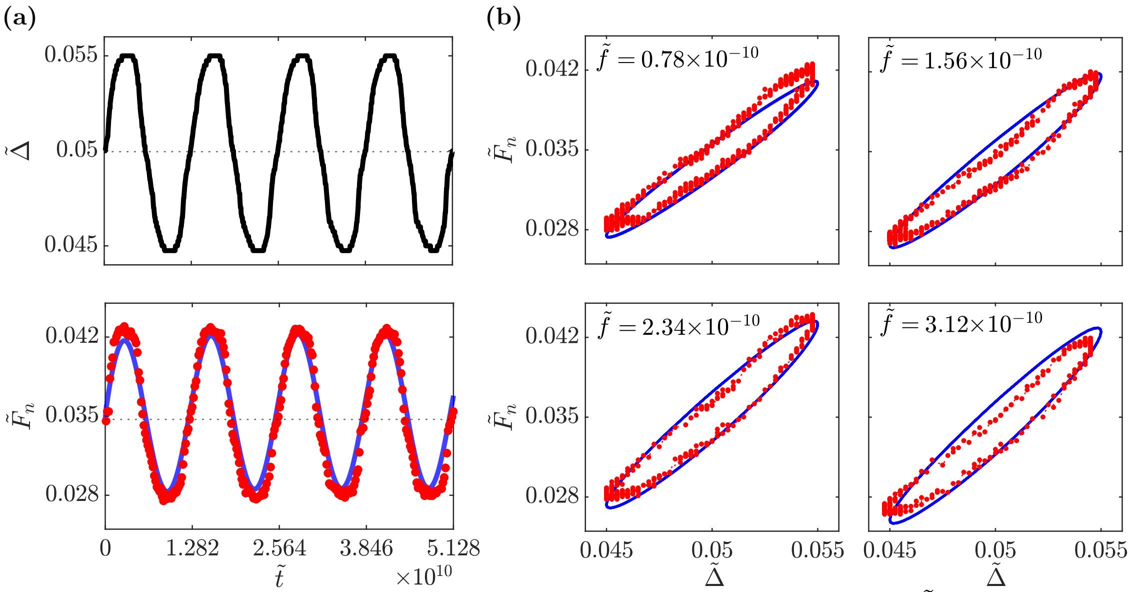

Figure 2.5: The upper left panel displays the dimensionless penetration $\tilde{\Delta} = \Delta/R$ (black line) as a function of dimensionless time $\tilde{t}$ at an indenting frequency $\tilde{f} = 0.78 \times 10^{-10}$. In the lower panel, (a) compares the dimensionless normal force $\tilde{F}_n = F/(E_0 \lambda d)$, where d is the out-of-plane thickness, between experimental data (red dots) and numerical results (blue line). Panel (b) shows $\tilde{F}_n$ versus $\tilde{\Delta}$ for various indenting frequencies $\tilde{f} = f\tau_0$.

are rearranged, the stresses are reduced, and the material approaches a quasi-equilibrium state. This process enables a more accurate evaluation of the effects of subsequent oscillatory loading and minimizes transient effects.

Following the relaxation phase, a sinusoidal oscillatory displacement is applied to the average indentation during the second part of the experiment. The oscillatory amplitude is represented in dimensionless form as follows:

$$\tilde{\alpha} = \frac{\alpha}{R}, \tag{2.37}$$

and was set equal to $\tilde{\alpha}^* = 0.005$. The oscillation frequency was also expressed in dimensionless form as

$$\tilde{f} = f\tau_0, \tag{2.38}$$

where $\tau_0 = 1.56 \times 10^{-10}$ s represents the characteristic relaxation time obtained from the relaxation spectrum shown previously in Figure 2.3 (c).

Selecting these parameters ensures that the oscillatory motion remains within the small-amplitude indentation regime, thereby maintaining the material response in the linear viscoelastic range as defined by DMA. This loading protocol also provides critical information regarding dynamic stiffness and energy dissipation mechanisms.

It is important to emphasize that, during harmonic indentation, the contact area between the indenter and the viscoelastic substrate is not constant, but rather evolves continuously throughout the oscillation cycle. As the indenter moves towards and away from the surface, the contact region expands and contracts accordingly. This variation in contact area introduces additional complexity into the mechanical response of the system. In particular, the changing contact geometry leads to a redistribution of stresses within the viscoelastic body, causing the material to experience a loading condition that effectively contains multiple frequency components beyond the fundamental oscillation frequency imposed by the actuator. As a result, the indentation experiment simulates a complex mechanical environment in which the material response is influenced by a spectrum of effective deformation rates.

Another important point to consider is the actual shape of the indentation signal applied during the experiment. Ideally, the displacement should be perfectly sinusoidal. However, as shown in Figure 2.5(a), the signal recorded during the experiment exhibits slight deviations from this ideal shape. These deviations arise from the physical limitations of the experimental setup: factors such as the dynamic response of the actuator, inaccuracies in the control system, and the mechanical flexibility of the test rig. Although these differences are relatively small, they are an inevitable feature of real experimental systems and must be taken into account when comparing experimental results with numerical simulations.

The upper panel of Figure 2.5 (a) illustrates the time dependence of the applied indentation depth. The lower panel displays the corresponding normal force response obtained experimentally, alongside the force predicted by the numerical boundary element method (BEM) model, both using the same harmonic displacement signal as input. This comparison is conducted for the following dimensionless oscillation frequency:

$$\tilde{f} = 0.78 \times 10^{-10}. \tag{2.39}$$

Based on the qualitative evaluation of the results, we can say that a high level of agreement is observed between the experimental measurements and the numerical predictions. In particular, we can accurately observe both the amplitude and phase characteristics of the force signal generated during the numerical model oscillation. This agreement indicates that the numerical methodology developed within the framework of the study is capable of correctly describing the main features of the viscoelastic contact response, even under dynamic loading conditions where the contact geometry is constantly changing.

To further examine the influence of loading frequency on the viscoelastic behavior of the material, harmonic indentation tests were conducted at various dimensionless frequencies $\tilde{f}$, with the oscillation amplitude held constant. Panel (b) of Figure 2.5 presents the results, showing the measured normal force as a function of indentation depth for each frequency.

The obtained force-indentation curves form closed hysteresis loops, which are characteristic of viscoelastic materials subjected to cyclic deformation. These loops are formed due to the non-coincidence of the loading and unloading paths: during each oscillation period, part of the mechanical energy supplied to the system is lost through viscous processes occurring within the polymer structure. As a result, the area remaining inside the hysteresis loop represents the energy dissipated during one loading cycle.

Comparison of hysteresis loops for different frequencies shows that as the frequency increases, the loops become wider and longer, indicating that the energy dissipated increases. This suggests that viscous mechanisms are more dominant at high loading rates. When deformation occurs rapidly, the polymer chains do not have enough time to relax, resulting in increased internal friction and more energy loss.

Finally, when comparing the experimental hysteresis loops with those predicted by the numerical simulations, it becomes evident that the numerical model successfully captures the overall trends observed in the experimental data. Although minor discrepancies may appear in certain regions of the cycles, particularly at higher frequencies, the numerical predictions remain in good qualitative agreement with the measurements. This result confirms the reliability of the Boundary Element Method approach adopted in this work for modelling viscoelastic contact under harmonic indentation conditions.

2.3.3 Energy Dissipation and Analytical Approximation

In order to estimate the energy dissipation during cyclic indentation, a novel analytical formulation is proposed in this study, which allows to estimate the hysteresis work under harmonic oscillation conditions. Although numerical simulations based on the Boundary Element Method (BEM) describe the contact mechanics problem with high accuracy, the analytical approach allows to explain the system in a simpler and more understandable way. Through this formulation, it is possible to isolate the main physical parameters that determine the energy losses in viscoelastic contacts and effectively predict the dissipative behavior.

The results obtained from this analytical formulation are illustrated in Figure 2.6(a).

In particular, Figure 2.6 presents a contour map of the dimensionless dissipated work defined as

$$\tilde{W} = \frac{W}{\mathcal{E}_0 \, \lambda \, R}, \tag{2.40}$$

This indicator is determined using the analytical expression in Equation 2.31. Dissipated work is defined as a function of two dimensionless parameters: oscillation

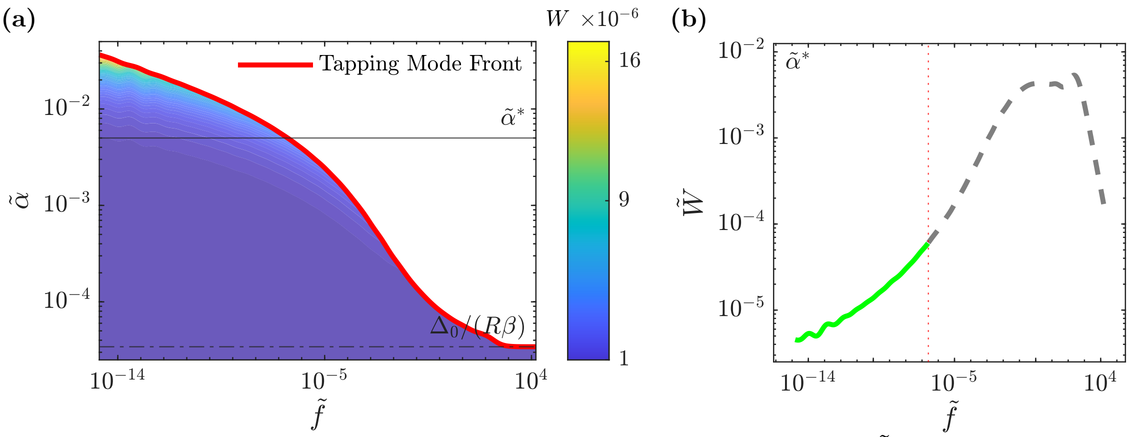

Figure 2.6: (a) Contour plot of the dimensionless dissipated work $\tilde{W}$, calculated using Eq. (2.31), for vertical harmonic oscillation of the punch as a function of dimensionless frequency $\tilde{f}$ and amplitude $\tilde{\alpha}$ at constant mean indentation $\tilde{\Delta}_0 = 0.05$. The red curve shows the analytical detachment boundary from Eq. (2.34), which separates the detachment region (white) from continuous contact. (b) Dimensionless dissipated work versus frequency for the critical amplitude $\tilde{\alpha}^* = 0.005$, illustrating the influence of the loss modulus Im $\mathcal{E}(\omega)$ as described by Eq. (2.31).

frequency $\tilde{f}$ and the oscillation amplitude $\tilde{\alpha}(\omega)$. In this approach, the average indentation depth is assumed to be constant $\tilde{\Delta}_0 = 0.05$ to isolate and clarify the effects of frequency and amplitude on the dissipative behavior can be analyzed and visualized more clearly.

The contour plot clearly shows how the energy dissipated varies under different loading conditions. In general, larger oscillation amplitudes and higher frequencies lead to more energy losses, since in this case the viscoelastic mechanisms within material are more active. This representation gives an overview of the parameters that determine the dynamic response of the system.

An important characteristic of the viscoelastic indentation process is evident in the time-dependent variation of contact pressure and displacement distributions obtained from numerical simulations. These distributions are shown in Figure 2.7.

Figure 2.7 presents the contact pressure distribution and the corresponding surface displacement on the viscoelastic substrate at various time points during the harmonic oscillation period. The simulation results correspond to a dimensionless frequency $\tilde{f} = 3.12 \times 10^{-10}$, an average indentation depth $\tilde{\Delta}_0 = 0.25$, and an oscillation amplitude $\tilde{\alpha} = 0.15$.

These results show that the viscoelastic material does not respond immediately to the indenter's oscillatory motion. Instead, a phase lag occurs between the applied indentation displacement and the resulting viscoelastic substrate deformation. This delay results directly from the time-dependent relaxation processes characteristic of viscoelastic materials.

As previously discussed in Ref.[37], in the context of periodic detachment, this

Figure 2.7: The pressure distribution at different time steps is characterized by the black line and the corresponding displacement distribution, the red line. The dotted red line shows the change in the position of the rigid indenter. In the simulation, the average displacement value is $\tilde{\Delta}_0 = 0.25$, the oscillation frequency is $\tilde{\alpha} = 3.12 \times 10^{-10}$ and the amplitude is $\tilde{\alpha} = 0.15$.

delayed response can result in the periodic detachment of the indenter from the surface during the oscillation period. During the unloading phase, when the indenter moves away from the substrate surface, the viscoelastic material does not recover rapidly enough to sustain contact. Under such conditions, the indenter temporarily loses contact with the substrate before re-establishing contact during the subsequent loading phase. This intermittent contact behavior is commonly referred to as tapping mode.

The presence of this tapping regime is clearly visible in the contour plot of Figure 2.6(a), where a tapping mode front separates the continuous-contact region from the detachment region. In the figure, the detachment region is represented by the white area, while the region above the front corresponds to conditions under which the indenter remains in continuous contact with the substrate throughout the oscillation cycle.

Analytical analysis of the tapping mode shows that two different asymptotic behaviors emerge at low and high frequencies. These behaviors arise from the dependence of the system response on the modulus of the complex viscoelastic modulus $\mathcal{E}(\omega)$, more precisely $1/|\mathcal{E}(\omega)|$. At low frequencies, the material has enough time to relax and continuous contact is maintained. At high frequencies, the material cannot fully adapt to the applied displacement, leading to a temporary loss of contact—i.e., the activation of the tapping mode.

At the same time, it is important to accurately know the complex modulus $\mathcal{E}(\omega)$ of the material in order to determine both the dimensionless dissipated work $\tilde{W}$ and the tapping limit $\tilde{\alpha}(\omega)$. In this study, these properties were obtained by Dynamic Mechanical Analysis (DMA). Reliable DMA data play a key role in correctly predicting the dissipative behavior of a viscoelastic contact system, both analytically and numerically.

Figure 2.6 (b) clearly demonstrates the effect of oscillation frequency on energy dissipation. The frequency dependence of the dimensionless dissipated work is presented for the critical amplitude $\tilde{\alpha}^*$. Analytical results indicate that dissipated work is strongly correlated with the loss modulus $\mathrm{Im}\ \mathcal{E}(\omega)$ of the material, which aligns with Equation 2.31. As the imaginary part represents the viscous component, higher values of $\mathrm{Im}\ \mathcal{E}(\omega)$ correspond to increased internal friction and greater energy dissipation. The graph differentiates between two regimes: the solid line represents continuous contact, while the dashed line denotes the tapping regime, where separation occurs.

The graph shows two regimes based on contact conditions. The solid line indicates continuous contact, where the indenter stays in contact with the substrate throughout the oscillation cycle. The dashed line indicates the tapping regime, where detachment occurs.

To validate the analytical and numerical predictions, we also evaluated the dissipated work experimentally by calculating the area of the force-displacement hysteresis loops from harmonic indentation. Figure 2.8 compares the experimental results with the theoretical predictions.

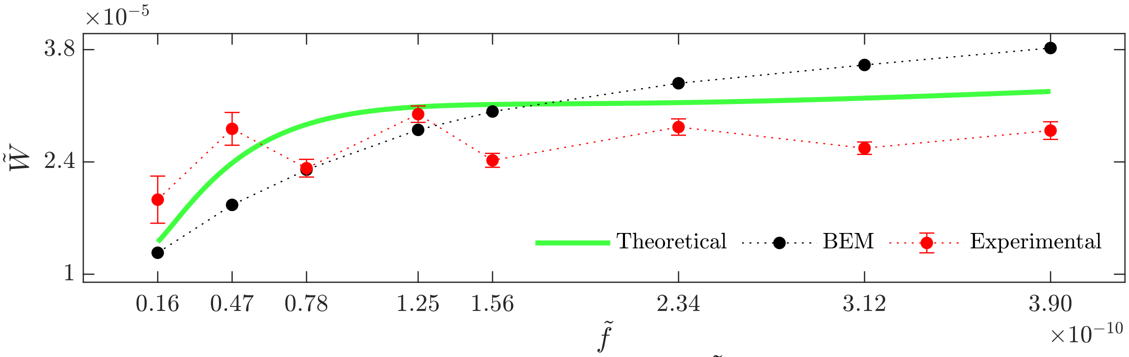

Figure 2.8: The graph compares the dissipated work $\tilde{W}$ during the vertical oscillation of the punch at different frequencies. Dashed lines with red dots indicate experimental measurements at ten frequencies, while the solid green line shows theoretical results. The dashed line with blue dots represents Boundary Element Method (BEM) analyses based on Eq. 2.31.

Figure 2.8 compares the dimensionless dissipated work from three different sources: the analytical formulation derived from Equation 2.31, numerical simulations based on the Boundary Element Method (BEM), and experimental measurements obtained with the Biomomentum MACH-1 v. 4.5 instrument. The results show good agreement between experimental and numerical predictions, confirming that the BEM model accurately describes viscoelastic energy dissipation during cyclic indentation. Some differences are observed at higher frequencies, which is consistent with the behavior seen in hysteresis loops.

It should be noted that the numerical model developed in this study considers only the normal contact problem and does not include normal–tangential interactions. In real systems, tangential forces can cause stick–slip phenomena at the contact surface and create additional energy dissipation mechanisms [137]. However, these effects are usually significant only when there is a strong elastic inhomogeneity between the materials (for example, in cases characterized by Dundurs parameters) or when the viscoelastic layer is very thin [138, 139].

In the present case, it is justified to ignore these effects. The thickness of the viscoelastic layer used is much larger than the characteristic dimensions of the contact area and the Poisson's ratio of the material is approximately $\nu = 0.5$ [138, 139]. Under these conditions, the interaction between normal and tangential contact problems becomes weak, and using only the normal indentation model is sufficient to accurately describe the behavior of the system.

Furthermore, the current formulation does not explicitly consider adhesion effects or nonlinear viscoelastic behavior. However, the strong agreement between numerical results and experimental measurements suggests that the primary mechanisms governing the viscoelastic response are effectively represented by the model.

Although the analytical formulation is based on simplifying assumptions such as ideal sinusoidal indentation, it shows a fairly good agreement with the experimental results, especially at medium and high frequencies. The observed differences at low frequencies can be explained by these simplifications and the small deviations of the real experimental signal from the ideal sinusoid.

Nevertheless, the analytical approach provides both a useful and computationally efficient tool for estimating energy dissipation in viscoelastic contacts under harmonic loading.

The results obtained show that the Boundary Element Method (BEM) combined with the analytical formulation proposed in this study successfully reproduces the experimental behavior of viscoelastic indentation systems both qualitatively and quantitatively. This feature is of great practical importance, since the model allows for the prediction of the dissipative performance of viscoelastic components such as vibration dampers and polymer bearings.

Furthermore, the developed methodology can also be used as a valuable tool for the mechanical characterization of soft and biological materials [140, 141, 6, 142]. Indentation tests are widely used to determine the viscoelastic properties of such materials [143]. Since a reliable relationship is established between the viscoelastic modulus of the material and the observed mechanical response, this framework provides a powerful approach for the correct interpretation of experimental results and the extraction of key material parameters.

Chapter 3

Impact Response of Viscoelastic Solids

The dynamic interaction between impacting bodies and solid surfaces is one of the fundamental problems of contact mechanics and plays an important role in a wide range of engineering applications. In tribological systems, these interactions determine processes such as friction, wear, and surface damage; in particular, in bearings [144], gears [145], and rolling contacts [146], repeated micro-impacts directly affect the durability and efficiency of components. Viscoelastic contacts are widely used in the field of shock absorption and vibration control. In automotive suspensions, aerospace structures, and protective equipment, the ability of materials to dissipate energy through internal friction is crucial for reducing transmitted forces and preventing structural fatigue [76, 147, 70].

Furthermore, the mechanics of particle–surface collisions are key to granular materials and particulate systems. In areas such as powder processing, pharmaceutical manufacturing, and geophysical flows, where the collective behavior of particles is strongly influenced by individual collision dynamics and energy dissipation mechanisms. Understanding stress and contact development from impact in protective coatings and surface engineering is essential for designing materials resistant to erosion, impact wear, and repeated loading. This is especially important for systems in harsh environments, including turbine blades, pipelines, and cutting tools [148]. Controlling small-scale impact and contact behavior is also increasingly important in emerging fields such as additive manufacturing and soft material design. This enables purposeful shaping of mechanical response and material performance [149].

Furthermore, viscoelastic impact phenomena are of direct relevance to energy dissipation systems. In these systems, materials are specifically designed to absorb and redistribute kinetic energy; these include applications such as automotive crashworthiness, packaging systems, and sports equipment [76, 150]. The effectiveness of these systems is determined by the interplay among material rheology, impact velocity, and contact evolution, which necessitates precise experimental and theoretical descriptions of dynamic contact.

Within this broader context, the normal impact of a spherical body on a hard surface is considered a classical (canonical) model problem. Its simple geometry allows for the application of analytical approaches, and the main starting point in this field has been the Hertzian contact theory [41]. Despite this simplicity, the model correctly describes the basic mechanisms such as contact deformation, stress distribution and energy transfer, and is therefore used as a fundamental reference point for more complex problems. For this reason, this configuration has been widely studied, both for the development of predictive models and for applications where impact and contact mechanics are important. The classical theory establishes the relationship between contact force, indentation depth and contact radius under quasi-static conditions, which forms the basis of elastic contact [41]. As discussed in Chapter 1, materials such as polymers and elastomers exhibit viscoelastic properties. These characteristics result in time-dependent deformation, hysteresis, and energy dissipation. Notably, these phenomena cannot be fully described by elastic models alone.

To address these limitations, Hertzian contact theory has been developed in various directions. In early studies, Lee and Radok and Hunter proposed contact models within the framework of linear viscoelasticity, which allowed for a better understanding of time-dependent indentation and relaxation processes [42, 43]. Subsequently, these models were applied to impact problems, demonstrating that inertia, material rheological properties of the material and how the contact develops together determine the dynamic behavior of the system. In such cases, the impact of a viscoelastic sphere on a rigid surface is characterized by velocity-dependent deformation, partial energy recovery, and velocity-dependent restitution.

Experimental work on the impact of viscoelastic spheres has mainly focused on indicators that describe the overall (global) response of the system - for example, contact time, coefficient of restitution and force-time graphs. For example, Collins investigated the viscoelastic behavior of polymers through ball drop experiments and emphasized the role of energy dissipation mechanisms during repeated impacts [46, 47].In the same vein, Zhang and co-workers showed that viscoelastic effects significantly affect the bounce behavior by studying how deformation and contact time depend on impact velocity [45]. In more recent studies, such as Jian, experimental results have been combined with numerical models to more accurately predict contact forces and restitution [49]. On the other hand, Kunzemann modelled ball drop tests using finite element methods and successfully described nonlinear contact dynamics [48].

Although significant progress has been made in this area, much of the current research is still based on indirect measures of the contact process. Typically, parameters such as force, indentation depth, or coefficient of restitution are measured, but these do not fully reflect how the contact evolves locally. In particular, it is rarely possible to directly measure how the contact area changes over time during impact — this is mainly due to technical difficulties associated with high temporal resolution and optical observation. Although high-speed imaging has partially overcome this problem in some recent studies, the simultaneous measurement of displacement and contact area and their comparison within a single model is not yet widespread [149].

Taking this gap into account, the present study aims to investigate viscoelastic impact more fully, both experimentally and numerically. For this, an acrylic spherical indenter is dropped from certain heights onto a hard sapphire substrate and controlled, reproducible impact conditions are created. The dynamic response of the system is measured using a laser displacement system with high time resolution. In parallel, a high-speed camera placed under the transparent sapphire disk allows direct monitoring of the time evolution of the contact area.

The main advantage of this approach is that for the first time, both global kinematic data (displacement) and local contact properties (change in contact radius) are obtained simultaneously. This opens up new possibilities for a deeper understanding of viscoelastic impact mechanics.

Alongside the experimental studies, a special numerical model was developed to describe the viscoelastic impact process. This model makes it possible to directly compare theoretical predictions with experimental results. Combining both experimental and numerical approaches allows for a deeper understanding of the energy dissipation mechanisms, how contact changes over time, and rebound behavior. The obtained results provide a new view of the dynamic interaction between the rheological properties of the material and the contact mechanics. This, in turn, creates important practical opportunities for the development of impact-resistant materials, the construction of more effective damping systems, and the optimization of tribological interfaces.

3.1 Materials and Experimental Methods

The experimental setup used to investigate the contact area between an impacting ball and a sapphire disc was designed to provide precise control over drop conditions and to enable detailed visualization of the contact interface during impact.

The system features a rigid aluminum frame supporting the drop mechanism, a Keyence Laser for displacement measurement, and optical imaging components for simultaneous visualization of displacement and the contact interface (see Figure 3.1). An electromagnetic release mechanism at the top ensures controlled, repeatable sphere release. Drop height is precisely adjusted with high precision by a micrometer, which ensures that the sphere is positioned in the correct position before release.

A 3D-printed aligner was employed to center the metal holder containing the sphere. This component ensures proper alignment during the drop and minimizes lateral movement.

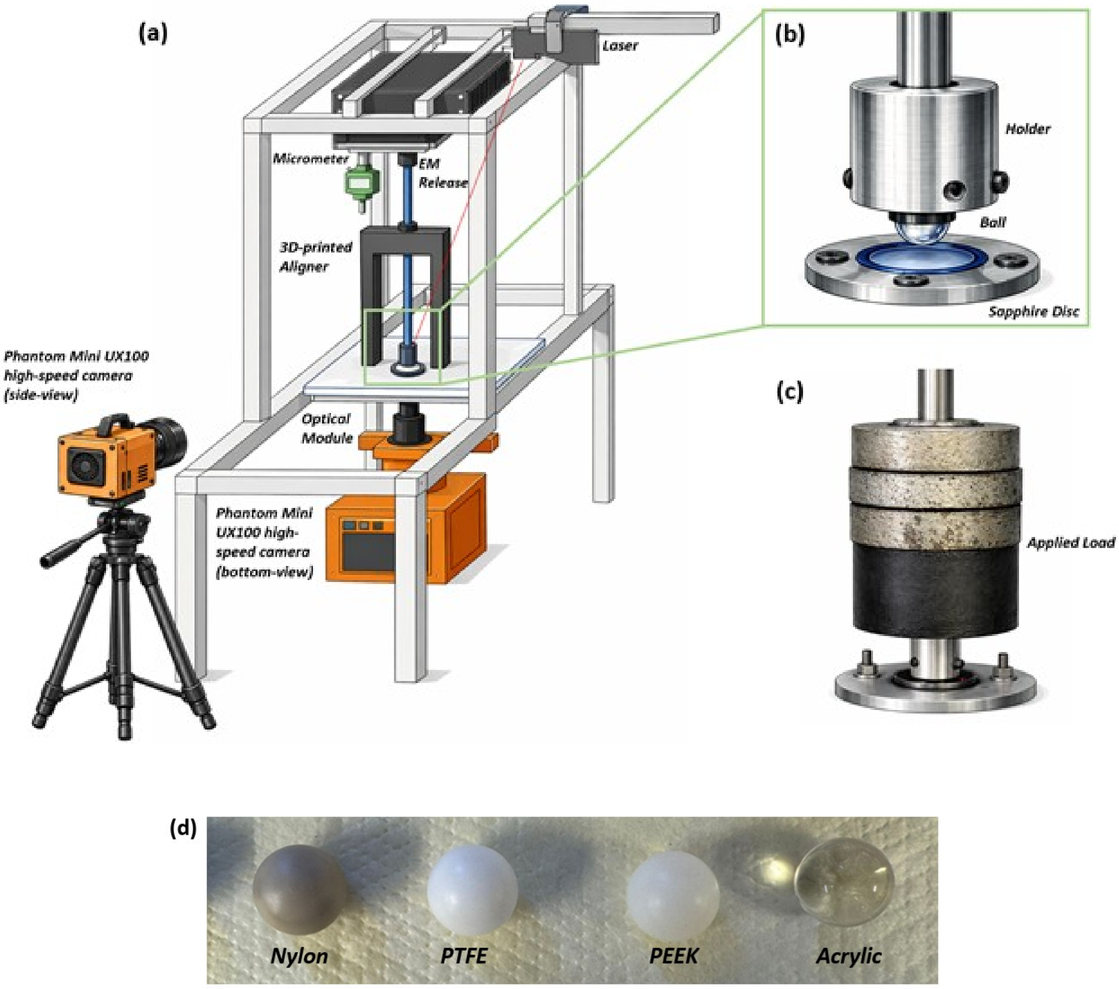

Figure 3.1: (a) General view of the experimental setup for the ball drop test, equipped with electromagnetic release, micrometer height adjustment, 3D printed holder, laser sensor, and high-speed camera; (b) close-up view of the holder-ball-sapphire contact area; (c) loading configuration of weights attached to the holder, intended for the static test; and (d) 3/4-inch Nylon, PTFE, PEEK, and Acrylic spheres manufactured by PCS Instruments and used in the tests.

PTFE, PEEK, Nylon, and Acrylic spheres with a diameter of 3/4 inches ($R = 9.525\,\mathrm{mm}$) were used in the experiments. The total mass of the metal holder to which the spheres were attached was 500 g. The sphere-holder system was dropped from heights of 1.5 mm, 5 mm, 7 mm, and 10 mm, mm onto a sapphire disk serving as a hard impact surface. This approach enabled a systematic investigation of the effect of impact energy on the contact area.

The vertical displacement of the holder during impact was measured using a laser displacement sensor mounted at an angle to the upper part of the frame. The laser beam was directed directly at the metal holder, and its movement was recorded continuously throughout the impact. The sensor operated with a time step of 50 μs and a sampling frequency of 20 kHz. In order to eliminate the projection effect on the measurements due to the inclined placement of the sensor, a geometric correction factor was applied during calculations.

For all subsequent experimental tests, displacement is measured by laser and must first be verified. To achieve this, an optical module consisting of a Phantom Mini UX100 high-speed camera is positioned in front of the holder to record its movement under controlled illumination at 10,000 frames per second, enabling detailed observation of the rapid evolution of the contact area during the short impact event. To compare displacement results with those from the laser, an optical method using Digital Image Correlation (DIC) is applied to the camera images (see Figure 3.8 (a)). To analyze displacement, a foreground and reference point are identified in the images. For this purpose, a blue reference line connecting selected sub-areas along the lower edge of the holder was selected and the displacement was calculated by tracking its movement in successive frames. This method relies on gray tone correlation and provides sub-pixel accuracy. Displacement is initially measured in pixels and then converted to physical units by calibration 0.07772 mm/pixel based on a 30 mm mm reference length on the holder. The data is further processed in MATLAB. Although laser and DIC measurements were conducted in separate sessions, specific 3D-printed support elements were used at each height to maintain consistent drop conditions.

After validating displacement measurements, we used a new experimental setup to study contact area development. A high-speed camera was positioned beneath the sapphire disc and directly observed the contact interface during impact. We repeated the experiments under identical drop conditions and heights. Contact area analysis focused on the acrylic sphere, as its transparency allowed optical monitoring of the contact area. The transparent acrylic sphere and an interferometric setup, based on Ovcharenko's method [151], enabled visualization of the contact area through a sapphire disc. Interference fringes at the interface provided enough contrast for precise contact area measurement (see Figure 3.14).

Following the contact area measurements, additional experimental tests were performed to evaluate the effect of temperature on the contact response of the acrylic sphere (see Figure 3.1). The acrylic sphere was heated to approximately 39 °C using a heat gun and dropped onto a sapphire disk from a height of 10 mm under the same conditions. This method enabled a direct comparison of contact area development at elevated and room temperatures.

Prior to experimentation, the optical system was calibrated to establish the spatial scale of the images. The influence of the 10× objective lens positioned before the beam splitter cube was incorporated, yielding a conversion factor of

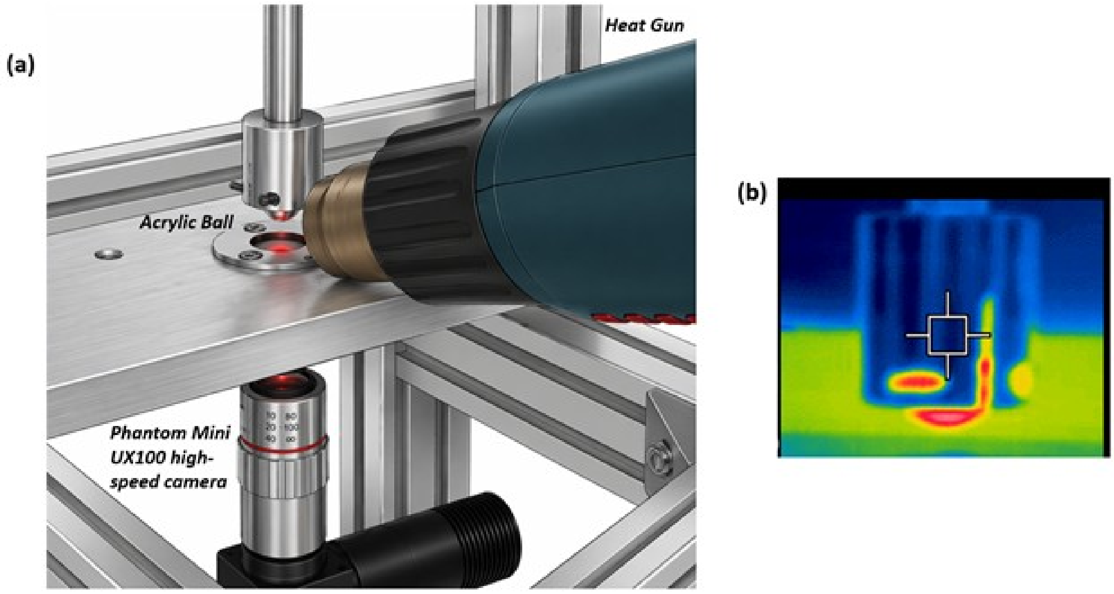

Figure 3.2: Experimental setup and temperature measurement for studying the contact analysis of acrylic sphere at high temperatures (a) Schematic representation of the experimental configuration, where an acrylic sphere mounted on a vertical holder impacts the substrate, while localized heating is applied using a heat gun. The contact event is recorded from below using a Phantom Mini UX100 high-speed camera. (b) Thermal image of the contact area obtained using an infrared thermometer, showing the controlled temperature of approximately 39 °C.

2.17 μm/pixel per pixel. This calibration enabled precise calculation of the contact radius and the corresponding contact area from the recorded images.

This experimental setup is particularly complex because it is required to measure the global kinematics of the impacting body and the local evolution of the contact interface simultaneously and under high-speed transient conditions. Penetration must be recorded by high-frequency displacement measurements, while the contact area must be determined optically at the micrometer level. These two quantities are on different scales in both space and time: while the global motion occurs at the millimeter level, the contact area evolves at micrometer scales and over a time interval of approximately 10^{-3} s. Therefore, precise synchronization of the measurement systems is necessary; otherwise, even small time differences can prevent the correct correlation of the corresponding contact state with the motion of the sphere.

The extremely brief duration of contact during impact complicates imaging of the precise moment of contact, particularly the initial contact.The short event duration limits the number of frames captured, thereby increasing uncertainty in determining the temporal evolution of the contact radius), and also places serious demands on image quality. The contact boundary is identified by interference fringes, which are sensitive to noise, optical alignment, and surface conditions. Additional challenges include ensuring precise alignment of the impacting body (to maintain axisymmetric conditions), as well as the high sensitivity of the measurements to small disturbances such as vibrations or slight tangential movements. For this purpose, a specially printed aligner was used during the tests. At the same time, plate vibration was studied separately; see Appendix B.

Following the dynamic impact experiments, additional tests were conducted under quasi-static loading to study the time-dependent contact response of the material. In this configuration, the same ball-and-disc system was employed, consisting of a PTFE ball mounted on a holder in contact with a sapphire disk. Quasi-static tests were performed on the same frame as the dynamic tests, but the loading was applied incrementally by placing calibrated masses on the holder. Initially, the system was subjected to the holder's own weight of 0.5 kg for 3 minutes, followed by normal loading at approximately every 15 min, first 2 kg, then 1 kg, 1 kg, and 1 kg. Sufficient time was provided between each load increment to observe the time-dependent response of the material. This methodology enabled evaluation of both the instantaneous elastic response and the time-dependent deformation behaviour associated with creep (see Figure 3.17 (c)). The vertical displacement of the holder was measured using a laser displacement sensor.

The obtained laser measurements were performed with a time resolution of 5 s, which allowed monitoring of both the instantaneous elastic response and the subsequent viscoelastic creep. Appropriate geometric correction was applied to eliminate errors caused by the inclined placement of the laser.

All experimental spheres were supplied by PCS Instruments (see Figure 3.17 (d)). After impact testing, the spheres were cut and samples were prepared for material characterization. Dynamic Mechanical Analysis (DMA) was used to assess the viscoelastic properties, with particular focus on the acrylic sphere used in optical measurements. DMA tests were conducted using a dynamic mechanical analyzer from Anton Paar.

3.2 Theoretical and Numerical Framework

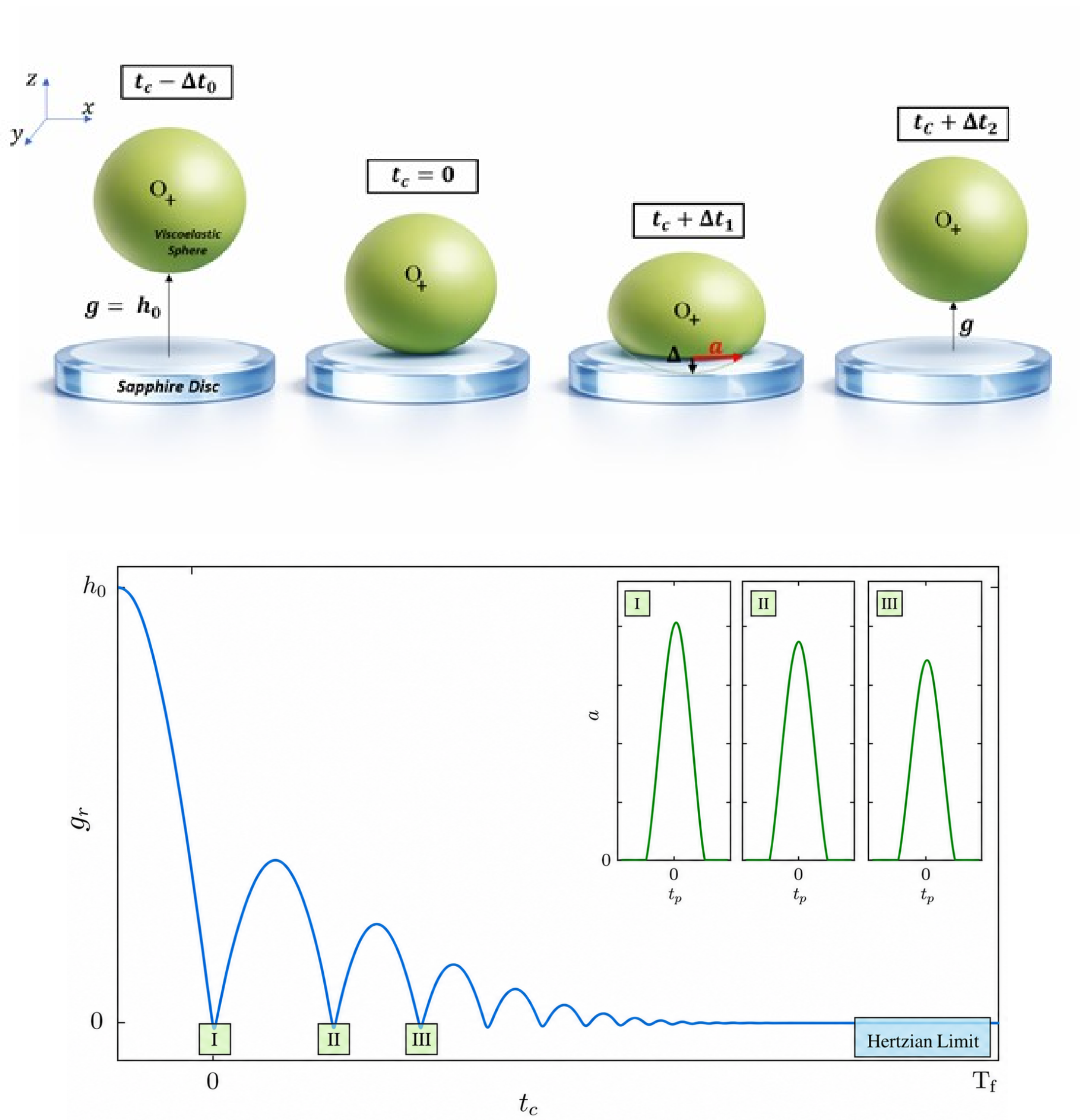

Figure 3.3: (a) The evolution of the reduced gap g_r as a function of time t_c for a given initial drop height h_0, where $t_c = 0$ corresponds to the first contact. (b) Qualitative illustration of the impact process.

Figure 3.3 schematically illustrates the impact process studied in this work and defines the key physical quantities for the analysis. A viscoelastic sphere with radius R is dropped from height h_0 onto a hard sapphire substrate, moving in the normal direction until contact occurs. The initial contact time, $t_c = 0$, serves as the reference point for both experimental and numerical analysis. The time evolution of the system is expressed in terms of the reduced gap g_r.

To formally define this quantity, we introduce the gap function g, which is generally expressed as $g(x,t) = g_0(x,t) - \Delta(t) + w(x,t)$ [152]. Here $\Delta(t)$ denotes the approximation of the rigid body, $g_0(x,t)$ denotes the initial seperation between the undeformed bodies, and $w(x,t)$ denotes the normal displacement of the surface in the radial coordinate x.

Accordingly, the reduced gap is defined as $g_r(x,t) = g(x,t) + \Delta(t) = g_0(x,t) + w(x,t)$.In the special case for the center point $x = 0$: $g_r(0,t) = g(0,t) + \Delta(t) = g_0(0,t) + w(0,t)$, where $g_0(0,t) = z_{\mathbf{O}}(t) - R$, and $z_{\mathbf{O}}(t)$ is the vertical coordinate of the center of mass of the sphere (see Figure 3.3).

The use of the reduced gap g_r enables a clear distinction between contact and separation scenarios. Specifically, contact occurs when $g_r \leq 0$, as the gap $g_r \leq 0$ and the rigid body approximation Δ assume non-positive values. In contrast, when the sphere is separated from the substrate, penetration - $\Delta = 0$ and the gap g assumes positive values. Unless specified otherwise, the sign of g_r refers to its value at the center point ($x = 0$).

Figure 3.3 shows that after the initial impact, the sphere rebounds with decreasing intensity and gradually approaches the Hertzian regime. The lower panel displays the key quantities used to analyze the contact area. The first three impact events are identified by the time variation of g_r. For each event, the variation of the contact radius a near its maximum is analyzed (see inset graph). To ensure systematic comparison, a local time variable t_p is defined at the moment when the contact radius reaches its maximum $t_p = 0$. This method enables comparison of different impact events regardless of their timing. The analysis focuses on the first three impacts only, as these events reflect the main features of the contact dynamics while minimizing the influence of weaker subsequent rebounds.

The behavior of a linear viscoelastic solid is characterized by a constitutive equation that relates deformation $\varepsilon(t)$ to the time derivative of the applied stress $\dot{\sigma}(t)$ [78].

$$\varepsilon(t) = \int_{-\infty}^{t} \frac{d\sigma(t')}{dt'} \, \mathcal{J}(t - t') \, dt'. \tag{3.1}$$

where $\mathcal{J}(t)$ is the creep compliance function. This function is related to the intrinsic material properties via

$$\mathcal{J}(t) = \frac{\mathcal{H}(t)}{\mathcal{E}_0} - \mathcal{H}(t) \int_0^{\infty} \mathcal{A}(\tau) \, \mathrm{e}^{-t/\tau} \, d\tau, \tag{3.2}$$

where $\mathcal{H}(t)$ is the Heaviside step function, E_0 is the long-term (rubber) modulus, and $\mathcal{A}(\tau)$ is the continuous creep spectrum over relaxation times. For numerical implementation, the spectrum is discretized and expressed as $\mathcal{A}(\tau) = \sum_{j=1}^{n} \mathcal{A}_j \, \delta(\tau - \tau_j)$ and the resulting creep function is $\mathcal{J}(t) = \frac{\mathcal{H}(t)}{\mathcal{E}_0} - \mathcal{H}(t) \sum_{j=1}^{n} \mathcal{A}_j \, \mathrm{e}^{-t/\tau_j}$. This approach enables the viscoelastic behavior of a material to be described as a sum of several characteristic relaxation mechanisms (Prony order), facilitating efficient application in numerical models.y in numerical models.

The normal surface displacement $w(x,t)$ induced by the applied stress field is computed using the convolution integral [39, 37, 38]

$$w(x,t) = \int_{-\infty}^{t}\int_{-\infty}^{\infty} \mathcal{J}(t-t')\,\mathcal{G}(x,x')\,\frac{\partial\sigma(x',t')}{\partial t'}\,dx'\,dt', \tag{3.3}$$

Here, $\mathcal{G}(x,x')$ represents the spatial Green's function. When the radial area is divided into N concentric rings of width λ, the Green's function that describes the displacement at point x_i due to a unit pressure applied in the k-th ring is expressed as follows:

$$\mathcal{G}(x_i,x_k) = \mathcal{U}\big(x_i, x_k + \tfrac{\lambda}{2}\big) - \mathcal{U}\big(x_i, x_k - \tfrac{\lambda}{2}\big)\,, \tag{3.4}$$

where $\mathcal{U}(x_i,x_k)$ is defined as [152, 153]

$$\mathcal{U}(x_i,x_k) = \frac{4(1-\nu^2)}{\pi}\begin{cases} x_k \mathrm{E}(x_i/x_k) & x_i \le x_k \\ x_i\left[\mathrm{E}(x_k/x_i) - (1-(x_k/x_i)^2)\mathrm{K}(x_k/x_i)\right] & x_i > x_k \end{cases} \tag{3.5}$$

with $\mathrm{K}(\cdot)$ and $\mathrm{E}(\cdot)$ denoting the complete elliptic integrals of the first and second kind, respectively.

Following the numerical approach proposed in Ref. [39], the discretized expression of the surface displacement at the i-th node and at time $t = n\Delta t$ can be written as

$$w(x_i,n\Delta t) - \Omega(x_i,n\Delta t) - \Gamma(x_i,n\Delta t) = \mathcal{J}(0)\sum_{k=1}^{N}\mathcal{G}(x_i,x_k)\,\sigma(x_k,n\Delta t), \tag{3.6}$$

where the history-dependent terms $\Omega(x_i,n\Delta t)$ and $\Gamma(x_i,n\Delta t)$ are defined as [39, 38, 154]

$$\Omega(x_i,n\Delta t) = \sum_{k=1}^{N}\mathcal{G}(x_i,x_k)\sum_{m=0}^{n-1}\mathcal{J}\big(\Delta t(n-m)\big)\,\Delta\sigma_k^m, \tag{3.7a}$$

$$\Gamma(x_i,n\Delta t) = -\sum_{k=1}^{N}\mathcal{G}(x_i,x_k)\,\mathcal{J}(0)\,\sigma(x_k,(n-1)\Delta t), \tag{3.7b}$$

where, $\Delta\sigma_k^m = \sigma(x_k,m\Delta t) - \sigma(x_k,(m-1)\Delta t)$.

Equation (3.6) can be recast in algebraic form as a linear system. Defining $w_c(x_i,n\Delta t) = w(x_i,n\Delta t) - \Omega(x_i,n\Delta t) - \Gamma(x_i,n\Delta t)$, one obtains

$$\{w_{c_i}\} = [\mathcal{K}_{ik}]\{\sigma_k\}, \tag{3.8}$$

where $\mathcal{K}_{ik}$ denotes the influence matrix. The contact problem is then solved iteratively according to the approach presented in [119]. In each iteration, elements with negative contact pressure are removed from the contact area, and areas with interpenetration are included in the contact zone. This process is continued until the contact area stabilizes.

A the rigid approach, denoted as $\Delta(t)$, must be established to guarantee the global equilibrium of the sphere. This condition is formulated as follows:

$$M\ddot{z}_{\mathbf{O}}(t) = F_n(\Delta(t)) - W, \tag{3.9}$$

Here, F_n denotes the normal contact force, which is determined by integrating the pressure distribution across the contact area, while W represents the total weight. The total mass of the system is defined as $M = m_s + m_h$, where $m_s = 5\,\mathrm{g}$ is the mass of the sphere and $m_h = 500\,\mathrm{g}$ is the mass of the holder (see Figure 3.1).

The experimental velocity was calculated from the displacement fields obtained by Digital Image Correlation (DIC). The vertical displacement $Y_{\mathrm{disp}}(t)$ of a selected representative point on the substrate (in pixels) was tracked over time and converted to millimeters using a calibrated conversion factor C:

$$Y_{\mathrm{disp},}(t) = Y_{\mathrm{disp}}(t) \times C \tag{3.10}$$

The instantaneous vertical velocity $v_{\mathrm{exp}}(t)$ was determined by numerically differentiating the displacement–time function. A central difference scheme was used for interior points, while forward and backward differences were used at the boundaries to improve accuracy:

$$v_{\mathrm{exp}}(t_i) = \frac{Y_{\mathrm{disp,mm}}(t_{i+1}) - Y_{\mathrm{disp,mm}}(t_{i-1})}{t_{i+1} - t_{i-1}} \quad \text{(Central Difference)} \tag{3.11}$$

$$v_{\mathrm{exp}}(t_1) = \frac{Y_{\mathrm{disp,mm}}(t_2) - Y_{\mathrm{disp,mm}}(t_1)}{t_2 - t_1} \quad \text{(Forward Difference)} \tag{3.12}$$

$$v_{\mathrm{exp}}(t_N) = \frac{Y_{\mathrm{disp,mm}}(t_N) - Y_{\mathrm{disp,mm}}(t_{N-1})}{t_N - t_{N-1}} \quad \text{(Backward Difference)} \tag{3.13}$$

As a result, the velocity obtained in units of was converted to and a moving average filter was applied to reduce the high-frequency noise generated by the numerical derivative:

$$v_{\mathrm{exp,ms}}(t) = \frac{\mathrm{smooth}(v_{\mathrm{exp}}(t), N)}{1000} \tag{3.14}$$

3.3 Results and discussion

3.3.1 Dynamic Mechanical Analysis of the Spheres

As described in Section 3.1, the viscoelastic properties of the materials used in the impact experiments, including Acrylic (PMMA), PEEK, Nylon, and PTFE, were characterized using Dynamic Mechanical Analysis (DMA). For each material, prismatic specimens with a cross section of 3 mm × 3 mm and a length of 20 mm were prepared. Frequency and temperature sweep tests were conducted to evaluate the linear viscoelastic behavior.

DMA tests were performed under torsional loading over the frequency range 0.1 to 10 Hz and the temperature was varied from −40°C to 120°C. This approach allowed the determination of the complex shear modulus $\mathcal{G}^*(\omega, T)$, which includes both the elastic and dissipative components of the material. The complex modulus consists of two parts: the storage modulus $\mathcal{G}'(\omega)$, which characterizes the energy storage, and the loss modulus $\mathcal{G}''(\omega)$, which is related to viscous dissipation.

The DMA results for each material were brought to the corresponding reference temperatures T_0 using the time-temperature superposition (TTS) principle (PEEK: 129.93°C, Nylon: 20.16°C, PMMA: 20.042°C, and PTFE: 20.031°C). The complex modulus master curves are shown in Figure 3.4, 3.5, 3.6, 3.7. Markers represent experimental data, while lines show the fitted viscoelastic model. The left axis displays $\mathcal{G}'(\omega)$, and the right axis displays $\mathcal{G}''(\omega)$.

The master curves clearly show the transition from the low-frequency rubbery regime to the high-frequency glassy regime; this reflects the decrease in the mobility of the polymer chains as the frequency increases. At the same time, the loss modulus α exhibits a characteristic peak behavior due to relaxation, which is related to the molecular segment dynamics and energy dissipation. The slip coefficients a_T, shown in the right panels of the Figure 3.4, 3.5, 3.6, 3.7, enable construction of the master curve across a wide frequency range according to the following relationship:

$$\mathcal{G}(\omega, T) = \mathcal{G}\big(a_T\, \omega,\, T_0\big). \tag{3.15}$$

The smooth variation of a_T with temperature indicates thermo-rheological consistency for all materials and confirms the validity of the TTS approach.

This DMA analysis reliably characterizes the frequency-dependent viscoelastic behavior of acrylic, PEEK, Nylon and PTFE materials and provides a solid basis for the correct analysis and prediction of their dynamic response under impact loading.

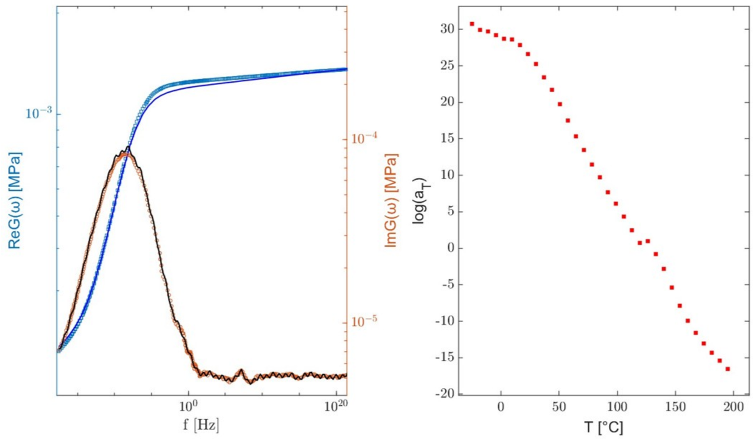

Figure 3.4: Viscoelastic modulus master curves obtained from DMA analysis for a PEEK sphere: the left panel shows the experimental data for the storage and loss moduli (blue circles Re $\mathcal{G}$, red circles Im $\mathcal{G}$ and the numerical fits (solid blue and black lines), respectively; the right panel presents the temperature-dependent slip factors a_T, with the reference temperature $T_0 = 129.93°$C.

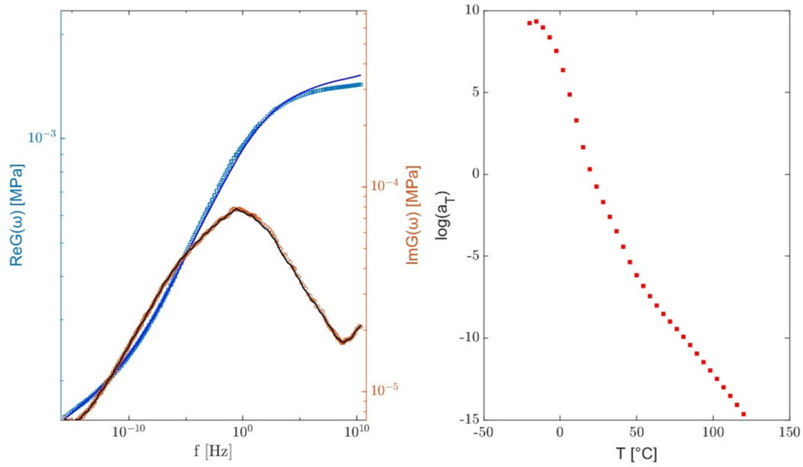

Figure 3.5: Viscoelastic modulus master curves obtained from DMA analysis for a Nylon sphere: the left panel shows the experimental data for the storage and loss moduli (blue circles Re $\mathcal{G}$, red circles Im $\mathcal{G}$ and the numerical fits (solid blue and black lines), respectively; the right panel presents the temperature-dependent slip factors a_T, with the reference temperature $T_0 = 20.16°$C.

3.3.2 Experimental Validation via Laser and High-Speed Imaging

The dynamic response of the impact system $h_0 = 7\,$mm was investigated at a controlled drop height, precisely set using a micrometer-based mechanism to ensure

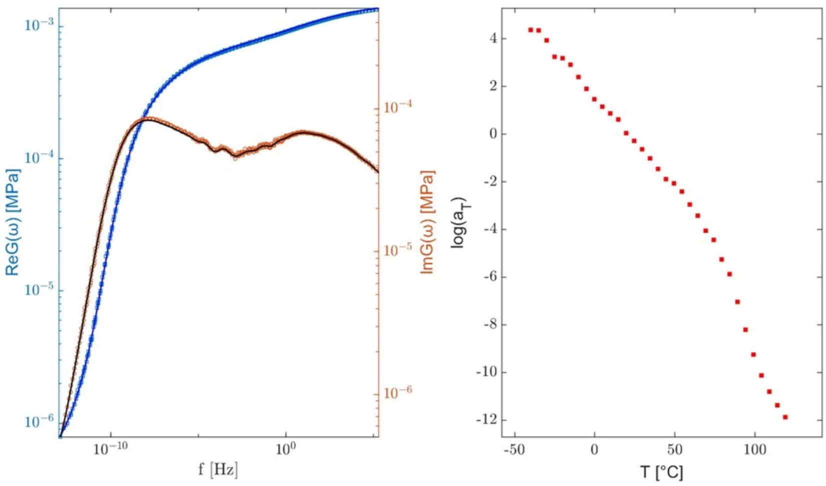

Figure 3.6: Viscoelastic modulus master curves obtained from DMA analysis for a Acrylic sphere: the left panel shows the experimental data for the storage and loss moduli (blue circles Re $\mathcal{G}$, red circles Im $\mathcal{G}$ and the numerical fits (solid blue and black lines), respectively; the right panel presents the temperature-dependent slip factors a_T, with the reference temperature $T_0 = 20.042°$C.

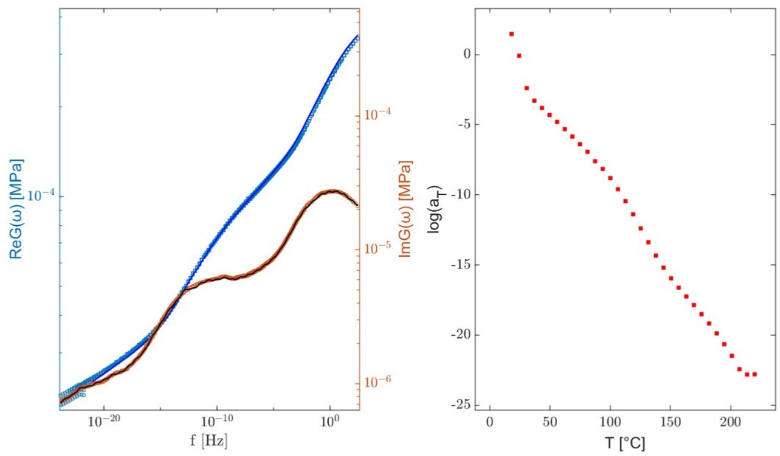

Figure 3.7: Viscoelastic modulus master curves obtained from DMA analysis for a PTFE sphere: the left panel shows the experimental data for the storage and loss moduli (blue circles Re $\mathcal{G}$, red circles Im $\mathcal{G}$ and the numerical fits (solid blue and black lines), respectively; the right panel presents the temperature-dependent slip factors a_T, with the reference temperature $T_0 = 20.031°$C.

experimental reproducibility. The displacement of the ball-holder system was independently measured using a Keyence laser displacement sensor and the Digital Image Correlation (DIC) method, as described in Section 3.1, together with high-speed imaging. This allowed direct comparison and validation of the measurement methods.

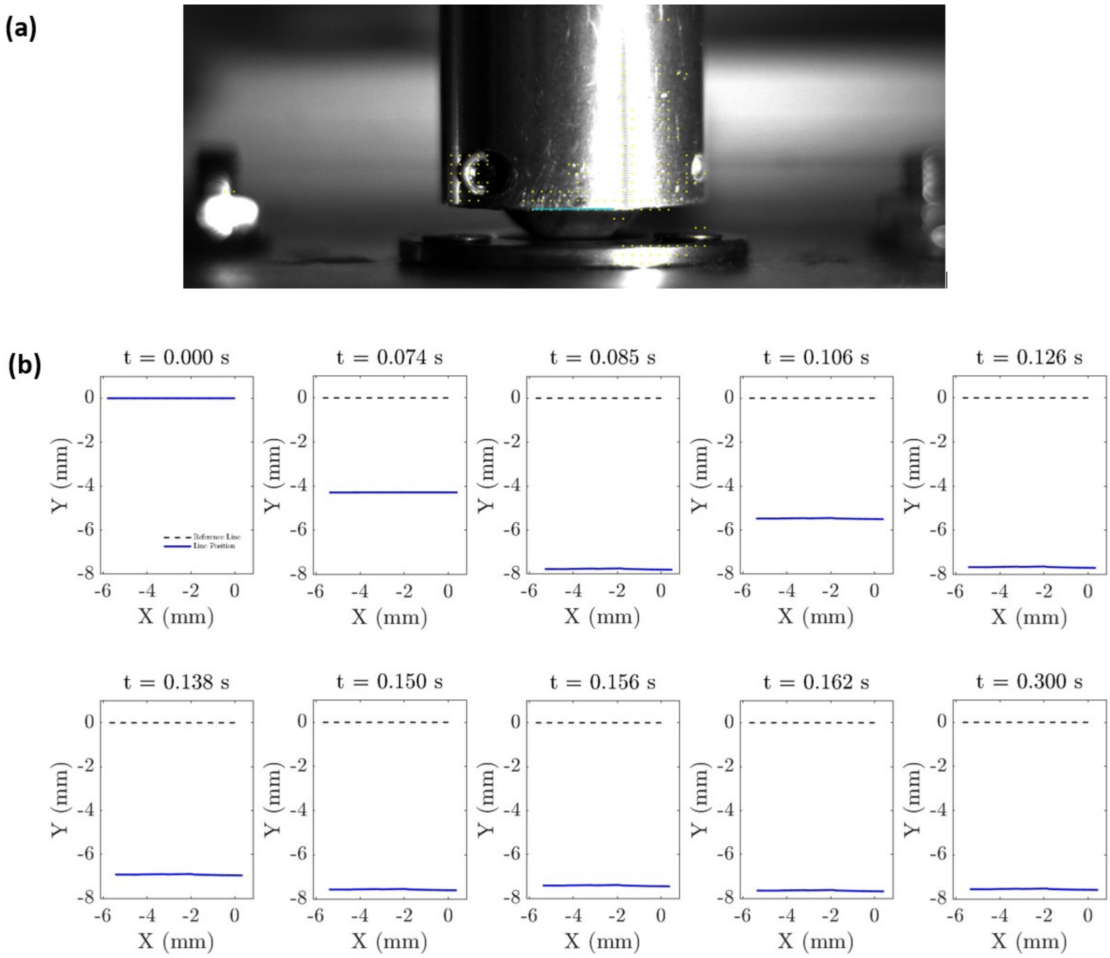

Figure 3.8: Deformation evolution of the PTFE ball impact on a sapphire disc. (a) DICe analysis of the PTFE ball holder showing the reference line (blue) selected on the subset of automatically detected points (yellow dots). (b) Time-lapse deformation of the reference line at selected times (0, 0.074, 0.085, 0.106, 0.126,3, 0.138, 0.149,6, 0.155,6, 0.161,8 s, and final time - 0.300 s). The line drops from a 7 mm height and progressively deforms upon impact, with subsequent rebounds visible. All coordinates are in mm (calibration: 1 pixel = 77.7 µm).

Figure 3.8 (b) shows the intermediate results obtained from the DIC analysis. As can be seen in Figure 3.8 (a)), a blue reference line was defined on the surface of the gripper and divided into several sub-areas (subsets), and the motion of these areas was tracked through the image sequence using correlation-based matching. The DIC algorithm calculates the displacement area by maximizing the correspondence of the grayscale distribution within each subset between successive frames, thus ensuring sub-pixel accuracy. The temporal displacement of the subsets captures the spatially distributed motion of the gripper during impact. Using this data, a representative subset was selected to construct a one-dimensional displacement–time profile. This profile was used to determine the global displacement response of the system (see Figure 3.8 (a)).

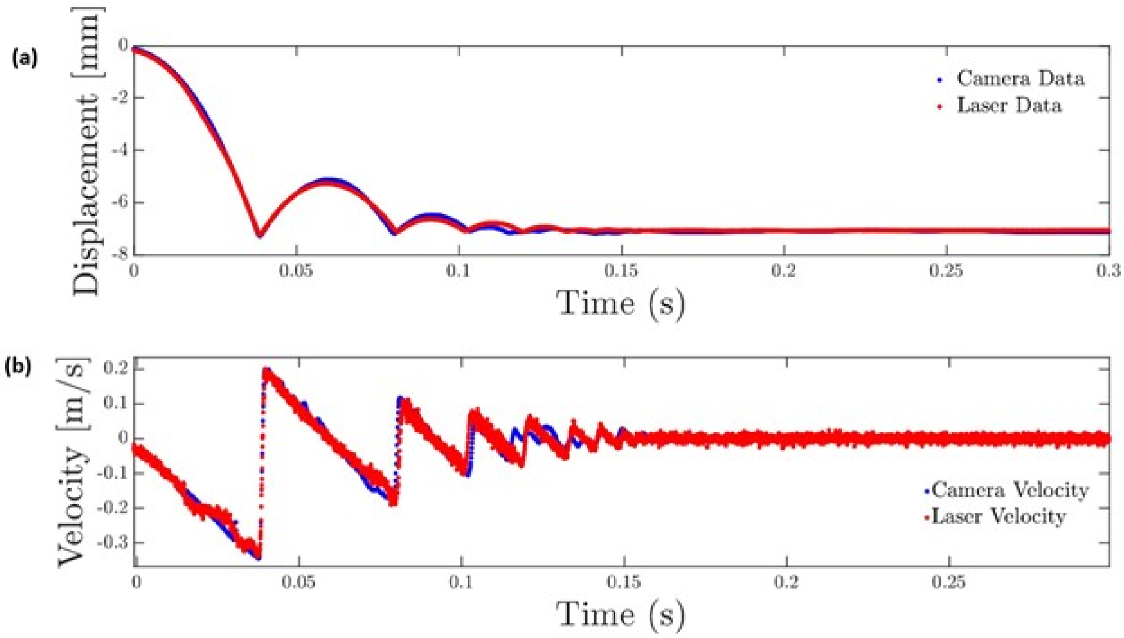

Figure 3.9: Time evolution of the ball drop response for a drop height of h = 7 mm, obtained from the high-speed Phantom Mini UX100 camera (blue markers) obtained from the DIC and from laser measurements (red markers). Panel (a) presents the experimental displacement histories of both tests, while panel (b) shows the corresponding velocities calculated from these data.

The displacement–time dependences obtained by the laser sensor and the DIC method are presented in Figure 3.9. A high level of agreement is observed between these two independent measurements throughout the experiment, confirming the reliability of the experimental setup and the calibration procedures. The initial contact between the PTFE sphere and the hard sapphire surface occurs at approximately $t \approx 0.04\,\mathrm{s}$ and is characterized by a sharp decrease in displacement. As a result of the first impact, the maximum indentation is approximately $-7\,\mathrm{mm}$, which is consistent with the predetermined drop height on micrometer.

After the initial impact, the system shows a series of jumps with decreasing amplitude. This pattern reflects the dissipative nature of the contact, primarily caused by surface energy losses from the viscoelastic response of the PTFE. In the next stage, the motion switches to a damped oscillation regime and the amplitude decreases significantly. Finally, at approximately $t \geq 0.15\,\mathrm{s}$ the system approaches

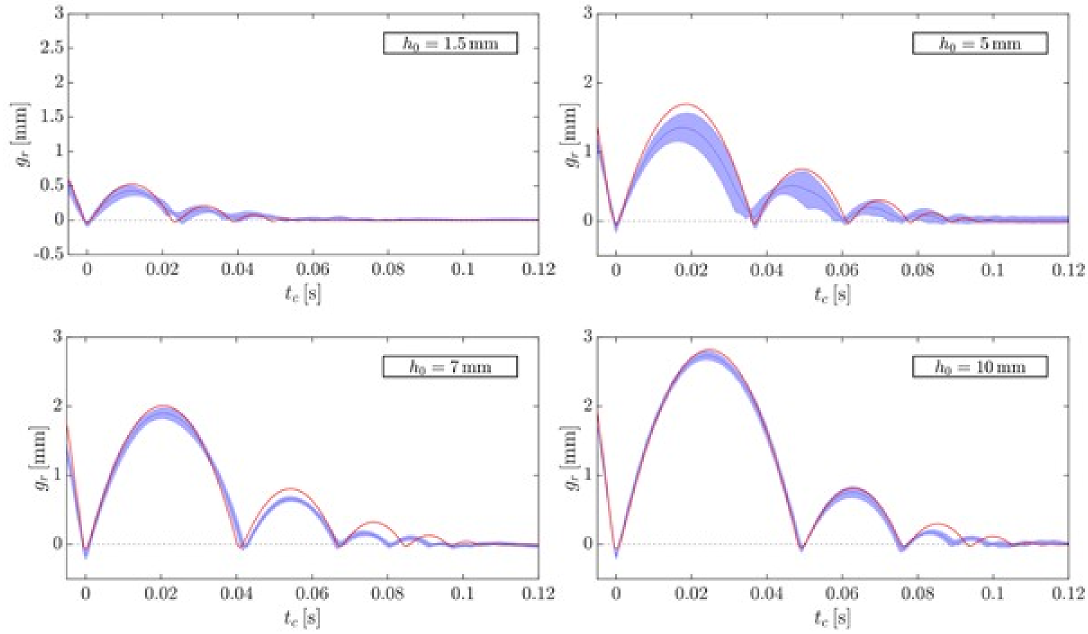

Figure 3.10: The impact response of an Acrylic sphere dropped from heights $h_0 = 1.5$ mm, 5 mm, 7 mm, and 10 mm. shows the variation of the vertical displacement h as a function of time t. The experimental data with uncertainty is represented by the blue region, while the red line shows the numerical prediction of the gap evolution.

quasi-static equilibrium and the displacement stabilizes around -7.1 mm.

Velocity–time profiles, 3.9 (b), were calculated from the experimental displacement data in Section 3.2 and further confirmed the results. These profiles show sharp changes during each impact: the largest velocity is observed at the first bounce, and subsequent peaks gradually decrease due to energy losses. Velocity plots show the impact dynamics—in particular, the timing and intensity of the bounces—more clearly than displacement data.

3.3.3 Effect of Drop Height on Impact Response

Once the material properties were calibrated in the numerical model, impact tests were performed to evaluate the global motion of the sphere and the development of contact during impact. Figures 3.10, 3.11, and 3.12 compare experimental results with numerical predictions for vertical displacement Δ mm of Acrylic, Nylon, and PEEK spheres. For each tested material, the tests were performed at four initial heights: ($h_0 = 1.5$ mm), (5 mm), (7 mm), and (10 mm). Five repetitions of experimental tests were performed for each material to increase statistical reliability.

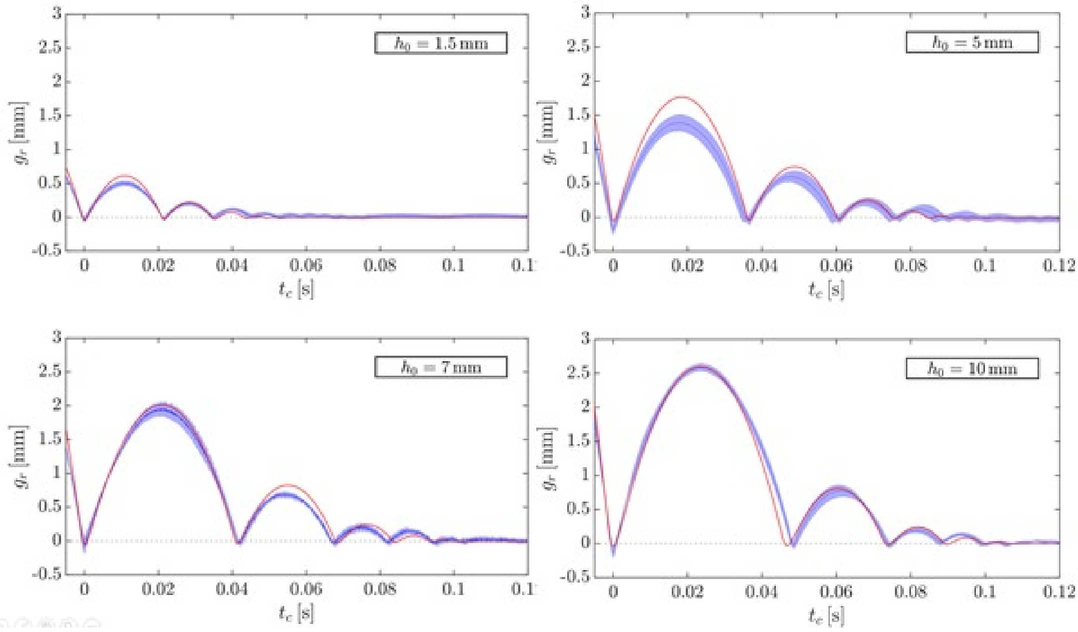

Figure 3.11: The impact response of an Nylon sphere dropped from heights $h_0 = 1.5\,\mathrm{mm}$, $5\,\mathrm{mm}$, $7\,\mathrm{mm}$, and $10\,\mathrm{mm}$. shows the variation of the vertical displacement h as a function of time t. The experimental data with uncertainty is represented by the blue region, while the red line shows the numerical prediction of the gap evolution.

In all cases, the experimental signals are shifted along the time axis to correspond to the initial contact moment ($t_c = 0$) between the sphere and the sapphire surface. This allows for consistent comparison of the experimental and numerical results with respect to the same time reference. The vertical displacement (Δ) is plotted as a function of time; the blue shaded areas represent the experimental data and their uncertainty interval, while the red lines represent the numerical predictions. The green areas highlight the penetration phase, which is presented in more detail in the additional zoomed-in plots.

The narrow experimental error intervals across all materials and drop heights indicate high repeatability and reliability of the measurements. This confirms that the observed agreement is due to the accuracy of the model and not to measurement errors. The close agreement between the blue bands and the red curves demonstrates that the numerical model describes the impact response with high accuracy.

The results show that as the drop height increases, the deformation increases and the bounce dynamics become more pronounced, while the damping of successive bounces reflects the intrinsic viscoelastic dissipation property of the material. Although the acrylic, nylon, and PEEK materials have different material properties, the numerical model successfully describes the main stages of the impact response in all cases—the initial compression, the bounce sequence, and the damping of oscillations. This indicates that the model is reliable and generalizable to a variety

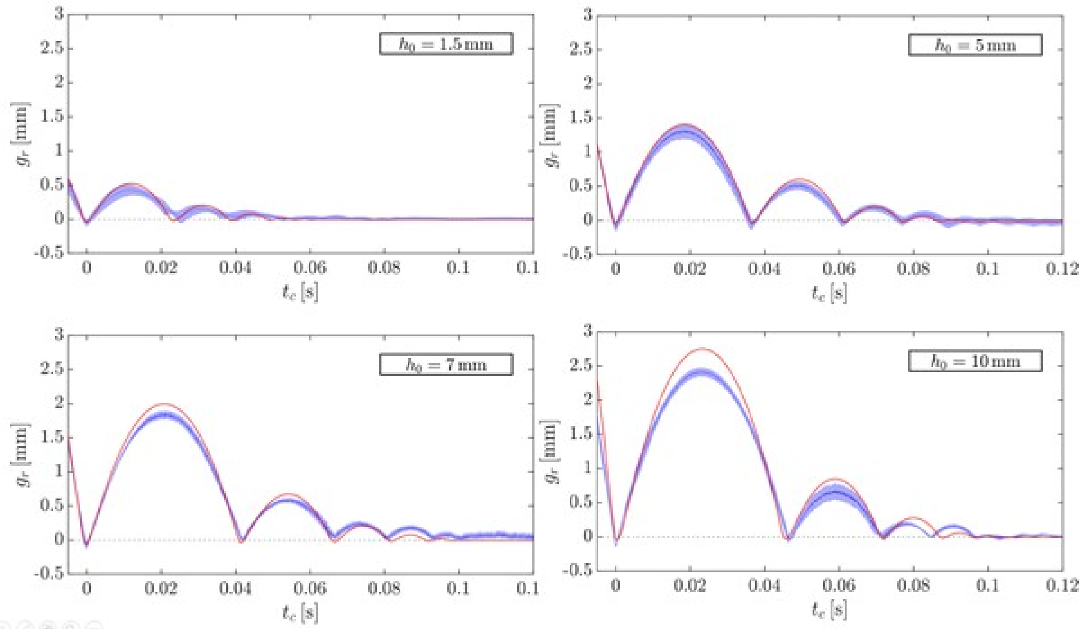

Figure 3.12: The impact response of an PEEK sphere dropped from heights $h_0 = 1.5\,\mathrm{mm}$, $5\,\mathrm{mm}$, $7\,\mathrm{mm}$, and $10\,\mathrm{mm}$. shows the variation of the vertical displacement h as a function of time t. The experimental data with uncertainty is represented by the blue region, while the red line shows the numerical prediction of the gap evolution.

of viscoelastic polymers.

A partial deviation from the general trend is observed for the case $h_0 = 5\,\mathrm{mm}$; here, the experimental scatter is slightly wide for acrylic and, to some extent, for nylon. This indicates that this impact condition is more sensitive to secondary effects that are not taken into account in the model—for example, small alignment errors, tangential motion components, plate vibration (see Appendix B), or local dynamic responses of the sapphire substrate. However, the scatter for PEEK is smaller, indicating that it responds more stably under the same conditions.

Despite minor differences, the numerical model accurately reproduces the overall change in reduced gap (g_r) for all three materials and drop heights with high accuracy. In particular, the initial compression stage, successive bounces, and gradual damping of oscillations are described with very good agreement. The gradual decrease in the bounce amplitude is a clear indication of viscoelastic dissipation, and this behavior is observed in the same way in Acrylic, Nylon and PEEK materials. During each impact, part of the energy is elastically stored and subsequently recovered, while the other part is irreversibly dissipated within the material. As a result, the bounces gradually weaken, and this trend is successfully reflected by the numerical model. This indicates that the applied viscoelastic model correctly describes the main dissipative mechanisms.

The agreement obtained is particularly striking because the numerical model used is quite simple: only the normal motion of the sphere is taken into account, and tangential effects and possible vibrations of the sapphire substrate are not included. The presence of vibrations was confirmed by additional experimental tests, see Appendix B. Nevertheless, the results show that for the selected drop heights and materials, the impact behavior is mainly determined by the normal contact dynamics. This result is confirmed in the same way for materials with different viscoelastic properties, such as Acrylic, Nylon and PEEK, and demonstrates the validity of the model as well as its wide application possibilities.

Due to its transparency, the acrylic sphere represents the only material among those investigated for which the evolution of the contact region can be directly visualized during impact through optical measurements. This unique feature allows for a simultaneous and reliable observation of both the global motion and the local contact behaviour. For this reason, the following analysis focuses on the acrylic sphere, for which a direct comparison between displacement measurements and contact radius evolution can be established.

Figure 3.10 presents the time evolution of the impact response of an acrylic sphere falling from $h_0 = 1.5\,\mathrm{mm}$ onto a sapphire substrate. The figure displays both global kinematic data and local contact data: the blue curve represents vertical displacement measured by a Keyence laser displacement sensor, while the green markers indicate contact radius obtained from high-speed images. This visualization highlights the relationship between the macroscopic movement of the sphere and the microscopic development of the contact interface. It should be noted that the laser and camera measurements were performed at different times. In addition to 1.5 mm, the results for 5 mm, 7 mm, and 10 mm drop heights are provided in Appendix C.

The results in Figure 3.13can be clearly divided into three distinct phases. The first phase is the *bouncing phase*, where a series of discrete impacts occur. During this period, the displacement signal shows strong oscillations, and the contact radius is characterized by sharp peaks corresponding to each impact. Interestingly, these peaks coincide with the minima of the displacement signal — that is, each impact event measured by the laser corresponds to a specific optically observed contact state.

Intervals I, II, and III highlighted in the Figure 3.13 represent the first three impacts, which are most significant for contact development. These events are also depicted in Figure 3.14, where experimental contact area profiles are compared with numerical results (solid red circles). This comparison establishes a direct relationship between the time-domain response and the geometrical evolution of the contact region. It is particularly striking that the decrease in contact area from the first to the third impact corresponds precisely to the reduction in contact radius peaks in the time signal.

As time progresses, the system enters the next phase. This phase is called the *vibration phase*, and in this phase, damped oscillations around the equilibrium

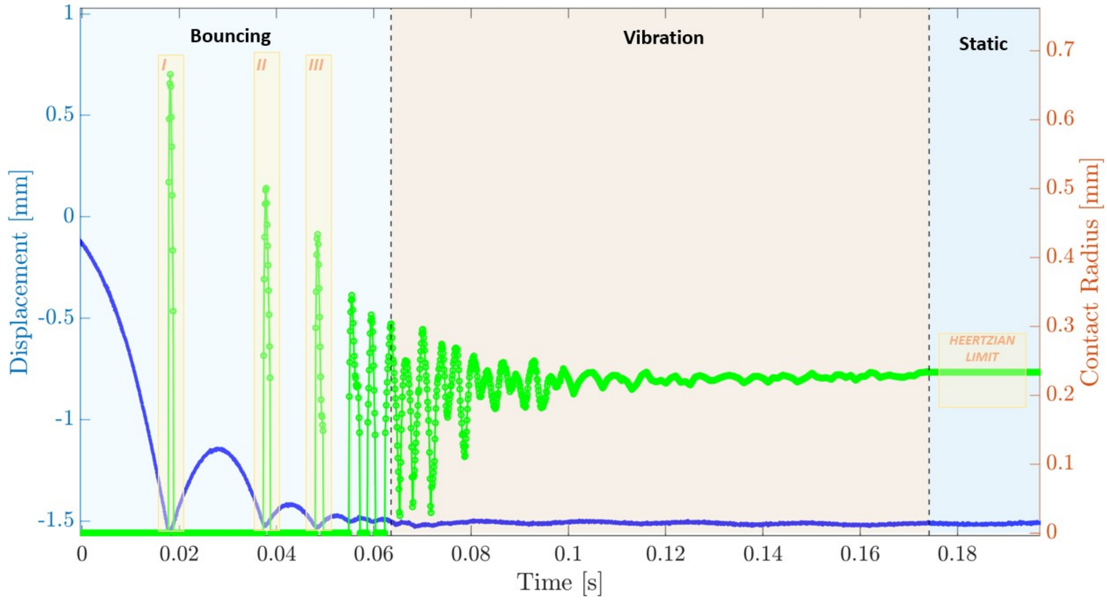

Figure 3.13: Temporal evolution of the impact response of an acrylic sphere released from an initial height $h_0 = 1.5\,\mathrm{mm}$ onto a sapphire substrate. The blue markers correspond to experimentally measured sphere displacement acquired using a Keyence laser sensor, while the green markers represent the contact radius evolution obtained from high-speed camera imaging. The response is segmented into three distinct regimes: (a) a bouncing phase characterized by successive impacts, (b) a vibration phase exhibiting damped oscillations, and (c) a static phase where a steady contact condition is attained. The highlighted intervals I-II-III identify representative impact events selected for detailed contact analysis, while the shaded region indicates the Hertzian contact limit (see Figure 3.14).

position can be observed. In this regime, the contact begins to transition to a continuous state, while the contact radius exhibits smaller amplitude variations. This indicates that energy is gradually lost due to the viscoelastic properties of the material.

Finally, the system enters the final *static phase*. At this point, both the displacement and the contact radius stabilize, which indicates that the sphere has come to a complete standstill.

The shaded area in Figure 3.13 shows the Hertz contact theory limit corresponding to the equilibrium contact radius under quasi-static conditions. The approach of the contact radius to this value is consistent with the final contact configuration observed in Figure 3.14 and confirms that the contact area has a stable shape according to Hertz theory. The transition from discrete impacts to continuous contact and then to static equilibrium shows that the model correctly describes both transient dynamics and long-term behavior. The strong correspondence between displacement and contact radius, as well as the overlap of temporal and spatial

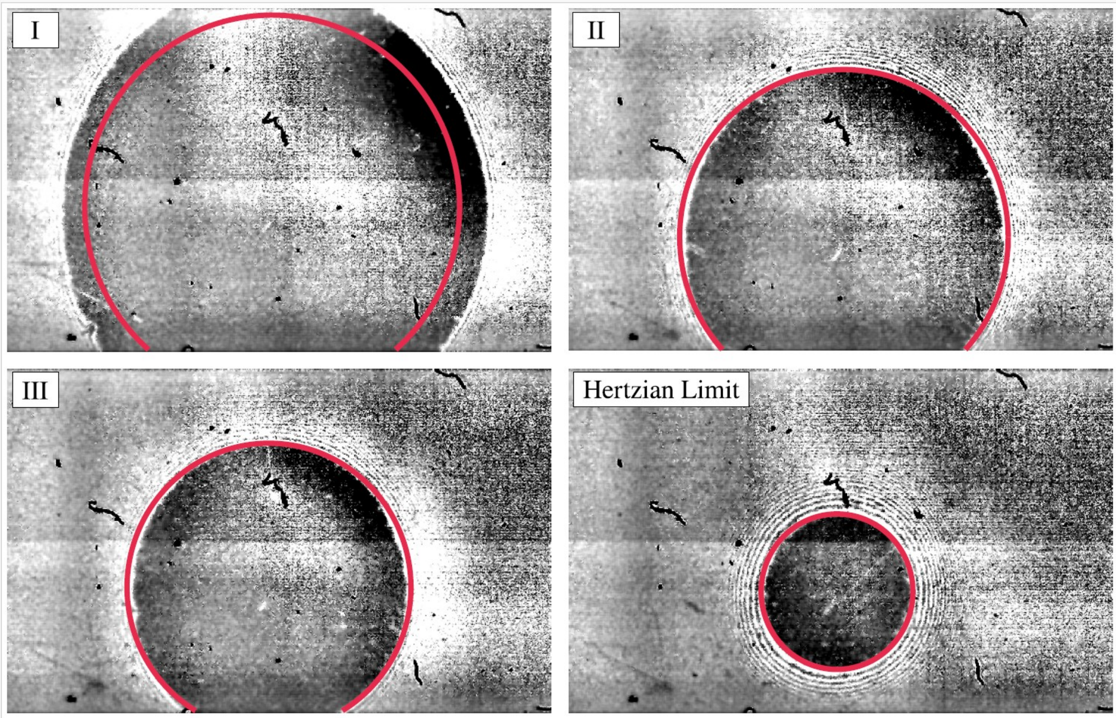

Figure 3.14: The numerically predicted contact areas (red lines) are compared with those obtained experimentally from high-speed cameras. The comparison is based on the first three maximum impacts and the static Hertzian limit at the end, with an initial drop height of $h_0 = 1.5\,\text{mm}$, as shown in Figure 3.13. During calibration, 1 *pixel* was measured as =2.17mm.

observations, demonstrate the validity of this approach and highlight the fundamental connection between global impact dynamics and local contact mechanics in viscoelastic materials.

Figure 3.15 further supports this interpretation. The experimental test shows the time-dependent variation of the contact radius during the first three impacts for all release heights ((a) $h_0 = 1.5\,\text{mm}$, (b) $h_0 = 5\,\text{mm}$, (c) $h_0 = 7\,\text{mm}$, and (d) $h_0 = 10\,\text{mm}$) and is compared with numerical predictions. In the graph, blue square markers indicate the experimental contact radius obtained by image processing, while red solid lines represent the predictions of the numerical model.

For each case, the comparison is made by applying a local time variable t_p; this variable is chosen so that $t_p = 0$ corresponds to the moment when the contact radius is maximum during the considered impact. Thanks to this normalization, the time evolution of the contact radius around each peak is analyzed in a more consistent and comparable way, regardless of the absolute time of impact. Thus, it is possible to directly compare different impact events within a single time frame, which allows a clearer assessment of the agreement between experimental results and numerical simulations.

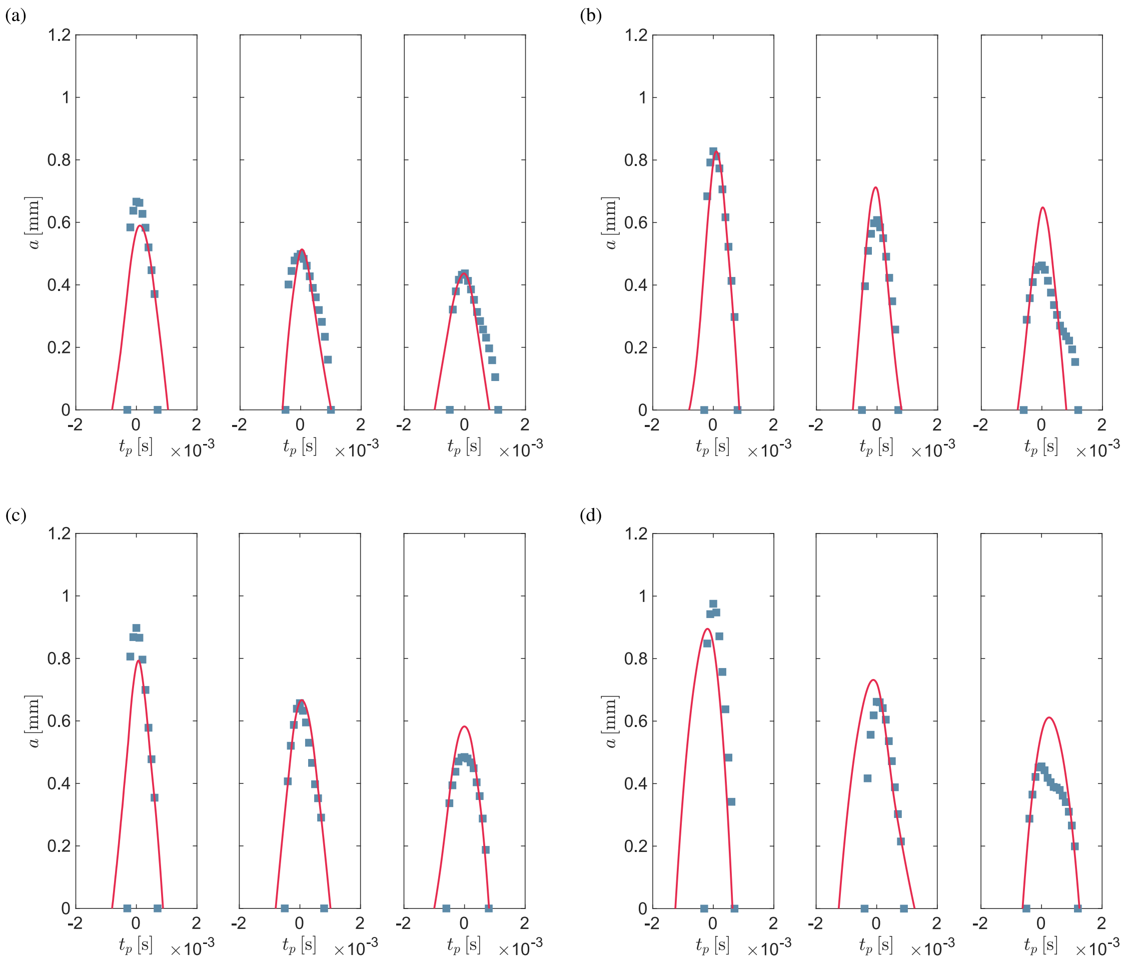

Figure 3.15: The contact radius a versus time is plotted for different drop heights ($h_0 = 1.5\,\mathrm{mm}$ (a), $h_0 = 5\,\mathrm{mm}$ (b), $h_0 = 7\,\mathrm{mm}$ (c), and $h_0 = 10\,\mathrm{mm}$ (d)). The numerical results (red lines) are compared with the experimental data (blue squares), both data sets being transformed so that the maximum contact radius occurs at $t_p = 0$.

The numerical model reproduces the time evolution of the contact radius for the first three impacts at all drop heights with high accuracy. It particularly accurately reflects the level of the maximum contact radius, the rapid increase during the loading phase, and the decrease during unloading. This agreement is notable given that each impact occurs within a very short interval, approximately 10^{-3} s. Accurate modeling of these fast dynamics requires fine discretization; here, the spatial resolution is $\lambda = 4 \times 10^{-5}$ m and a time step of $\Delta t = 2 \times 10^{-4}$ s. This strong agreement demonstrates that the physical foundations of the model are sound and that the numerical integration scheme is stable and reliable for tracking contact development over short time scales.

For the smallest drop height $h_0 = 1.5\,\mathrm{mm}$, the first peak is well reproduced, but a slight difference remains in the maximum value — the experimental results indicate that the contact radius is slightly larger. However, for the second and third impacts, the agreement improves further, and the model accurately reflects the gradual decrease in peak amplitude due to viscoelastic dissipation. These results also align with the previously discussed development of the contact area in Figure 3.14.

A similar agreement is observed for the intermediate drop heights $h_0 = 5\,\mathrm{mm}$ and $h_0 = 7\,\mathrm{mm}$. The experimental data closely follow the numerical curves, with only small deviations visible during the discharge phase. These differences can be mainly explained by uncertainties in the definition of the contact boundary in the image processing or by second-order effects not taken into account in the model.

At the highest height $h_0 = 10\,\mathrm{mm}$, the first impact produces a larger contact radius, which is consistent with the high impact energy. The model also describes both the magnitude and the overall shape of the peaks well. However, for subsequent impacts, especially during the discharge phase, small asymmetries in the experimental curves become more noticeable. This can be attributed to the increased role of tangential motion, small alignment errors, or local dynamic effects at high energy impacts—factors that are not included in the model. The agreement observed across all drop heights is particularly significant. Despite the simplicity of the model, the fact that it accurately describes such fast contact events demonstrates its validity and confirms that it successfully captures the main features of viscoelastic impact behavior.

Additional experiments were conducted to assess the effect of temperature on the impact behavior of the acrylic sphere. The sphere was locally heated with a heat gun, and the contact process was recorded from below with a Phantom Mini UX100 high-speed camera, Figure 3.2. The temperature of the contact area was monitored using an infrared thermometer, ensuring that the surface was maintained at approximately 39°C. The experiments were conducted for $h_0 = 10\,\mathrm{mm}$, which allowed both maintaining the distance from the heat source and clearly observing the impact dynamics.

Figure 3.16 presents the experimental results: changes in contact radius over time and corresponding contact images for room temperature (blue markers) and the heated state (red markers). The first three impacts demonstrate that the contact radius increases consistently at all stages as temperature increases. This is due to the temperature-dependent viscoelastic properties of the material — as the temperature increases, the material softens and deforms more under the same load. Consequently, the contact area expands, as shown in the images.

At the same time, the development of the contact radius with time in the heated case occurs somewhat earlier (shifts to the left). This indicates that the contact is formed more quickly and is explained by the reduced stiffness of the material. The effect is especially noticeable in the initial stage of the impact, since the maximum contact radius is reached earlier.

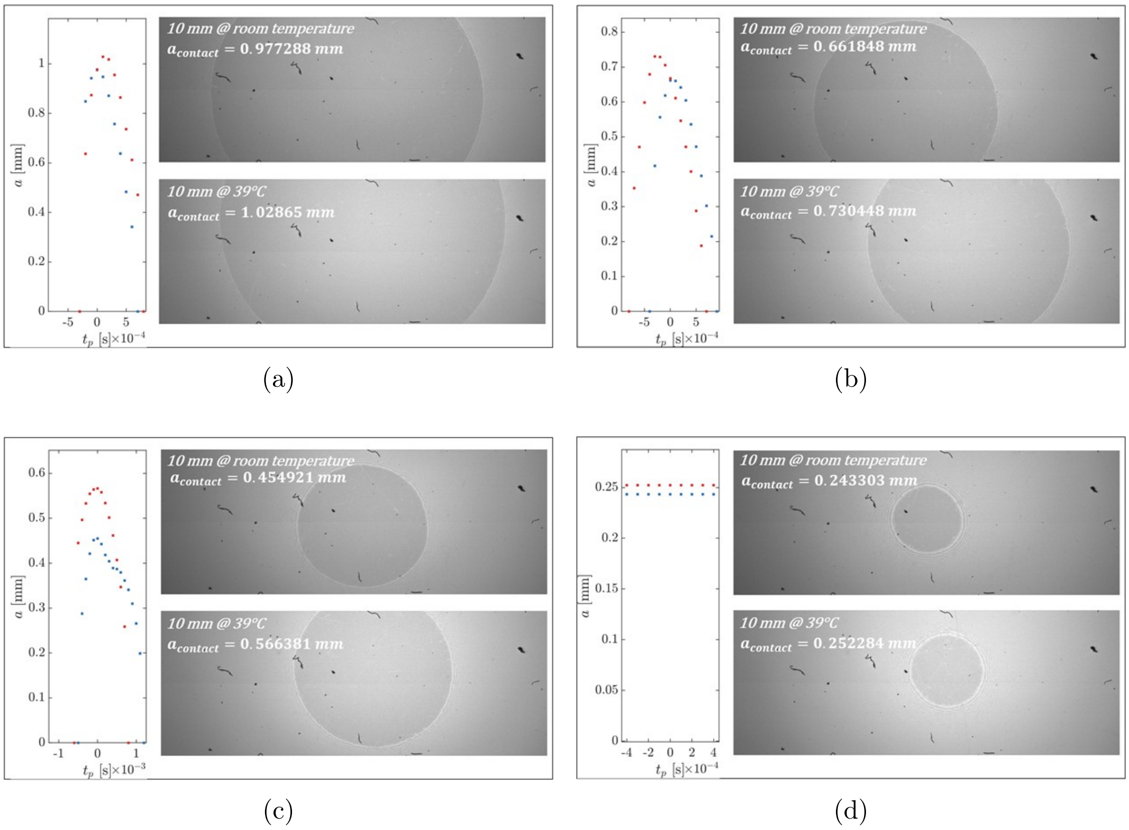

Figure 3.16: Experimental comparison of the evolution of the contact radius for an acrylic sphere dropped from 10 mm at two different thermal conditions: at room temperature (blue squares) and heated to 39°C (red squares). Panels (a)–(c) show the first three maximum impacts at each height, while (d) presents the quasi-static Hertz limit. Each plot shows the contact radius a and the shifted contact time t_p, together with corresponding high-speed images of the contact area.

A similar trend appears in the quasi-static case, within the Hertz contact theory limit: the heated sphere forms a larger contact radius even at equilibrium. This indicates that temperature effect is not limited to the dynamic phase, but affects contact mechanics beyond the dynamic phase. Observing this behavior in both dynamic and static cases confirms the strong influence of temperature on the viscoelastic response of acrylic.

In addition to the increased contact area, the contact radius develops earlier when heated, indicating faster contact formation during impact. This results from reduced material stiffness and enhanced viscous response at higher temperatures. The effect is most pronounced at the start of impact, as the maximum contact radius is reached more quickly.

The same trend is preserved in the quasi-static case — in the Hertz contact theory limit shown in panel (d). Even in the equilibrium case, the heated sphere shows a larger contact radius than at room temperature. This confirms that the temperature effect is not limited to the dynamic phase, but affects the contact mechanics in general. The consistent observation of this behavior in the dynamic and static cases clearly highlights the strong influence of temperature on the viscoelastic response of acrylic.

3.3.4 Static Loading Tests

Another experiment involved applying step loading to a PTFE sphere. The development of the contact response during the stepwise loading is shown in Figure 3.17 (a), where laser displacement measurements are compared with theoretical Hertz contact theory predictions.

The normal load was increased in stages: first 0.5 kg was applied at $t = 0$ min, and then the load was gradually increased to 2.5 kg at $t = 2.55$ min, 3.5 kg at $t = 18.20$ min, 4.5 kg at $t = 33.10$ min, and 5.5 kg at $t = 47.55$ min. This loading method enables observation of both the immediate elastic response and the time-dependent viscoelastic behavior at each stage.

The experimental displacement data were obtained with a laser-measuring system at a time resolution of 5 seconds. Due to the high sensitivity of the sensor, some fluctuations are visible in the raw data; this is mainly due to measurement noise, surface irregularities and environmental effects. To reduce this dispersion and to see the underlying physical trend more clearly, a moving average filter was applied, resulting in smoother and more reliable curves. Thus, the smoothed results show the overall mechanical response, while the raw data reflect the natural variation of the measurements.

The contact radius increases consistently with increasing load, as expected from classical contact mechanics. In addition, a time-dependent behavior is also clearly visible at each loading stage: immediately after the load is applied, the system goes through a short transient phase and then gradually approaches a quasi-steady state. This is a consequence of the viscoelastic creep characteristic of PTFE, under continuous loading, the deformation continues to increase with time due to internal structural changes.

In contrast, Hertz contact theory provides an instantaneous, time-independent contact response for each load. Therefore, the theoretical curves appear as stepwise, constant values, which reflect the assumption of perfectly elastic behaviour. Although the model correctly shows an overall increase in contact radius with increasing load, it does not account for the transient development observed in the experiment. For this reason, the differences are most noticeable immediately after the application of the load - at that moment, the experimental contact radius is smaller because the deformation has not yet fully developed.

Over time, however, the experimental contact radius increases and approaches a constant value, as a result of which the theoretical and experimental results

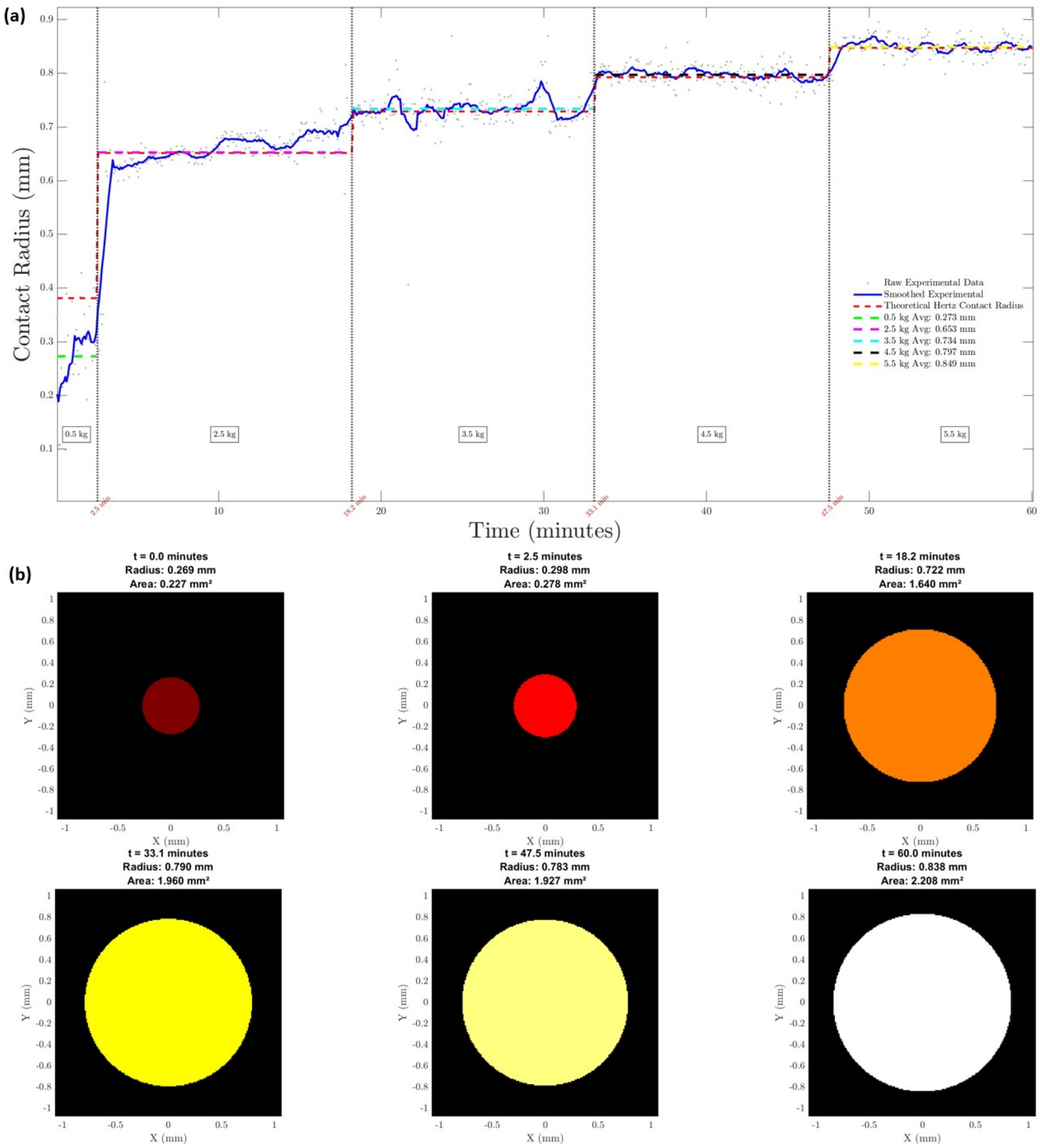

Figure 3.17: (a) Comparative plot of experimental and theoretical contact area evolution under stepwise loading for a PTFE ball on a sapphire surface: gray dots show raw data from the laser, blue solid curve is the smoothed response of the raw data, and red dashed line represents the Hertz prediction; horizontal dashed lines show the average contact radius at each load (0.5–5.5 kg), and vertical dashed lines show the applied load changes. (b) Evolution of theoretical contact area under stepwise loading.

converge. This indicates that the system has reached an equilibrium state that can be approximately described by elastic theory in the long run. However, the fact that certain differences remain clearly reveals the limitations of the Hertz model for viscoelastic materials.

Experimental results averaged over each load level show a similar growth trend in contact radius compared to theoretical predictions, but differences remain, especially at low loads. This is explained by the fact that both viscoelastic effects and measurement noise are more pronounced. In addition, corrections for laser angle and the geometric relationship used to convert displacement to contact radius ($a = \sqrt{R\delta}$) can introduce further variability.

The theoretical contact area development given in the lower part of Figure 3.17 presents an idealized picture: here the contact area is assumed to form immediately at each load level, to be constant over time, and to be perfectly circular. The experimental results show the opposite — the contact area gradually expands over time, confirming the existence of time-dependent deformation mechanisms.

Conclusions

This thesis is based on the study of the systematic investigation of viscoelastic materials under various contact loadings. This research combines experimental measurements, numerical modeling and analytical approaches under one umbrella, with a particular focus on indentation and impact processes. By considering quasi-static and dynamic regimes together, a unified and physically consistent framework is established to explain the deformation, stress distribution, contact development and energy dissipation mechanisms.

In Chapter 2, the mechanical behavior of NBR, a viscoelastic material, under indentation loading is investigated using a combination of experimental, numerical and analytical approaches and at the same time the development and validation of a numerical framework that can accurately predict the indentation behavior of materials. A specially designed periodic indenter was used for this purpose. Experimental analyses were performed on an NBR sample in a Biomomentum MACH-1 device using the same indenter. The obtained results were used as reference data for the verification of Boundary Element Method (BEM) simulations and an additional analytical approach developed to estimate the energy dissipation during cyclic indentation. The research is aimed at understanding the time-dependent response under both static and dynamic conditions. This type of research is considered to be of great practical importance. It is widely used in fields such as the design of viscoelastic dampers, as well as in biomechanics, in the mechanical characterization of soft materials and biological tissues using indentation-based methods. Because the indentation method is considered the best alternative to typical DMA analysis, and the use of this method is characterized by its advantages such as fast and reliable results, no sample cutting, and preservation of material integrity due to factors such as high temperature.

The stress relaxation experiments revealed typical viscoelastic behavior. Thus, a rapid increase in the response is observed during the initial loading, followed by a gradual decrease in the force due to the redistribution of stress within the polymer network, and after a certain time, the steady-state regime is reached. These experimental results were reproduced with high accuracy by the numerical model, which successfully described both the initial elastic response and the subsequent relaxation towards a stable plateau. The system showed strong agreement with the experimental results.

In order to further analyze the dynamic response, harmonic indentation tests were performed in addition to stress relaxation. The obtained simulation and experimental results showed good agreement at different frequency and amplitude conditions. At the same time, the results successfully recovered the hysteresis force–displacement cycles characterizing the energy dissipation and damping capacity. Both the accurate numerical calculations and the analytical formulation showed agreement with the experimental results in the evaluation of the dissipated work, which confirms that the analytical approach is an effective tool for simple and reliable evaluation of energy losses in cyclic viscoelastic contact problems.

In Chapter 3, the focus is on the dynamic response of viscoelastic materials under impact loading. For this purpose, a special experimental setup was developed to analyze the normal impact of spheres made of various materials such as Acrylic, PTFE, Nylon, PEEK on a hard sapphire substrate. The setup combined an electromagnetic release mechanism, a micrometric height adjustment, a laser displacement sensor, and a high-speed imaging system in the same setup, allowing for accurate and repeatable measurements of both global motion and local contact area development. This approach is considered an important advance in terms of simultaneously verifying kinematic and contact-level predictions.

The process line was simulated using a numerical model based on viscoelastic contact mechanics and implemented with the Boundary Element Method (BEM). Despite simplifying assumptions such as considering only normal motion and ignoring tangential effects and structural vibrations, the model showed high agreement with experimental results at different drop heights. In particular, the development of the reduced gap, the sequence of the jump, the damping of the motion due to viscoelastic dissipation, the spatial variation of the contact area, the temperature variation of the contact area, and the change of the contact in the static state were all accurately reproduced.

The analysis of the initial impacts showed that the main mechanisms—i.e., inertia, contact mechanics, and the time-dependent behavior of the material—are successfully described by the model. The reduction of the jump amplitude and contact area is correctly associated with the internal energy dissipation. The differences observed in the later stages are explained by the neglected secondary effects such as tangential motion, small alignment errors, and vibrations. This both confirms the robustness of the model and indicates directions for future improvement. It should be noted that a transparent acrylic sphere was used to study the contact area, allowing the contact to be seen.

Together with Chapter 2, these results show that viscoelastic contact problems from indentation to impact can be effectively analyzed with relatively simple and physically consistent models when supported by high-quality experimental data. The strong agreement obtained between experimental, numerical, and analytical approaches confirms the validity and universality of these methods.

In a broader context, the thesis highlights the important role of memory effects and time-dependent behavior in viscoelastic mechanics. Relating measurable quantities such as indentation depth, contact area, dissipated energy, and rebound dynamics to the intrinsic properties of the material provides a deeper understanding of the different loading regimes and time scales.

However, certain limitations still remain in the study. First, the constitutive description is restricted to linear viscoelasticity: stress is assumed to depend linearly on the deformation history through the Boltzmann superposition principle. This assumption is well justified for the small-strain, low-to-moderate strain-rate regimes considered here, but it is not expected to hold for the large local strains and strain rates that can occur during high-velocity impact or for materials exhibiting pronounced non-linear or strain-stiffening behaviour; extending the framework to such regimes would require a non-linear viscoelastic or viscoplastic constitutive model. Second, the contact formulation neglects friction and adhesion. This is a reasonable approximation for the normal-impact and normal-indentation configurations studied, where tangential effects are minor, but it would need to be relaxed for oblique impacts, sliding contact, or materials with significant surface adhesion (e.g. soft elastomers at low contact pressure), where tangential and adhesive contributions can materially change the contact radius and force history. Third, temperature-dependent behaviour is incorporated only through time–temperature superposition (shift factors) calibrated from quasi-static DMA tests; the framework does not explicitly model self-heating or strain-rate-dependent thermal softening that may occur during rapid, repeated impacts. Fourth, the experimental validation, while covering several materials (NBR, PTFE, PEEK, Nylon, acrylic) and a range of frequencies, drop heights and temperatures, remains based on a limited number of replicates per condition; broader claims of predictive accuracy would benefit from a larger testing campaign with explicit repeatability statistics, sensor-calibration uncertainty, and quantitative error metrics (e.g. normalised RMSE) for the experimental–numerical comparisons, rather than the qualitative agreement reported here. These limitations do not undermine the validity of the results within the tested conditions, but they define the boundaries within which the proposed methodology should currently be applied, and they motivate the directions for future work.

Beyond the limitations discussed above, the results also carry direct implications for tribological applications that warrant further discussion. The dissipated energy quantified through indentation and impact tests is closely related to viscoelastic friction and rolling resistance, since both arise from the same hysteretic mechanism: the lag between stress and strain during cyclic deformation of the contact interface. The framework developed here — relating contact area, indentation depth and dissipated energy to the complex modulus — could therefore be extended to estimate friction coefficients and rolling resistance in sliding or rolling contacts, complementing existing models that typically require separate, dedicated friction measurements.

Similarly, the impact results have direct relevance to contact damping and wear. The viscoelastic dissipation that governs rebound height and contact duration in the impact tests is the same mechanism that controls damping efficiency in vibration-isolation components, while the repeated, transient contact-area evolution observed here is a first step toward characterising surface fatigue and wear under cyclic or impulsive loading — an aspect not addressed in the present work but consistent with the broader engineering relevance noted above, e.g. for tire–road interaction and protective systems.

The results of this study open up new perspectives for both engineering and scientific applications by providing practical and reliable tools for the analysis of viscoelastic behavior under real contact conditions. From an engineering perspective, these methodologies provide significant advantages in the design and optimization of damping elements, vibration isolation devices, and shock absorption technologies, as well as in rapid assessment of material performance in applications such as tire-road interaction, and protective systems where effective absorption of impact energy is essential.

From a scientific perspective, this work provides a solid foundation for the study of viscoelastic materials — polymers, soft composites, and biomaterials, especially biological tissues, thin coatings, and in-situ components. This is because local and non-invasive measurements are required in these cases. This approach is particularly important in cases where traditional methods such as Dynamic Mechanical Analysis cannot be applied due to sample or test limitations.

This thesis bridges the gap between materials characterization and real contact behavior by combining contact-based experiments with numerical and analytical models, and enables a more accurate, efficient, and application-oriented analysis of viscoelastic systems, allowing for the direct extraction of material properties from indentation and impact tests.

Appendix A

Preliminary Theoretical Model for Acrylic Ball Drop Experiments

A1 Theoretical Framework for Collision Dynamics and Impact Trajectory Analysis

Before implementing the Boundary Element Method (BEM), a preliminary theoretical model was developed to investigate whether the experimentally observed displacement response of the acrylic ball drop tests from the laser sensor could be reproduced using a simplified viscoelastic contact formulation. The model was intended as an initial validation framework prior to the implementation of the more computationally intensive BEM analysis. The formulation was based on Hertzian contact mechanics [43, 41] combined with a viscoelastic collision theory presented by Brilliantov et al. [155] , adapted for the impact of an acrylic sphere on a rigid sapphire substrate, and the results were compared.

The contact between an acrylic sphere and a sapphire disc is characterized by the normal compression $\zeta(\tau)$ that occurs during the impact. In general, the compression, $\zeta(\tau) = a_1 + a_2 - |\mathbf{x}_1(\tau) - \mathbf{x}_2(\tau)|$ is determined by the radii of curvature and position vectors of the contacting bodies. Since the sapphire disk is assumed to be much stiffer than the acrylic sphere ($a_2 \to \infty$), the effective radius and mass are equal to the sphere's radius $a^{\text{eff}} = a$ and mass $m^{\text{eff}} = m$, respectively. Therefore, the compression can be expressed in terms of the vertical position of the sphere's center:

$$\zeta(t) = a - y_c(t) \tag{A.1}$$

where the contact between the two bodies exists only when $y_c < a$. The elastic contact response between the acrylic sphere and the sapphire crystal was determined using Hertzian contact mechanics

$$\mathcal{P}_{\text{el}} = \chi\, \zeta^{3/2} \tag{A.2}$$

where the Hertzian stiffness coefficient is given by $\chi = 2\mathcal{E}\sqrt{a_{\text{eq}}}\,/\,[3\,(1-\vartheta^2)]$, and $\mathcal{E}$ and ϑ represent the Young's modulus and Poisson's ratio of the acrylic material, respectively. Equation (A.2) describes the nonlinear elastic resistance during deformation and assumes frictionless elastic contact conditions with small deformations.

To calculate the energy loss during impact, it is essential to introduce a dissipative force component within the viscoelastic material. The dissipative force is expressed as $\mathcal{P}_{\text{dis}} = \frac{\mathcal{E}}{(1-\vartheta^2)}\sqrt{a_{\text{eq}}}\,\Omega\sqrt{\zeta}\,\dot{\zeta}$, where Ω is a material-dependent dissipative parameter $\Omega = (1/3)\,[(3\psi_2-\psi_1)^2/(3\psi_2+2\psi_1)]\;[(1-\vartheta^2)(1-2\vartheta)/(\mathcal{E}\vartheta^2)]$ which is related to the viscous material constants, ψ_1 and ψ_2. Since these intrinsic viscous constants are generally not available for acrylic materials, the damping contribution was assumed to be a manually selected parameter at this initial stage. Therefore, the viscous damping coefficient $c_v = 3/2(\Omega\chi)$, which allows the dissipative force to be written in a compact form, was applied in this study.

$$\mathcal{P}_{\text{dis}} = c_v\sqrt{\zeta}\,\dot{\zeta} \tag{A.3}$$

where c_v is the effective damping coefficient and $\dot{\zeta}$ is the compression velocity. The total normal contact force acting during impact consequently becomes

$$\mathcal{P}^N = \chi\zeta^{3/2} + c_v\sqrt{\zeta}\,\dot{\zeta}. \tag{A.4}$$

For the isolated collision problem, the compression dynamics satisfy $m\ddot{\zeta} = -\mathcal{P}^N$. Substituting the elastic and dissipative contributions yields the governing viscoelastic collision equation

$$\ddot{\zeta} + \frac{2\mathcal{E}\sqrt{a_{\text{eff}}}}{3m(1-\vartheta^2)}\left(\zeta^{3/2} + (3/2)\Omega\sqrt{\zeta}\dot{\zeta}\right) = 0. \tag{A.5}$$

Using the kinematic relations $\zeta = a - y_c$, $\dot{\zeta} = -\dot{y}_c$, and $\ddot{\zeta} = -\ddot{y}_c$, the governing equation of motion for the acrylic sphere during contact was obtained as

$$-\ddot{y}_c = -\frac{1}{m}\left[\chi\,(a-y_c)^{3/2} + c_v\sqrt{a-y_c}\,(-\dot{y}_c)\right] \tag{A.6}$$

To simulate the complete ball-drop trajectory, the contact formulation was coupled with gravitational acceleration.

$$\ddot{y}_c = -g + \frac{1}{m}\left[\chi(a-y_c)^{3/2} - c_v\sqrt{a-y_c}\,\dot{y}_c\right]. \tag{A.7}$$

Equation (A.7) governs the motion during the contact phase ($y_c < a$), whereas during free fall ($y_c \geq a$) the motion reduces to $\ddot{y}_c = -g$. The nonlinear term $(a-y_c)^{3/2}$ represents the Hertzian elastic contribution, while the velocity-dependent damping term accounts for dissipation of energy during impact and rebound. To improve the representation of impact behaviour at higher drop energies, a simplified plasticity correction was also introduced. The total overlap was defined as $\delta_{\text{raw}} = \max(0, a - y_c)$ and decomposed into elastic and permanent components according to $\delta_{\text{el}} = \max(0, \delta_{\text{raw}} - \delta_{\text{perm}})$. Permanent deformation was updated using $\delta_{\text{perm}}^{\text{new}} = \max(\delta_{\text{perm}}, \delta_{\text{raw}} - \delta_{\text{yield}})$, where δ_{yield} represents the prescribed yield threshold.

Additionally, a loading–unloading stiffness correction was applied using an unloading multiplier f_{unload}, giving an effective unloading stiffness of $k_{\text{use}} = k f_{\text{unload}}$. These corrections enabled the model to capture hysteretic energy loss and permanent deformation during rebound without requiring a fully nonlinear plasticity formulation.

$$k_{\text{use}} = \begin{cases} k, & \text{if loading } (\dot{y}_c < 0), \\ k\, f_{\text{unload}}, & \text{if unloading } (\dot{y}_c \geq 0). \end{cases} \tag{A.8}$$

where $f_{\text{unload}} > 1$ is the unloading stiffness multiplier.

It should be noted that the parameters used in the theoretical calculations were not directly obtained from the independent material characteristics of the tested acrylic sample. They were selected from various literature sources according to the conditions under which the test was performed. These parameters were density $\rho = 1180$ kg/m^3, Young's modulus $\mathcal{E} = 3.2$ GPa, and Poisson's ratio $\vartheta = 0.35$. The plasticity correction took into account a yield stress of 2.0×10^{-5} m and a yield stress range of 0.02-0.04. The viscous damping coefficient was selected in the range of 13,700-16,800 $\text{N} \cdot \text{s/m}^{1.5}$, and the total impact mass was matched to the acrylic ball and holder assembly. Consequently, the original viscoelastic model cannot be presented as a fully predictive constitutive framework. It should rather be considered as a semi-empirical approximation designed to reproduce the dominant effect behavior. This represents an important limitation of the original model and was one of the main motivations for the application of the Boundary Element Method in the main part of the thesis, Chapter 3.

A2 Comparison with experimental results

In the preliminary theoretical model, an acrylic ball was dropped onto a sapphire disc from four different drop heights of 1.5 mm, 5 mm, 7 mm, and 10 mm, determined by a micrometer. The results were recorded using a laser sensor. The experimental results obtained are compared with theoretical calculations and are shown in detail in Figure A.1. Based on the comparison, we can say that the simplified viscous formulation is able to reproduce the general impact behavior and recoil characteristics observed experimentally.

Although deviations are visible at higher impact energies due to the simplified description of damping, local contact deformation and irreversible material effects, reasonable agreement between the experimental and theoretical curves was achieved at each of the four drop heights. Given that several damping and contact parameters were selected from literature values and were also manually adjusted damping coefficient, we cannot say that the model plays a predictive role. To overcome these limitations, select realistic parameters and provide more realistic predictions for more conditions, the BEM methodology is developed in Chapter 3. Nevertheless, the initial formulation provided additional validation of the newly constructed device, defined a useful initial confirmation of the experimental observations and provided confidence in the overall modeling strategy before applying the more rigorous Boundary Element Method framework presented in the main chapters of the thesis.

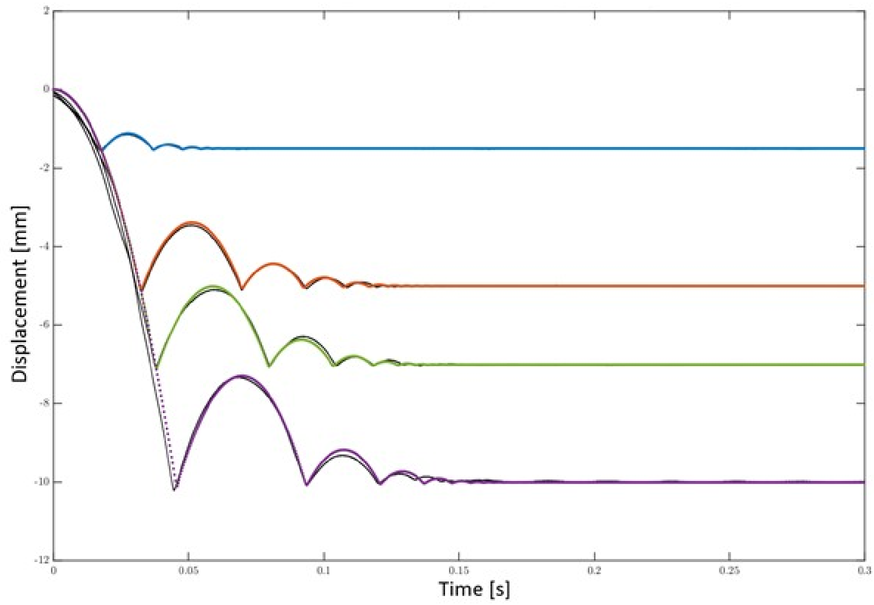

(a)

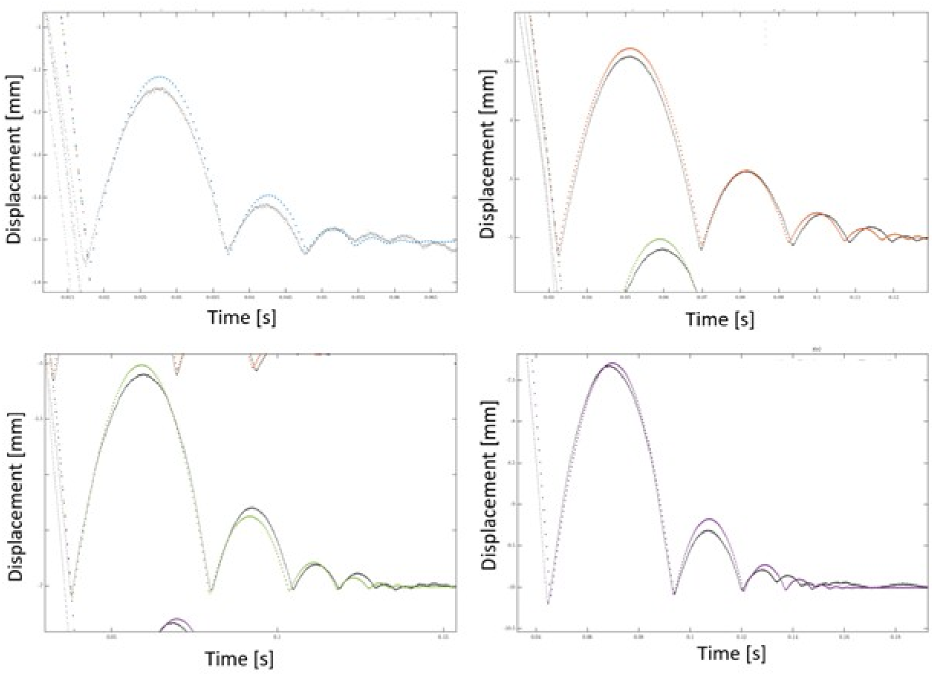

(b)

Figure A.1: Comparison between theoretical predictions and laser-based experimental measurements for acrylic ball drop impacts at four release heights: 1.5 mm (blue), 5 mm (red), 7 mm (green), and 10 mm (purple). In panel (a), colored dotted curves represent the theoretical results, while black curves correspond to the experimental laser measurements. Panel (b) presents magnified views of the first impact region for each drop height, highlighting the agreement between the theoretical model and experimental observations during the initial collision dynamics.

Appendix B

Plate Vibration During Impact Tests

B1 Experimental Setup and Measurement

Beyond the sphere displacement measurements described in Chapter 3, further experiments were performed to monitor the vibration of the support plate during impact. Nylon, Acrylic, PEEK, and PTFE spheres were dropped from heights of 1.5 mm, 5 mm, 7 mm, and 10 mm onto a sapphire disc embedded in a metal plate.

While the primary laser sensor was used to measure the sphere motion, in a second configuration the laser beam was directed to the surface of the plate close to the sapphire disc. This approach allowed recording the local vibrations generated by the impact (see Figure B.1a. When the sphere collides with the disc, some of its kinetic energy transfers to the support structure. Although the plate is rigid, measurements show small but measurable dynamic displacements during and after impact.

Figure B.1b provides a qualitative description of the response of the plate after impact. The plate oscillates around its equilibrium position with a small-amplitude motion characterized by alternating upward and downward displacements. The dashed lines indicate the boundaries of this oscillation, while the sinusoidal shape depicts the propagation of the vibration along the plate surface away from the impact region.

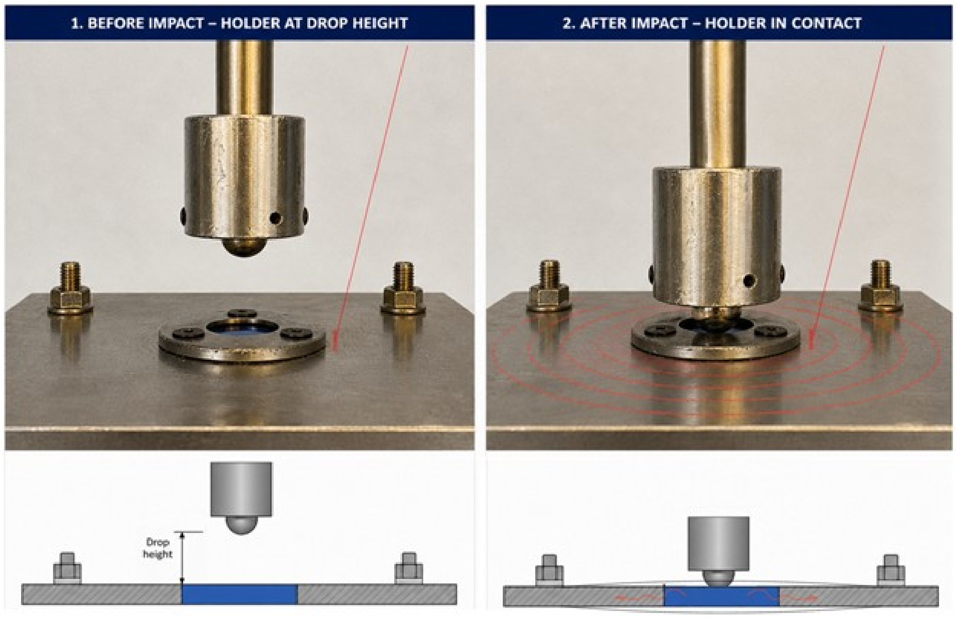

(a) Experimental setup

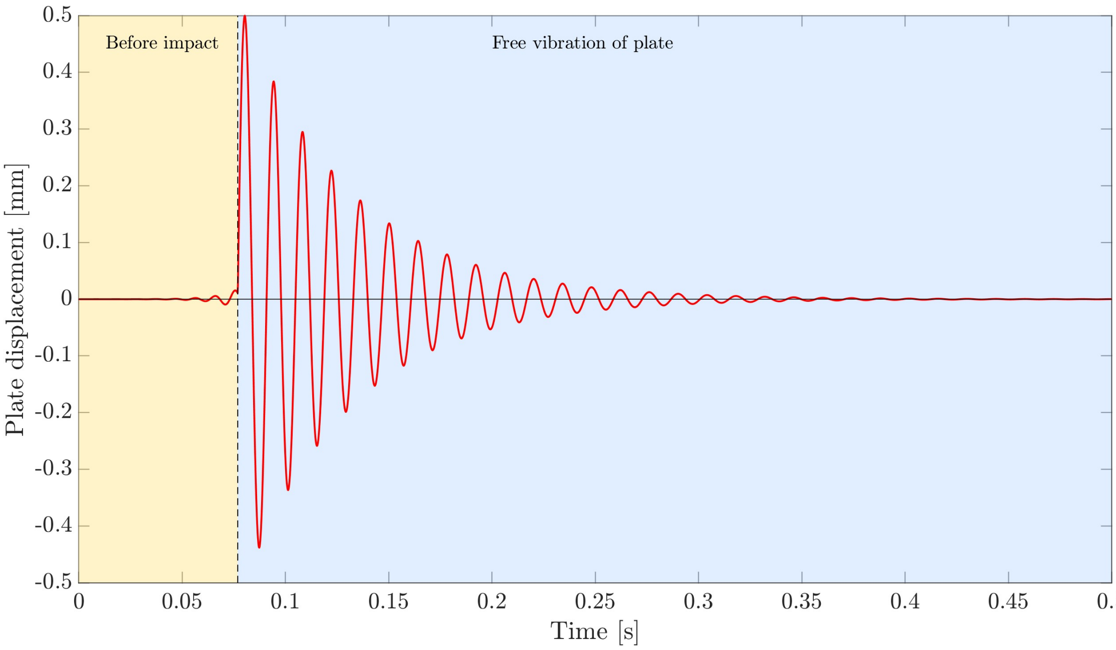

(b) Qualitative vibration representation

Figure B.1: (a) Impact configuration showing the holder on a sapphire disk placed on a metal plate, the attached sphere, and the laser beam before and after impact (top), and the corresponding schematic of the drop device showing the vibrational state before and after impact (bottom). (b) Qualitative representation of the plate response after impact, showing the equilibrium position and oscillation due to wave propagation.

B2 Measured Vibration Response

The measured plate response shows transient oscillations characteristic of damped systems. Figure B.2 shows sample signals for different materials: maximum displacement peaks occur immediately after impact, and then the amplitude gradually decreases due to damping. The symmetric nature of the signal around zero indicates that the plate is moving alternately up and down.

When comparing the materials, the overall oscillation shape is similar, the differences are mainly in the amplitude. The frequencies for nylon (red), acrylic (blue), PEEK (green) and PTFE (black) are almost identical, indicating that the vibration is mainly determined by the structural properties of the plate. The amplitude, however, varies depending on the impacting material and reflects the differences in the energy transferred.

As the drop height increases, the vibration amplitude increases correspondingly, which is associated with higher impact energy. However, the frequency composition remains constant. This result shows that the response of the plate is mainly controlled by its own dynamic properties, while the material of the sphere and the impact conditions mainly affect the magnitude of the vibration.

B3 Influence on Experimental–Numerical Discrepancies

In Chapter 3, we observed small differences between the experimental and numerical results. These differences are caused by several factors, the most important of which is the vibration of the plate. In the numerical model, the sapphire disk is assumed to be completely rigid and fixed, but experiments show that some of the impact energy is transferred to the plate, which in turn is dissipated in the form of vibrations.

This energy loss reduces the energy available for deformation and rebound of the sphere, and as a result, differences in the measured displacements occur. We can observe these both in the impact responses of the spheres and in the effects on the contact area. The effect is particularly strong at high drop heights, since in these cases the vibration amplitude increases. This effect is more pronounced in the case of acrylic spheres, since the movement of the plate changes the effective stiffness of the contact during impact.

As a result, the system behaves not as an ideal rigid contact, but as a more realistic mechanical system in which the impact and the structure interact. Taking into account the vibration of the plate allows us to better explain the experimental results and to understand the differences between the model and the measurements.

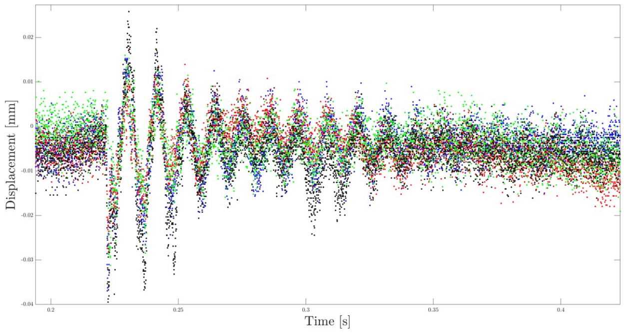

(a) 1.5 mm

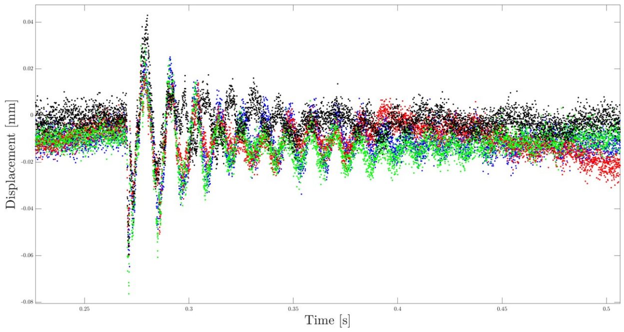

(b) 5 mm

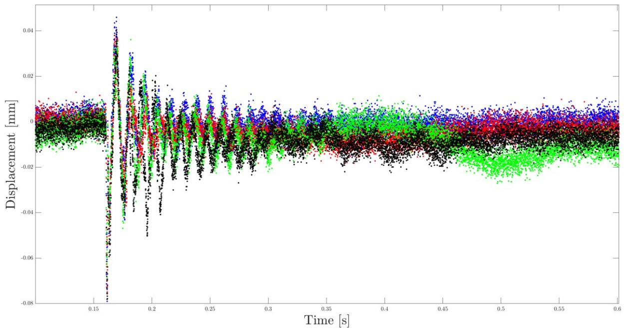

(c) 7 mm

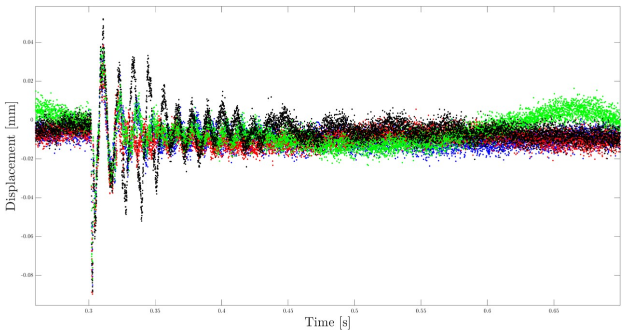

(d) 10 mm

Figure B.2: Measured plate vibration responses for drop heights of (a) 1.5 mm, (b) 5 mm, (c) 7 mm, and (d) 10 mm. The plate displacement near the sapphire disc is shown for impacts from Nylon (red), Acrylic (blue), PEEK (green), and PTFE (black) spheres.

Appendix C

Experimental Comparison of Displacement and Contact Radius

C1 Overview of Experimental Results

This appendix provides additional experimental results for the impact of an acrylic sphere on a sapphire substrate from various initial drop heights $h_0 = 1.5\,\mathrm{mm}$, $5\,\mathrm{mm}$, $7\,\mathrm{mm}$, $10\,\mathrm{mm}$. These data are complementary to the results obtained for other heights not mentioned in the main text and are only intended for experimental observation.

For each case, the vertical displacement of the sphere over time and the corresponding contact radius are presented. Displacement is measured using a high-precision Keyence laser displacement sensor, providing detailed information about the global motion of the sphere during impact.

The contact radius was independently measured using high-speed imaging, allowing direct observation of the contact area and its changes over time. Although the laser and imaging tests were performed at different times, we can observe a very good correlation between them. We can see that the radius changes according to the impact response. This shows that the results show consistent temporal correspondence between the two data sets, confirming that the observed trends are reproducible and reliable.

The comparison of these two measurements allows a direct assessment of the relationship between the macroscopic motion of the sphere and the microscopic development of the contact interface. In particular, the time evolution of the contact radius clearly follows the main features of the displacement signal — the initial impact, the maximum compression phase, and the subsequent rebound behavior.

As the drop height increases, both the magnitude of the displacement and the magnitude of the contact radius increase, reflecting higher impact energy. Despite the different impact conditions, the overall correspondence between the displacement and the development of the contact is maintained in all cases.

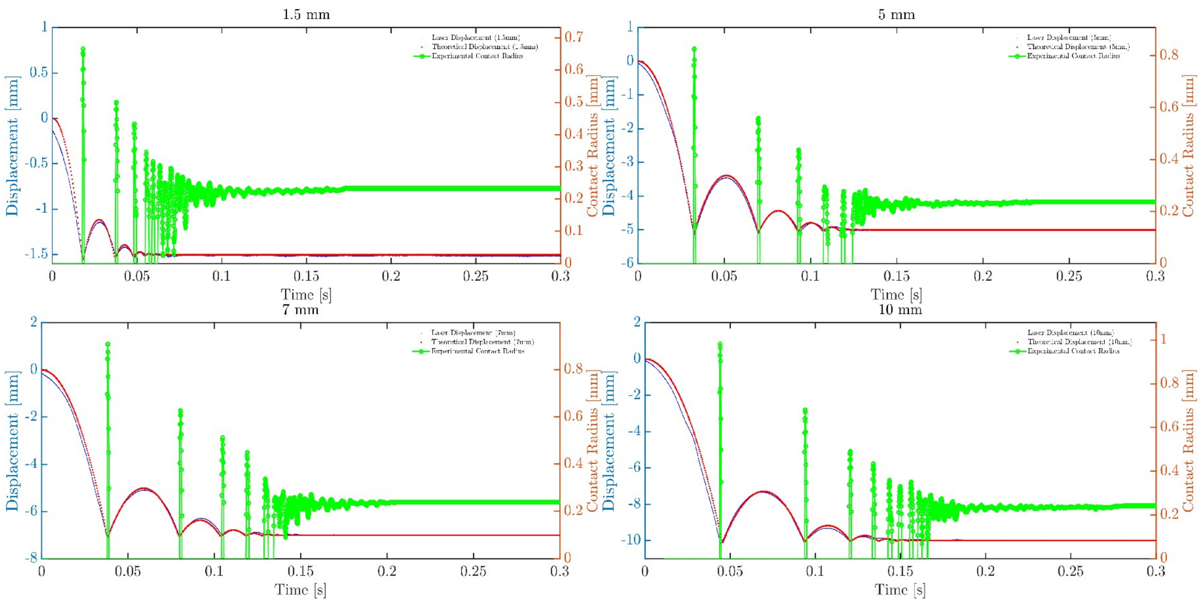

Figure C.1: General illustrations of the experimental evolution of vertical displacement and contact radius for an acrylic sphere impacting a sapphire substrate at different drop heights ($h_0 = 1.5\,\text{mm}, 5\,\text{mm}, 7\,\text{mm}, 10\,\text{mm}$). The blue curves show the laser-measured displacement, while the green marks show the contact radius obtained based on image processing from high-speed images, respectively, highlighting the relationship between global motion and contact evolution.

Appendix D

Camera and Image Calibration Procedures Used in the DIC Validation Tests

This annex describes the calibration procedures applied to the high-speed camera images used in the Digital Image Correlation (DIC) validation tests of Chapter 3. Two distinct optical configurations were used during the experimental campaign, and each required an independent pixel-to-millimetre calibration: (i) a front-view camera tracking the impact of a PTFE ball dropped onto a sapphire disc (Section D1), and (ii) a camera positioned beneath the sapphire disc to observe the contact area directly through the disc (Section D2). Because the two configurations use different lenses, working distances, and zoom settings, the magnification — and therefore the physical size represented by one pixel — is not the same for both cameras. Each camera was therefore calibrated separately using a reference object of known length placed in the same focal plane as the feature being measured.

D1 DIC Calibration — PTFE Ball Drop Test

The DIC validation test consisted of a PTFE (polytetrafluoroethylene) ball dropped from a height of 7 mm onto a sapphire disc. A single high-speed camera was positioned in front of the test rig, recording the lateral (side) view of the impact event. The camera was operated at a frame rate of 10,000 fps and a resolution of 1280 × 480 px, which provided sufficient temporal resolution to resolve the short duration of the impact and sufficient spatial resolution for subset-based correlation. The first frame of each recorded sequence, captured before the ball made contact with the disc, was used as the undeformed reference image required by the DIC algorithm.

The recorded image sequence was processed using DICe (Digital Image Correlation engine), an open-source DIC software. The analysis proceeded as follows:

- A reference line (shown in blue in Fig. D.1) was defined on the reference frame, positioned across the region of interest where displacement was to be tracked.
- A grid of subsets (yellow markers in Fig. D.1) was generated along and around this line. Each subset is a small image window whose grey-level pattern is tracked from frame to frame by cross-correlation.
- The full sequence of 9,367 frames was processed, and DICe computed the in-plane displacement of every subset relative to its position in the reference frame.
- The displacement of the reference line as a function of time was the primary output used to characterise the motion of the ball/fixture interface during impact.

Since the frame rate was fixed at 10,000 fps, the time interval between consecutive frames is 0.1 ms, allowing the frame index to be converted directly into elapsed time for the displacement–time curves presented in Chapter 3.

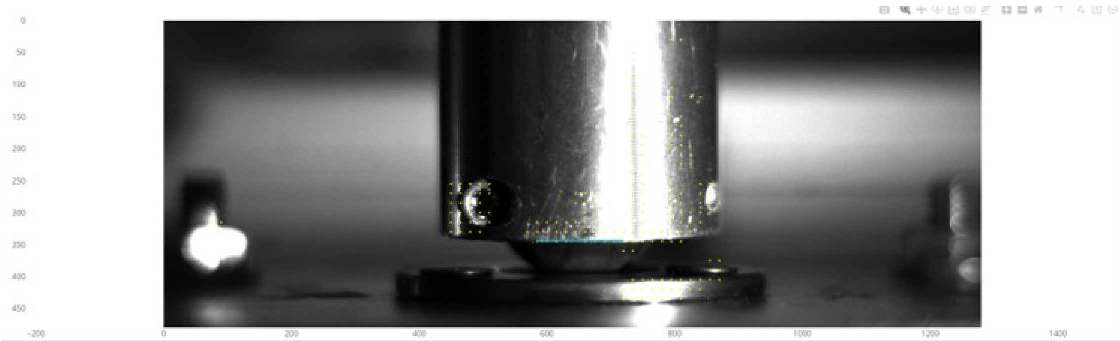

Figure D.1: DICe reference frame: subset grid (yellow) and reference line (blue) used to track displacement.

DICe reports displacement in pixel units, so a spatial calibration was needed to convert the output into physical units. For each test, the reference image was opened in Microsoft Paint, and a feature of known physical length within the field of view was measured in pixels using the on-screen measurement tool. The pixel size — i.e. the physical length represented by one pixel — was then obtained from:

$$\text{Pixel size} = \frac{\text{Real length}}{\text{Pixel length}} \tag{D.1}$$

For the present test, a reference length of 30 mm corresponded to a measured distance of 386 pixels, giving:

$$\text{Pixel size} = \frac{30\text{ mm}}{386\text{ px}} \approx 0.07772\text{ mm/px} \approx 77.7\ \mu\text{m/px} \tag{D.2}$$

This conversion factor was applied uniformly to the DICe pixel displacement output for this camera configuration, producing the millimetre-based displacement–time curves discussed in Chapter 3. Because the reference length spans a relatively large number of pixels (386 px), the relative uncertainty introduced by manual pixel-counting in Paint (typically ±1–2 px) is small, on the order of 0.3–0.5% of the calibrated length.

D2 Contact-Area Calibration: Camera Beneath the Sapphire Disc

For the contact-area measurements, the high-speed camera was relocated beneath the sapphire disc, viewing the contact region directly through the disc itself, in transmission rather than in the front-view (reflection/side) configuration used in Section D1. This change in viewpoint required a different lens, working distance, and zoom setting, all of which alter the optical magnification of the system. Consequently, the pixel-to-millimetre scale factor obtained for the front-view DIC camera (Section D1) cannot be applied to images from the under-disc camera, and an independent spatial calibration was performed for this configuration.

A calibration ruler with fine, evenly spaced graduations was placed directly on the sapphire disc, in the same focal plane as the contact region to be analysed, and imaged with the high-speed camera under the same acquisition settings used for the contact-area tests (10,000 fps, 1280 × 480 px resolution, see Fig. D.2). A known 1 mm interval on the ruler was selected and measured on screen, yielding a distance of 461 pixels. Using the same relation as in Section D1:

$$\text{Pixel size} = \frac{1\ \text{mm}}{461\ \text{px}} \approx 0.00217\ \text{mm/px} \approx 2.17\ \mu\text{m/px} \tag{D.3}$$

The resulting pixel size of approximately 2.17 μm/px reflects the much higher optical magnification used for the under-disc camera, as required to resolve the small dimensions of the contact area between the PTFE ball and the sapphire disc. This factor was used to convert all pixel-based contact-area measurements (e.g. contact width, contact diameter, contact-area evolution over time) obtained from the under-disc camera into physical units in the analysis presented in Chapter 3. Given the high magnification, an uncertainty of ±1 pixel in the ruler measurement (461 px) corresponds to a relative uncertainty of approximately 0.2%, which is considered acceptable for the contact-area measurements reported.

Table D.1 summarises the acquisition and calibration parameters used for the two camera configurations described in this annex.

The two calibrations were treated independently throughout the data-processing chain: pixel displacements from the front-view DIC analysis (Section D1) were converted using the 0.07772 mm/px factor, while pixel-based contact-area measurements from the under-disc camera (Section D2) were converted using the 0.00217 mm/px

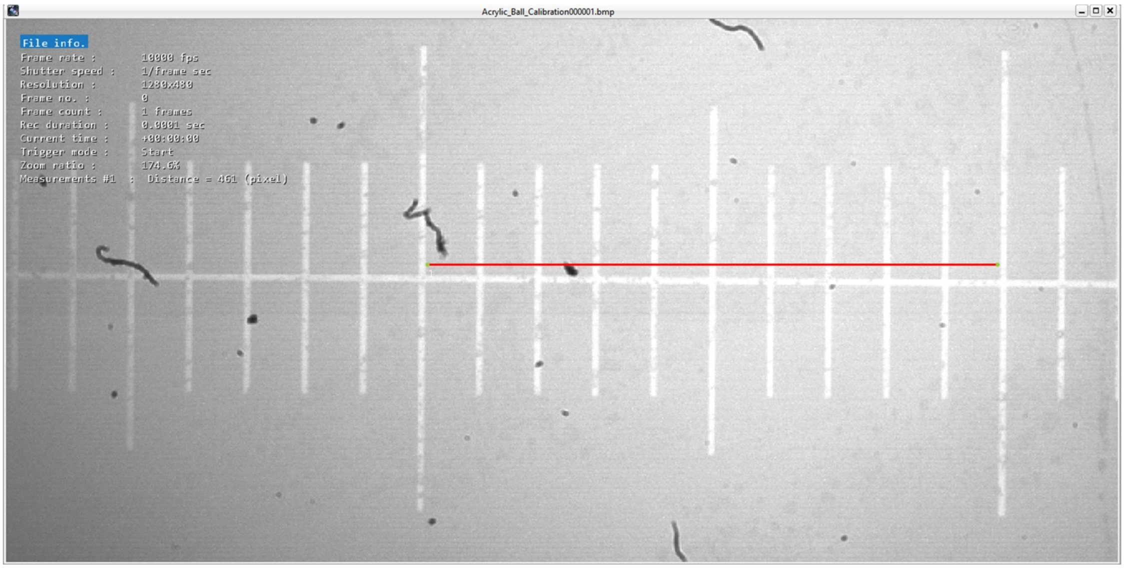

Figure D.2: Calibration ruler on the sapphire disc, imaged with the camera positioned beneath the disc. The 461-pixel distance corresponds to a 1 mm reference interval.

Table D.1: Calibration parameters for the front-view (DIC) and under-disc (contact-area) camera configurations.

Parameter	**D.1 – (DIC)**	**D.2 – (Contact Area)**
Frame rate	10,000 fps	10,000 fps
Resolution	1280 × 480 px	1280 × 480 px
Reference length used	30 mm	1 mm
Measured pixel distance	386 px	461 px
Pixel size	0.07772 mm (77.7 μm)	0.00217 mm (2.17 μm)
Approximate relative uncertainty	0.3–0.5%	0.2%

factor. This distinction is important, as applying the wrong calibration factor between the two camera configurations would lead to an error of approximately two orders of magnitude in the converted physical dimensions.

Bibliography

[1] Mohammad Mahdi Javidan and Jinkoo Kim. Experimental and numerical sensitivity assessment of viscoelasticity for polymer composite materials. *Scientific reports*, 10(1):675, 2020.

[2] Hareesh Tippur. Introduction to plastics engineering, 2021.

[3] Gizem Urtekin, Muhammad Saeed Ullah, Rumeysa Yildirim, Guralp Ozkoc, and Mehmet Kodal. A comprehensive review of the recent developments in thermoplastics and rubber blends-based composites and nanocomposites. *Polymer Composites*, 44(12):8303–8329, 2023.

[4] Olagoke Olabisi and Kolapo Adewale. *Handbook of thermoplastics*. CRC press, 2016.

[5] David T Wu, Nicholas Jeffreys, Mani Diba, and David J Mooney. Viscoelastic biomaterials for tissue regeneration. *Tissue Engineering Part C: Methods*, 28(7):289–300, 2022.

[6] Gang Bao and Subra Suresh. Cell and molecular mechanics of biological materials. *Nature materials*, 2(11):715–725, 2003.

[7] Albert James Licup, Stefan Münster, Abhinav Sharma, Michael Sheinman, Louise M Jawerth, Ben Fabry, David A Weitz, and Fred C MacKintosh. Stress controls the mechanics of collagen networks. *Proceedings of the National Academy of Sciences*, 112(31):9573–9578, 2015.

[8] Liqun Ning, Riya Mehta, Cong Cao, Andrea Theus, Martin Tomov, Ning Zhu, Eric R Weeks, Holly Bauser-Heaton, and Vahid Serpooshan. Embedded 3d bioprinting of gelatin methacryloyl-based constructs with highly tunable structural fidelity. *ACS applied materials & interfaces*, 12(40):44563–44577, 2020.

[9] Arulmozhivarman Joseph Chandran, Sanjay Mavinkere Rangappa, Indran Suyambulingam, and Suchart Siengchin. Micro/nano fillers for value-added polymer composites: A comprehensive review. *Journal of Vinyl and Additive Technology*, 30(5):1083–1123, 2024.

[10] Yakubu Kasimu Galadima, Selda Oterkus, Erkan Oterkus, Islam Amin, Abdel-Hameed El-Aassar, and Hosam Shawky. Modelling of viscoelastic materials using non-ordinary state-based peridynamics. *Engineering with Computers*, 40(1):527–540, 2024.

[11] Sahar Sultan, Gilberto Siqueira, Tanja Zimmermann, and Aji P Mathew. 3d printing of nano-cellulosic biomaterials for medical applications. *Current Opinion in Biomedical Engineering*, 2:29–34, 2017.

[12] Carmine Putignano, David Burris, Axel Moore, and Daniele Dini. Cartilage rehydration: The sliding-induced hydrodynamic triggering mechanism. *Acta Biomaterialia*, 125:90–99, 2021.

[13] Nariman Ashrafi and Mohamad Reza Eskafi. Application of viscoelastic fluids in industrial dampers. In *ASME International Mechanical Engineering Congress and Exposition*, volume 54921, pages 189–195, 2011.

[14] Gianmarco Vergassola, Dario Boote, and Angelo Tonelli. On the damping loss factor of viscoelastic materials for naval applications. *Ships and Offshore Structures*, 13(5):466–475, 2018.

[15] Francis Dave C Siacor, Qiyi Chen, Jia Yu Zhao, Lu Han, Arnaldo D Valino, Evelyn B Taboada, Eugene B Caldona, and Rigoberto C Advincula. On the additive manufacturing (3d printing) of viscoelastic materials and flow behavior: From composites to food manufacturing. *Additive Manufacturing*, 45:102043, 2021.

[16] Allan S Hoffman. Hydrogels for biomedical applications. *Advanced drug delivery reviews*, 64:18–23, 2012.

[17] Jos Malda, Jetze Visser, Ferry P Melchels, Tomasz Jüngst, Wim E Hennink, Wouter JA Dhert, Jürgen Groll, and Dietmar W Hutmacher. 25th anniversary article: engineering hydrogels for biofabrication. *Advanced materials*, 25(36):5011–5028, 2013.

[18] Adam S Verga, Sarah Jo Tucker, Yuming Gao, Alena M Plaskett, and Scott J Hollister. Nonlinear viscoelastic properties of 3d-printed tissue mimicking materials and metrics to determine the best printed material match to tissue mechanical behavior. *Frontiers in Mechanical Engineering*, 8:862375, 2022.

[19] Jusuf Ibrulj, Ejub Dzaferovic, Murco Obucina, and Manja Kitek Kuzman. Numerical and experimental investigations of polymer viscoelastic materials obtained by 3d printing. *Polymers*, 13(19):3276, 2021.

[20] David M Sengeh, Kevin M Moerman, Arthur Petron, and Hugh Herr. Multimaterial 3-d viscoelastic model of a transtibial residuum from in-vivo indentation and mri data. *Journal of the mechanical behavior of biomedical materials*, 59:379–392, 2016.

[21] Kuen Yong Lee and David J Mooney. Hydrogels for tissue engineering. *Chemical reviews*, 101(7):1869–1880, 2001.

[22] TJ Royston, HA Mansy, and RH Sandler. Excitation and propagation of surface waves on a viscoelastic half-space with application to medical diagnosis. *The Journal of the Acoustical Society of America*, 106(6):3678–3686, 1999.

[23] S. Yousef. 16 - polymer nanocomposite components: A case study on gears. In J. Njuguna, editor, *Lightweight Composite Structures in Transport*, pages 385–420. Woodhead Publishing, 2016.

[24] Zuzana Murčinková, Jozef Živčák, Jozef Zajac, and Pavel Adamčík. Passive multi-layer composite damper of flat belt tensioner idler. *Applied Sciences*, 11(7), 2021.

[25] Markus Heß and Fabian Forsbach. An analytical model for almost conformal spherical contact problems: Application to total hip arthroplasty with uhmwpe liner. *Applied Sciences*, 11(23), 2021.

[26] Ehsan Askari and Michael S Andersen. A closed-form formulation for the conformal articulation of metal-on-polyethylene hip prostheses: Contact mechanics and sliding distance. *Proceedings of the Institution of Mechanical Engineers, Part H: Journal of Engineering in Medicine*, 232(12):1196–1208, 2018. PMID: 30445886.

[27] J. Padovan, A. Kazempour, F. Tabaddor, and B. Brockman. Alternative formulations of rolling contact problems. *Finite Elements in Analysis and Design*, 11(4):275–284, 1992.

[28] Flavio Farroni, Michele Russo, Riccardo Russo, and Francesco Timpone. A physical-analytical model for a real-time local grip estimation of tyre rubber in sliding contact with road asperities. *Proceedings of the Institution of Mechanical Engineers, Part D: Journal of Automobile Engineering*, 228(8):955–969, 2014.

[29] Luigi Romano. Two-dimensional frbd friction models for rolling contact. *Nonlinear Dynamics*, 114(6):444, 2026.

[30] M. Fillon et al. Experimental study of tilting-pad journal bearings-comparison with theoretical thermoelastohydrodynamic results. *Journal of Tribology*, 1992.

[31] Michele Santeramo, Carmine Putignano, Georg Vorlaufer, Stefan Krenn, and Giuseppe Carbone. On the role of viscoelasticity in polymer rolling element bearings: load distribution and hysteretic losses. *Mechanism and Machine Theory*, 189:105421, 2023.

[32] Michele Santeramo, Guglielmo Giannetti, Enrico Meli, Giuseppe Carbone, and Carmine Putignano. Polymer journal bearings: A numerical and experimental study. *Tribology International*, 213:111010, 2026.

[33] Andrea Genovese and Sebastian Rosario Pastore. Development of a portable instrument for non-destructive characterization of the polymers viscoelastic properties. *Mechanical Systems and Signal Processing*, 150:107259, 2021.

[34] K. Friedrich. Polymer composites for tribological applications. *Advanced Industrial and Engineering Polymer Research*, 1(1):3–39, 2018.

[35] Richard M Christensen. *Theory of viscoelasticity*. Courier Corporation, 2013.

[36] Kyle D Allen and Kyriacos A Athanasiou. Viscoelastic characterization of the porcine temporomandibular joint disc under unconfined compression. *Journal of biomechanics*, 39(2):312–322, 2006.

[37] Carmine Putignano. Oscillating viscoelastic periodic contacts: A numerical approach. *International Journal of Mechanical Sciences*, 208:106663, 2021.

[38] Etibar Mikayilov, Michele Santeramo, Simone De Carolis, Giuseppe Carbone, and Carmine Putignano. Micro-oscillating indentation of viscoelastic solids: A combined numerical, analytical and experimental investigation. *International Journal of Solids and Structures*, page 113582, 2025.

[39] Carmine Putignano and Giuseppe Carbone. Indenting viscoelastic thin layers: A numerical assessment. *Mechanics Research Communications*, 126:104011, 2022.

[40] Carmine Putignano and Giuseppe Carbone. On the role of roughness in the indentation of viscoelastic solids. *Tribology Letters*, 70(4):117, 2022.

[41] Heinrich Hertz. The contact of elastic solids. *J Reine Angew, Math*, 92:156–171, 1881.

[42] EH Lee and Jens Rainer Maria Radok. The contact problem for viscoelastic bodies. 1960.

[43] SC Hunter. The hertz problem for a rigid spherical indenter and a viscoelastic half-space. *Journal of the Mechanics and Physics of Solids*, 8(4):219–234, 1960.

[44] Jacopo Bonari, Maria R Marulli, Nora Hagmeyer, Matthias Mayr, Alexander Popp, and Marco Paggi. A multi-scale fem-bem formulation for contact mechanics between rough surfaces. *Computational Mechanics*, 65:731–749, 2020.

[45] XW Zhang, Z Tao, and QM Zhang. Dynamic behaviors of visco-elastic thin-walled spherical shells impact onto a rigid plate, 2014.

[46] Fiachra Collins, Dermot Brabazon, and Kieran Moran. Viscoelastic impact characterisation of solid sports balls used in the irish sport of hurling. *Sports Engineering*, 14(1):15, 2011.

[47] Fiachra Collins, Dermot Brabazon, and Kieran Moran. The dynamic viscoelastic characterisation of the impact behaviour of the gaa sliotar. *Procedia Engineering*, 2(2):2991–2997, 2010.

[48] Mario Kunzemann, Astrid Pechstein, and Alexander Humer. Finite elements for large-strain viscoelasticity with volume-preserving internal strains: modeling and simulation of ball-drop tests: M. kunzemann et al. *Acta Mechanica*, pages 1–22, 2025.

[49] B Jian, GM Hu, ZQ Fang, HJ Zhou, and R Xia. A normal contact force approach for viscoelastic spheres of the same material. *Powder Technology*, 350:51–61, 2019.

[50] Flavio Farroni, Andrea Genovese, Antonio Maiorano, Aleksandr Sakhnevych, and Francesco Timpone. Development of an innovative instrument for non-destructive viscoelasticity characterization: Vesevo. In *The international conference of IFToMM ITALY*, pages 804–812. Springer, 2020.

[51] Thibaut André, Vincent Lévesque, Vincent Hayward, Philippe Lefèvre, and J-L Thonnard. Effect of skin hydration on the dynamics of fingertip gripping contact. *Journal of The Royal Society Interface*, 8(64):1574–1583, 2011.

[52] Michael L Crichton, Bogdan C Donose, Xianfeng Chen, Anthony P Raphael, Han Huang, and Mark AF Kendall. The viscoelastic, hyperelastic and scale dependent behaviour of freshly excised individual skin layers. *Biomaterials*, 32(20):4670–4681, 2011.

[53] Etibar Mikayilov. *The environmental impacts of the world energy transition: the role of raw materials mining.* PhD thesis, Politecnico di Torino, 2021.

[54] Guebum Han, Cole Hess, Melih Eriten, and Corinne R Henak. Uncoupled poroelastic and intrinsic viscoelastic dissipation in cartilage. *Journal of the Mechanical Behavior of Biomedical Materials*, 84:28–34, 2018.

[55] Yakup Artun, C Oktay Azeloglu, and Gökhan Taylan. Investigation of the tribological properties of pom and uhmwpe radial journal bearings made with different surface quality. *Proceedings of the Institution of Mechanical Engineers, Part J: Journal of Engineering Tribology*, 238(1):96–108, 2024.

[56] R Mnif, MC Ben Jemaa, N Hadj Kacem, and R Elleuch. Impact of viscoelasticity on the tribological behavior of ptfe composites for valve seals application. *Tribology transactions*, 56(5):879–886, 2013.

[57] You-Qiang Wang, Xiu-Jiang Shi, and Li-Jing Zhang. Experimental and numerical study on water-lubricated rubber bearings. *Industrial Lubrication and Tribology*, 66(2):282–288, 2014.

[58] Shijie Yu, Jun Cao, Shuxin Li, Haibo Huang, and Xiaojie Li. The tribological and mechanical properties of pi/pai/ep polymer coating under oil lubrication, seawater corrosion and dry sliding wear. *Polymers*, 15(6):1507, 2023.

[59] Jibrin Muhammad Yelwa, Haruna Musa, Opeoluwa O Fasanya, and Jibrin Yusuf Yahaya. Corrosion-resistant coatings: advances in deposition methods, nanostructures, and self-healing films. *Academia Materials Science*, 2(3), 2025.

[60] Shima Arian Kolour, Hanieh Sadat Mirjafari, Kimia Fathi, Hamid Khorsand, and Ali Ashtariyan. Polymeric coatings: a game changer for bearings in hybrid and electric automobiles. *Polymers for Advanced Technologies*, 36(5):e70170, 2025.

[61] Alireza S Sarvestani and Catalin R Picu. Network model for the viscoelastic behavior of polymer nanocomposites. *Polymer*, 45(22):7779–7790, 2004.

[62] Alba R Piacenti, Casey Adam, Nicholas Hawkins, Ryan Wagner, Jacob Seifert, Yukinori Taniguchi, Roger Proksch, and Sonia Contera. Nanoscale rheology: Dynamic mechanical analysis over a broad and continuous frequency range using photothermal actuation atomic force microscopy. *Macromolecules*, 57(3):1118–1127, 2024.

[63] Miroslav Slouf, Beata Strachota, Adam Strachota, Veronika Gajdosova, Vendulka Bertschova, and Jiri Nohava. Macro-, micro-and nanomechanical characterization of crosslinked polymers with very broad range of mechanical properties. *Polymers*, 12(12):2951, 2020.

[64] S Diridollou, F Patat, F Gens, L Vaillant, D Black, JM Lagarde, Y Gall, and

M Berson. In vivo model of the mechanical properties of the human skin under suction. *Skin Research and technology*, 6(4):214–221, 2000.

[65] M Lr WILLIAMS. Structural analysis of viscoelastic materials. *AIAA journal*, 2(5):785–808, 1964.

[66] Yuan-cheng Fung. *Biomechanics: mechanical properties of living tissues.* Springer Science & Business Media, 2013.

[67] Van C Mow, SC Kuei, W Michael Lai, and Cecil G Armstrong. Biphasic creep and stress relaxation of articular cartilage in compression: theory and experiments. 1980.

[68] Savio L-Y Woo, J Marcus Hollis, Douglas J Adams, Roger M Lyon, and Shinro Takai. Tensile properties of the human femur-anterior cruciate ligament-tibia complex: the effects of specimen age and orientation. *The American journal of sports medicine*, 19(3):217–225, 1991.

[69] Tsu T Soong and Gary F Dargush. Passive energy dissipation systems in structural engineering. *(No Title)*, 1997.

[70] Ahid D Nashif, David IG Jones, and John P Henderson. *Vibration damping.* John Wiley & Sons, 1991.

[71] James M Kelly. *Earthquake-resistant design with rubber*, volume 7. Springer, 1993.

[72] MD Symans. Passive fluid viscous damping systems for seismic energy dissipation. *ISET J Earthq Technol*, 35(4):185, 1998.

[73] Daniela Rus and Michael T Tolley. Design, fabrication and control of soft robots. *Nature*, 521(7553):467–475, 2015.

[74] Filip Ilievski, Aaron D Mazzeo, Robert F Shepherd, Xin Chen, and George Whitesides. Soft robotics for chemists. 2011.

[75] Robert K Flitney. *Seals and sealing handbook.* Elsevier, 2011.

[76] Roderic S Lakes. *Viscoelastic materials.* Cambridge university press, 2009.

[77] B. N. J. Persson. Theory of rubber friction and contact mechanics. *The Journal of Chemical Physics*, 115(8):3840–3861, aug 2001.

[78] Richard Christensen. *Theory of viscoelasticity: an introduction.* Elsevier, 2012.

[79] K. A. Grosch. The relation between the friction and visco-elastic properties of rubber. *Proceedings of the Royal Society of London. Series A. Mathematical and Physical Sciences*, 274(1356):21–39, jun 1963.

[80] Harvey Thomas Banks, Shuhua Hu, and Zackary R Kenz. A brief review of elasticity and viscoelasticity for solids. *Advances in Applied Mathematics and Mechanics*, 3(1):1–51, 2011.

[81] Michael Rubinstein and Ralph H Colby. *Polymer physics.* Oxford university press, 2003.

[82] John D Ferry and Henry S Myers. Viscoelastic properties of polymers. *Journal of The Electrochemical Society*, 108(7):142C–143C, 1961.

[83] Ronald G Larson. The structure and rheology of complex fluids. *(No Title)*, 1999.

[84] Jan Mewis and Norman J Wagner. *Colloidal suspension rheology*. Cambridge university press, 2012.

[85] David Roylance. Engineering viscoelasticity. *Department of Materials Science and Engineering–Massachusetts Institute of Technology, Cambridge MA*, 2139:1–37, 2001.

[86] Lawrence E Malvern. *Introduction to the Mechanics of a Continuous Medium*. Number Monograph. 1969.

[87] F Riesz and B Nagy. Functional analysis, dover books on mathematics. 2012.

[88] Clifford Truesdell and Walter Noll. The non-linear field theories of mechanics. In *The non-linear field theories of mechanics*, pages 1–579. Springer, 2004.

[89] Francesco Mainardi and Giorgio Spada. Creep, relaxation and viscosity properties for basic fractional models in rheology. *The European Physical Journal Special Topics*, 193(1):133–160, 2011.

[90] Allen C Pipkin. *Lectures on viscoelasticity theory*. Springer Science & Business Media, 2012.

[91] Vito Volterra and ET Whittaker. *Theory of functionals and of integral and integro-differential equations*. Dover New York, 1931.

[92] Bernard D Coleman and Victor J Mizel. A general theory of dissipation in materials with memory. *Archive for Rational Mechanics and Analysis*, 27(4):255–274, 1967.

[93] Bernard D Coleman, Bernard D Coleman, Bernard D Coleman, Etats-Unis Chimiste, and Bernard D Coleman. *Thermodynamics of materials with memory*. Springer, 1972.

[94] TCT Ting. The contact stresses between a rigid indenter and a viscoelastic half-space. 1966.

[95] C Truesdell. The non-linear field theories of mechanocs. *Encyclopedia of physics*, 3:5–8, 1965.

[96] Morton E Gurtin, Eliot Fried, and Lallit Anand. *The mechanics and thermodynamics of continua*. Cambridge university press, 2010.

[97] Gerard A Maugin. *The thermomechanics of plasticity and fracture*, volume 7. Cambridge university press, 1992.

[98] Morton E Gurtin and Ismael Herrera. On dissipation inequalities and linear viscoelasticity. *Quarterly of applied mathematics*, 23(3):235–245, 1965.

[99] J Heijboer. Secondary loss peaks in glassy amorphous polymers. *International Journal of Polymeric Materials*, 6(1-2):11–37, 1977.

[100] André J Kovacs. La contraction isotherme du volume des polymères amorphes. *Journal of polymer science*, 30(121):131–147, 1958.

[101] Leslie Howard Sperling. Sound and vibration damping with polymers: Basic viscoelastic definitions and concepts. ACS Publications, 1990.

[102] David Turnbull and Morrel H Cohen. Free-volume model of the amorphous phase: glass transition. *The Journal of chemical physics*, 34(1):120–125, 1961.

[103] Namdeo R Jadhav, Vinod L Gaikwad, Karthik J Nair, and Hanmantrao M Kadam. Glass transition temperature: Basics and application in pharmaceutical sector. *Asian Journal of Pharmaceutics (AJP)*, 3(2), 2009.

[104] Thomas G Fox Jr and Paul J Flory. Second-order transition temperatures and related properties of polystyrene. i. influence of molecular weight. *Journal of Applied Physics*, 21(6):581–591, 1950.

[105] Herbert Leaderman. *Elastic and creep properties of filamentous materials*. PhD thesis, MassaChusetts Institute of Technology, 1941.

[106] John D Ferry. Mechanical properties of substances of high molecular weight. vi. dispersion in concentrated polymer solutions and its dependence on temperature and concentration. *Journal of the American Chemical Society*, 72(8):3746–3752, 1950.

[107] F Schwarzl and AJ Staverman. Time-temperature dependence of linear viscoelastic behavior. *Journal of Applied Physics*, 23(8):838–843, 1952.

[108] Michele Santeramo. Numerical and experimental methods for viscoelastic circular contacts in dry and lubricated conditions. 2023.

[109] Salete Martins Alves, VS Mello, and Jarbas Santos Medeiros. Palm and soybean biodiesel compatibility with fuel system elastomers. *Tribology International*, 65:74–80, 2013.

[110] HH Bertram. Developments in acrylonitrile—butadiene rubber (nbr) and future prospects. In *Developments in Rubber Technology—2: Synthetic Rubbers*, pages 51–85. Springer, 1981.

[111] Syam Prasad Ammineni, D Lingaraju, and Ch Nagaraju. The effects of physical aging on the quasi-static and dynamic viscoelastic properties of nitrile butadiene rubber. *Mechanics of Time-Dependent Materials*, 27(3):765–789, 2023.

[112] Marine Lallemant, T Kadiake, J Chambert, A Lejeune, R Ramanah, N Mottet, M Cosson, and E Jacquet. Influence of experimental conditions on some in-vitro biomechanical properties of the sow's perineum. *Scientific Reports*, 14(1):27455, 2024.

[113] H Orava, P Paakkari, J Jäntti, MK Honkanen, JT Honkanen, T Virén, P Tanska, RK Korhonen, MW Grinstaff, J Töyräs, et al. Triple contrast computed tomography reveals site-specific differences in human knee joint biomechanical properties. *Osteoarthritis and Cartilage*, 31:S257–S258, 2023.

[114] Paige S Woods, Alyssa A Morin, Po-Jung Chen, Sarah Mahonski, Liping Xiao, Marja Hurley, Sumit Yadav, and Tannin A Schmidt. Automated indentation demonstrates structural stiffness of femoral articular cartilage and temporomandibular joint mandibular condylar cartilage is altered in fgf2ko mice. *Cartilage*, 13(2_suppl):1513S–1521S, 2021.

[115] Bernard Drouin, Lucie Lévesque, Audrey Lainé, Erica Rosella, Caroline Loy, and Diego Mantovani. Viscoelastic properties of collagen hydrogels.

[116] Michelle Griffin, Yaami Premakumar, Alexander Seifalian, Peter Edward Butler, and Matthew Szarko. Biomechanical characterization of human soft tissues using indentation and tensile testing. *Journal of visualized experiments: JoVE*, (118), 2016.

[117] Michael Ortiz. Linear viscoelasticity: Mechanics, analysis and approximation. *Archives of Computational Methods in Engineering*, pages 1–21, 2025.

[118] G. Carbone, B. Lorenz, B. N. J. Persson, and A. Wohlers. Contact mechanics and rubber friction for randomly rough surfaces with anisotropic statistical properties. *The European Physical Journal E*, 29(3):275–284, jul 2009.

[119] Giuseppe Carbone and Carmine Putignano. A novel methodology to predict sliding and rolling friction of viscoelastic materials: Theory and experiments. *Journal of the Mechanics and Physics of Solids*, 61(8):1822–1834, 2013.

[120] G. Carbone and L. Mangialardi. Adhesion and friction of an elastic half-space in contact with a slightly wavy rigid surface. *Journal of the Mechanics and Physics of Solids*, 52:1267–1287, 6 2004.

[121] Julius S Bendat and Allan G Piersol. *Random data: analysis and measurement procedures*. John Wiley & Sons, 2011.

[122] Alan V. Oppenheim and Roland W. Schafer. *Discrete-time signal processing*. Always learning. Pearson, Harlow, third edition, pearson new international edition edition, 2014.

[123] Malcolm L Williams, Robert F Landel, and John D Ferry. The temperature dependence of relaxation mechanisms in amorphous polymers and other glass-forming liquids. *Journal of the American Chemical society*, 77(14):3701–3707, 1955.

[124] Alan N Gent. A new constitutive relation for rubber. *Rubber chemistry and technology*, 69(1):59–61, 1996.

[125] Lucie Rouleau, Rogério Pirk, Bert Pluymers, and Wim Desmet. Characterization and modeling of the viscoelastic behavior of a self-adhesive rubber using dynamic mechanical analysis tests. *Journal of Aerospace Technology and Management*, 7:200–208, 2015.

[126] B N J Persson, O Albohr, U Tartaglino, A I Volokitin, and E Tosatti. On the nature of surface roughness with application to contact mechanics, sealing, rubber friction and adhesion. *Journal of Physics: Condensed Matter*, 17(1):R1, dec 2004.

[127] B. N. J. Persson. Rubber friction: role of the flash temperature. *Journal of Physics: Condensed Matter*, 18(32):7789–7823, jul Persson2006.

[128] T Pritz. Verification of local kramers–kronig relations for complex modulus by means of fractional derivative model. *Journal of Sound and Vibration*, 228(5):1145–1165, 1999.

[129] SW Park and RA0942 Schapery. Methods of interconversion between linear

viscoelastic material functions. part i—a numerical method based on prony series. *International journal of solids and structures*, 36(11):1653–1675, 1999.

[130] David Cheneler, Nazia Mehrban, and James Bowen. Spherical indentation analysis of stress relaxation for thin film viscoelastic materials. *Rheologica Acta*, 52(7):695–706, 2013.

[131] Yu M Efremov, SL Kotova, and PS Timashev. Viscoelasticity in simple indentation-cycle experiments: a computational study. *Scientific reports*, 10(1):13302, 2020.

[132] Mark R VanLandingham, N-K Chang, PL Drzal, Christopher C White, and S-H Chang. Viscoelastic characterization of polymers using instrumented indentation. i. quasi-static testing. *Journal of Polymer Science Part B: Polymer Physics*, 43(14):1794–1811, 2005.

[133] Christopher C White, Mark R VanLandingham, PL Drzal, N-K Chang, and S-H Chang. Viscoelastic characterization of polymers using instrumented indentation. ii. dynamic testing. *Journal of Polymer Science Part B: Polymer Physics*, 43(14):1812–1824, 2005.

[134] Che-Yu Lin, Yi-Cheng Chen, Chen-Hsin Lin, and Ke-Vin Chang. Constitutive equations for analyzing stress relaxation and creep of viscoelastic materials based on standard linear solid model derived with finite loading rate. *Polymers*, 14(10):2124, 2022.

[135] Nicholas W Tschoegl. *The phenomenological theory of linear viscoelastic behavior: an introduction.* Springer Science & Business Media, 2012.

[136] A. Persson. *On the Stress Distribution of cylindrical elastic bodies in contact.* Doktorsavhandlingar vid Chalmers tekniska Högskola. Fototryck, 1964.

[137] Jin Haeng Lee, Yanfei Gao, Allan F. Bower, Haitao Xu, and George M. Pharr. Stiffness of frictional contact of dissimilar elastic solids. *Journal of the Mechanics and Physics of Solids*, 112:318–333, 2018.

[138] K. L. Johnson. *Contact Mechanics.* Cambridge University Press, 1985.

[139] N. Menga, G. Carbone, and D. Dini. Exploring the effect of geometric coupling on friction and energy dissipation in rough contacts of elastic and viscoelastic coatings. *Journal of the Mechanics and Physics of Solids*, 148:104273, 2021.

[140] DW Schmid and Yu Y Podladchikov. Fold amplification rates and dominant wavelength selection in multilayer stacks. *Philosophical Magazine*, 86(21-22):3409–3423, 2006.

[141] Hongyan Ding, Guanghong Zhou, Tao Liu, Mujian Xia, and Xiangming Wang. Biotribological properties of ti/tib2 multilayers in simulated body solution. *Tribology International*, 89:62–66, 2015.

[142] Egor A Kapitonov, Natalia N Petrova, Vasilii V Mukhin, Leonid A Nikiforov, Vladimir D Gogolev, Ee Le Shim, Aitalina A Okhlopkova, and Jin-Ho Cho. Enhanced physical and mechanical properties of nitrile-butadiene rubber composites with n-cetylpyridinium bromide-carbon black. *Molecules*,

26(4):805, 2021.

[143] Rodney Loudon. Theory of the first-order raman effect in crystals. *Proceedings of the Royal Society of London. Series A. Mathematical and Physical Sciences*, 275(1361):218–232, 1963.

[144] Hongxiang Yin, Yi Wu, Dan Liu, Pengpai Zhang, Guanzhen Zhang, and Hanwei Fu. Rolling contact fatigue-related microstructural alterations in bearing steels: A brief review. *Metals*, 12(6):910, 2022.

[145] Guillermo E Morales-Espejel and V Brizmer. Micropitting modelling in rolling–sliding contacts: application to rolling bearings. *tribology transactions*, 54(4):625–643, 2011.

[146] Michela Faccoli, Candida Petrogalli, Matteo Lancini, Andrea Ghidini, and Angelo Mazzù. Rolling contact fatigue and wear behavior of high-performance railway wheel steels under various rolling-sliding contact conditions. *Journal of Materials Engineering and Performance*, 26(7):3271–3284, 2017.

[147] Mohan D Rao. Recent applications of viscoelastic damping for noise control in automobiles and commercial airplanes. *Journal of sound and vibration*, 262(3):457–474, 2003.

[148] Ian Hutchings and Philip Shipway. *Tribology: friction and wear of engineering materials*. Butterworth-heinemann, 2017.

[149] Ian Gibson, David Rosen, Brent Stucker, Mahyar Khorasani, David Rosen, Brent Stucker, and Mahyar Khorasani. *Additive manufacturing technologies*, volume 17. Springer, 2021.

[150] N Jones. Structural impact. cambridge university press; 2012.

[151] A Ovcharenko, G Halperin, I Etsion, and M Varenberg. A novel test rig for in situ and real time optical measurement of the contact area evolution during pre-sliding of a spherical contact. *Tribology Letters*, 23(1):55–63, 2006.

[152] Kenneth Langstreth Johnson and Kenneth Langstreth Johnson. *Contact mechanics*. Cambridge university press, 1987.

[153] Vlado A Lubarda. Circular loads on the surface of a half-space: displacement and stress discontinuities under the load. *International Journal of Solids and Structures*, 50(1):1–14, 2013.

[154] Simone De Carolis, Carmine Putignano, Leonardo Soria, and Giuseppe Carbone. Viscoelastic foundation-induced vibrations: Exploring linear theory application fields through numerical simulations. *Journal of Sound and Vibration*, page 119415, 2025.

[155] Nikolai V Brilliantov, Frank Spahn, Jan-Martin Hertzsch, and Thorsten Pöschel. Model for collisions in granular gases. *Physical review E*, 53(5):5382, 1996.

Publications

Mikayilov, E., Santeramo, M., De Carolis, S., Carbone, G., and Putignano, C. (2025). *Micro-oscillating indentation of viscoelastic solids: A combined numerical, analytical and experimental investigation.* International Journal of Solids and Structures, 113582. Elsevier (Pergamon).

Santeramo, M., **Mikayilov, E.**, Jaman, J., Dini, D., Fantetti, A., and Putignano, C. *Impacts of viscoelastic solids: A numerical and experimental analysis* (submitted).

Acknowledgments

I would like to express my sincere gratitude to my supervisors, Prof. Carmine Putignano and Prof. Giuseppe Carbone, for their continuous support throughout my Ph.D. research, as well as for their guidance, motivation, and encouragement.

I would like to extend my sincere thanks to the Tribology Group at Imperial College London, in particular Prof. Daniele Dini, Prof. Thomas Reddyhoff, and Dr. Alfredo Fantetti, for hosting me and for the stimulating discussions and inspiring scientific environment.

Finally, I would like to express my deepest gratitude to my family for their unconditional support, patience, and encouragement throughout this journey. Their constant presence and belief in me have been my greatest source of strength.